学位論文

A theoretical study on quantum state and optical trapping of excitons

(励起子の量子状態と光学トラップに関する理論研究)

平成２９年12月博士(理学)申請

東京大学大学院理学系研究科
物理学専攻
加藤　洋生

ABSTRACT

Excitons are bosonic composite particles formed by electron-hole pairs. In condensed matter physics, excitons are involved in the optical processes of semiconductors or insulators. There are mainly two ways for generating excitons in solids. One way is irradiating light to the solids. When the energy of a photon is larger than the band gap, an electron-hole pair is generated. Excited electron-hole pairs form exciton gas by the attractive Coulomb interaction. Of course direct excitation of excitons is possible. Another way is preparing a junction of N type and P type semiconductors and applying a gate voltage. Then these semiconductors release carriers and they form excitons. Generated excitons decay into a photon with finite lifetime. Thus the excitons have a great significance for understanding the optical response of solids and for designing optical devices.

The electron-hole many-body system has been vigorously studied and concepts of several fundamental phases are established. The exciton gas phase, the electron hole plasma, and the electron hole liquid. However, there are still some excitonic phases or few-body bound states whose formations are confirmed in limited number of materials. The exciton BEC is the most famous example. Since the BEC transition temperature is proportional to the inverse of particle mass, excitonic system has been regarded as a promising system for realizing BEC, thanks to the light mass of exciton. Another example is the polyexciton, an excitonic n-body bound state (PE_n). The presence of biexcitons, or excitonic molecules is trivial since such bound states are quite common in similar systems such as hydrogen atom and positronium. But the formation of PE_n for $n \geq 3$ is non-trivial since hydrogen and positronium do not make a trimer. It has been predicted that the formation of PE_n for $n \geq 3$ requires orbital degeneracy on band dispersion extrema. It is uncertain if polyexciton forms many-body phases.

We also mention about experimental techniques for trapping excitons. This method is aimed at realizing exciton BEC by capturing excitons on the bottom of trapping potential. The most popular method is applying a local strain on the crystal. Locally induced pressure reduces band gap and it works as an effective potential for carriers. In addition several confinement techniques have been proposed experimentally and theoretically. We focused on the optical trapping techniques used in the ultra-cold atomic system. It utilizes energy level shift of atoms induced by a laser irradiation which is nearly resonant to the energy level intervals of atoms. This mechanism is in principle applicable to the excitonic system in solids, but it has not been investigated so far.

Our thesis has two goals. The first one is numerically investigating the stability of polyexcitons. Although the condition of the polyexciton formation, namely the presence

of orbital degeneracy is quite common in many materials, only a limited number of theoretical and experimental studies have been reported. Recently an experimental study reported that five peaks were observed in low energy tail of a strong exciton recombination peak in photoluminescence spectrum of diamond. They attributed these peaks to an electron-hole recombination in polyexcitons. We aim to verify if those peaks are really explained by polyexcitons. The second one is a theoretical examination of the feasibility of optical trapping technique of excitons. We are using the same physical mechanism of optical trapping with that of ultra-cold atomic system. If such technique is feasible we can expect that it will be a strong tool to explore physical property of excitonic systems.

In this thesis we use two distinct theoretical schemes for the description of excitonic systems in solids. For numerical calculation of polyexcitons we describe the electron-hole system as an ensemble of independent particles with unit charge. The orbital degeneracy can be included in our model based on the $\boldsymbol{k} \cdot \boldsymbol{p}$ perturbation theory. The trial wave function is described by the explicitly correlated Gaussian (ECG) basis set. The ECG basis state is numerically low costing and has an ability to precisely describe the inter-particle correlation. The variational parameters are optimized by a randomly sampling method.

For the description of the light-matter interaction and the optical potential, we combine two methods. A model calculation which is in principle applicable to any quantum system with discrete inner excitation levels, and a first principles method to determine the parameters of the model. We use the GW+BSE method for simulating exciton energy spectrum and its wave function. This method is regarded as one of the most precise method for predicting the optical gap of solids.

For the first goal, we show that we succeeded in showing the stabilization of triexcitons and smaller complexes such as excitons, trions, biexcitons, and charged biexcitons in diamond. In the case of bulk crystal, triexcitons and charged biexcitons are truly unique in a system with orbital degeneracy. Calculated binding energies reproduce about 80% of the experimentally observed values. Our results support the interpretation that the experimentally observed peaks are originating from carrier recombination processes in polyexcitons. For the second goal, we show that an optical potential with $O(10^2)\mu$eV depth is feasible in graphane, a two-dimensional wide gap semiconductor. Furthermore we revealed that by appropriately choosing the direction of light polarization, it is feasible to selectively trap either of doubly degenerate excitonic states in graphane.

CONTENTS

ACKNOWLEDGEMENTS

To write this Ph.D. thesis I have been supported by many peoples and hence I want to show deep gratitude to them in order. Firstly, I am deeply grateful to my supervisor Prof. Shinji Tsuneyuki for his continuous and patient support for accomplishing our study. Through numerous insightful discussions with him, I could learn what a scientific research should be. Secondly, I express my great appreciation to Assistant Prof. Ryosuke Akashi for his guidance. From supporting solutions for individual obstacles in my research to proofreading of a paper, he enthusiastically supported my research activity. I firmly believe that it would be hard to complete my research without his help. Thirdly, I would also like to express my special gratitude to Prof. Kálmán Varga and Prof. Junko Usukura, the collaborators in the study of part I. They generously permitted me to use and develop the program of a few-body problem solver using SVM and ECG basis state. I was greatly helped by their apt and kind advices. Their contributions are crucial for this thesis.

It must be also emphasized that I have been helped not only in a place of study. From this aspect, I deeply appreciate Prof. Peter Maksym particularly for his guidance of writing not only papers but also job applications in english. Despite that he is not my official supervisor, he spared great amount of effort for coaching me. I cannot thank him enough for his kindness. A comfortably managed environment of laboratory was also essential for performing my researches for this five years. I owe it to two secretaries of our laboratory, Ms Makiko Fukuda and Ms Emi Shimosikiryo. They have been supported us with a lot of patience and I would like to show a debt of gratitude to them. I also thank to laboratory members those who shared precious time and did exciting discussions with me. I hope their successes in society.

Finally I mention a deep sense of gratitude and respect to my family, especially to my parents, Hideki Katow and Tomoko Katow. My father has been working so many years as a biologist and mother also has a background in same field. There is no doubt that my curiosity to nature science has been cultivated and protected in a home environment they prepared which is free from absurd peer pressures and/or suppressions. I also show a great gratitude to my fiancée, Mariko Okazawa for her patient emotional support in a couple of years after we met. She has been not only the mental mainstay but also a window to the outside of academia, and she sometimes let me know what I lack. I would like to thank about this point, too.

1. INTRODUCTION

1.1 An overview of the excitonic system in solids

Exctions are hydrogen-like composite particles formed by an electron-hole pair. The excitons can be formed when free carriers combine with each other by the Coulomb interaction. There are mainly two ways to generate free carriers in solids. One way is utilizing the photo-excitation processes in semiconductors. When the energy of a photon is higher than the band gap, an electron-hole pair can be excited. Another way is preparing a junction of a N type semiconductor and a P type semiconductor and inducing a gate voltage. Then the former type releases electrons and the latter type releases holes. These electrons and holes meet in the junction between two types of semiconductors and form excitons. Generated excitons decay into photons with finite lifetime. Typical lifetime varies from the order of tenth of nano seconds to micro seconds depending on materials and details of excitonic states. Thus the most important aim of the studies of excitons is understanding the photo-absorption and photo-emission process in solids.

The electron-hole many-body system

Here we give an overview of electron-hole many-body systems in solids. Provided that the total electric charge of the system is zero, a phase diagram of the electron-hole many-body system can be plotted by taking the temperature and electron-hole pair density for two axes. In figure 1.1 we show a phase diagram of an electron-hole many-body system in diamond [1] as an example. Closed circles are experimentally determined phase boundary which corresponds to the transition between the exciton gas phase and the electron-hole plasma (EHP). Closed triangles are experimentally determined density and temperature of the EHL phase. For low pair density and high temperature region, the system is in a gas phase of free excitons. When the density is increased to a sufficiently high value, excitons will ionize due to a screening effect by surrounding excitons. This is the electron-hole plasma phase (EHP). When the system is cooled down, the electron-hole pairs condense to a liquid phase called the electron-hole liquid. We have to note that the phase diagram is affected by details of the system, *e.g.* the electronic band structure, particularly the conduction and valence band degeneracy, and the dimensionality of the crystal.

There are, however, many excitonic phases or excitonic states whose formations are still uncertain. One example is a gas phase of excitonic complex particles, namely charged complexes like trions (exciton + electron(hole)), biexciton (exciton+exciton), or more generally polyexcitons (excitonic n body complexes). These complexes can be considered as intermediate states between the excitonic gas and the electron-hole liquid. Another example is the Bose-Einstein condensation (BEC) of exciton (exciton BEC). The realization of exciton BEC has been one of the biggest goal of this field for a long time. The BEC is a phenomenon where bosonic nature of

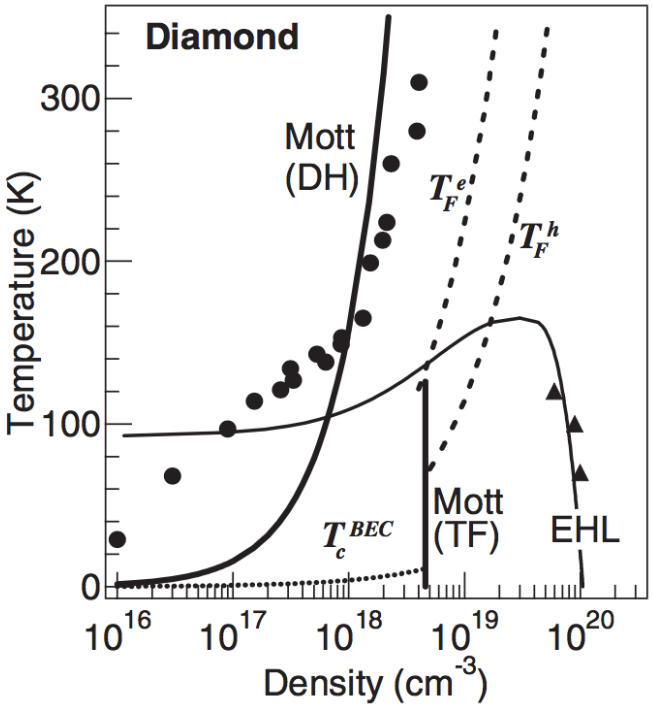

Figure 1.1: A phase diagram of the electron-hole many-body system in diamond [1]. The horizontal axis is the electron-hole pair density and the vertical axis is the temperature of system. The closed circles are the experimentally determined phase boundary between the exciton gas phase and the electron-hole plasma phase. When the density is lower than closed circles the system is in an exciton gas phase, and when it is higher the system is in an electron-hole plasma phase. Closed triangles are experimentally observed density and temperature of the electron-hole liquid (EHL). Theoretically estimated phase boundaries are also shown. The bold curve is the phase boundary between the exciton gas and EHP (Mott(DH)). The bold line is the Mott density given by the Thomas-Fermi screening approximation. The solid curve is the phase boundary of the liquid-gas transition given by Guggenheim's model. The dotted line is the exciton BEC transition temperature. The theoretical phase boundaries show only partial agreement with experimentally observed boundaries.

particles comes out into the macroscopic scale. Thanks to the light mass of excitons compared with that of atoms, excitonic systems have been considered as promising candidates for realizing the BEC. It is because the transition temperature of the BEC is proportional to the inverse of particle mass.

The excitonic complexes

Here we look back on the history of past attempts to explore the possible formation of excitonic complexes in solids. Existence of excitonic particles such as excitons (e^- + hole), charged excitons (trion, exciton + e^-(hole)), and biexcitons under photo-excitation processes is widely accepted by both theorists and experimentalists in many materials. The polyexcitons (PE_n), excitonic n-body complexes are composed of larger number of particles than that of biexcitons. Although there have been several theoretical studies numerically calculating the binding energies of charged biexcitons and smaller complexes in bulk or two-dimensional systems [2]- [3], numerical studies of PE_n ($n > 2$) are still missing except in quantum dots [4].

We need to emphasize the importance of studying the physical properties of excitonic complexes. In principle, they can play an essential role in the multi-photon processes and bring about correlation effects in optical responses of solids. Large excitonic effects in photoluminescence or photo-absorption spectra can be seen not only in bulk systems [5], [1] but also in 2D systems like MoS_2 [6], [7], [8], WSe_2 [9], and WS_2 [10], or lower dimensional systems like quantum dots [11]. A mass excitation of excitons and biexcitons leads to the formation of insulating gas phases in crystals. Phase diagrams of the electron-hole many-body systems are roughly investigated for well-known semiconductors such as silicon [5] or diamond [1]. Identification of possible excitonic bound states is also crucial for complementing and establishing phase diagrams.

The formation of polyexcitons should not be regarded as a trivial phenomenon. For example, the three-body bound state of positronium (Ps_3) was shown to be unstable by a precise numerical calculation [12], and the three-body bound state of hydrogen atom (H_3) is also known to be unstable [13]. Considering from a viewpoint of a mass ratio between a negatively charged particle's mass m_n and a positively charged particle's mass m_p, these studies deny the formation of trimer in two limiting cases, namely $m_n/m_p \to 0$ and $m_n/m_p = 1$. This fact suggests that PE_n for $n > 2$ are expected to be unstable in a wide range of mass ratio in direct gap semiconductors. On the other hand, in the case of indirect gap semiconductors, it has been predicted that degenerate valleys and valence bands can be utilized to avoid the Pauli repulsion between identical fermions, and it may lead to the formation of PE_n. The possible existence of PE_n was first pointed out by a paper of Wang and Kittel [14]. When the number of valley is N, they predicted that PE_{2N} may be formed. They examined the binding energies of polyexcitons in the heavy hole limit $m_e \ll m_h$, where m_e (m_h) is the effective mass of the electron (hole). In this limit they regarded hole as a classical particle and provide binding energies of PE_N for $N \leq 12$ for silicon and $N \leq 8$ for Ge. This approximation for hole is not realistic in solids and hence we cannot directly compare their results with experimentally observed values.

The concept of the PE_n in bulk systems seems to be well accepted. However, experimental signatures of polyexcitons have been reported only in silicon and diamond. These materials are typical indirect gap semiconductors. Steele, McMullan, and Thewalt experimentally observed a series of peaks in the four-particle decay process (two electron-hole pairs decay into one photon)

in high-purity silicon [15], and they attributed the peaks to biexciton decays in PE_n up to $n = 4$. However, due to the indistinct overlapping spectra and the small binding energy of the exciton, controversies occurred about the interpretations of spectrum. For instance, a study proposed an alternative interpretation of the observed spectra by a new type of electron-hole plasma [5], [15] [16]. Two decades later, in diamond, Omachi *et al.* [17] observed six photoemission peaks energetically lower than the single exciton peak and they attributed these peaks to exciton decay in $PE_n (n = 2 - 6)$. Here, the peak positions were precisely observed thanks to the large exciton binding energy in diamond which is several times bigger than that of excitons in silicon.

It is a challenging task to do computational simulations of strongly correlated quantum systems. There are limited number of theoretical studies about polyexcitons. One reason is the high computational cost of treating problems containing more than six particles without using any mean field approach, and other reasons are the complexities of degenerate valleys and bands and the large effective mass anisotropy. Cancio and Chang reported a numerical study treating excitonic complexes such as PE_4 at maximum by the Quantum Monte Carlo method [18]. They employed a spherical effective mass model and a trial wave function that was symmetrized under the permutation of fermions. It clearly violates the fermi statistics of electrons and holes. This treatment possibly provides incorrect binding energies. Accordingly, it has yet remained as an open question that whether the proposed stabilization mechanism [14] really explains the experimental reports [15], [17].

1.2 Theoretical description of excitonic system

In this subsection we briefly introduce two major theoretical frameworks for describing excitonic systems in solids. One framework is a combination of the GW approximation and Bethe-Salpeter equation (BSE), called GW+BSE method, where an exciton is treated as an elementary excitation of the electronic many-body system. The excitonic wave function is expressed by a linear combination of electron-hole pairs. Another framework is the wave function method. In this framework the electrons and holes are treated as independent particles with a unit charge and an effective mass.

Excitons as an elementary excitation of electron many-body system

The GW+BSE method is a kind of first principles many-body perturbation theory and actually a combination of three different theoretical frameworks, the density functional theory (DFT), the GW approximation, and the Bethe-Salpeter equation (BSE). The density functional theory describes the electronic systems as each electron feels an exchange-correlation potential being a functional of electron density distribution. This is one of the most widely used methods to simulate electronic structures of solids, though it has a problem that it largely underestimates band gaps. The GW approximation is an alternative method to solve this problem. This method is classified to a Green's function method, and the electronic system is described by a self consistent eigenvalue equation where the electron-electron interaction is given by a Coulomb potential screened by a medium. The theory of the GW approximation was introduced by Hedin [19]. The GW approximation is known to greatly improve the precision of band gap

estimation, although it is a computationally high costing method. In practical applications, the GW approximation is used to correct the one-particle energy level of the DFT calculation, and the wave function will never be updated. This is called the one-shot GW or G_0W_0 calculation. In spite of this drastic approximation, the energy correction by one-shot GW gives good estimations for values of band gaps in many solids. Hybertsen and Louie reported an early work of first principles calculation using GW approximation [20]. The BSE is an eigenvalue equation of the two-particle correlation function, which provides bound excitonic states within a framework of many-body perturbation theory. Excitonic states are expressed by a linear combination of one-particle electronic states given by the previous GW calculation. This method is known to provide quantitatively good estimation for the optical gap of solids. An early study of first principles calculation based on GW+BSE method is given by Rohlfing and Louie [21]. For carrying out these calculations, we take advantage of widely distributed program package, the *Quantum-ESPRESSO* [22] and the *BerkeleyGW* [23].

Excitonic complexes as an electron-hole few-body system

The fundamental problem of the GW+BSE method is that it is only applicable to the calculation of isolated single exciton, because the Bethe-Salpeter equation is an equation of motion of the two-particle correlation function. An alternative strategy to describe excitonic particles bigger than exciton is using the effective mass theory and directly diagonalizing the total wave function of the electron-hole few-body system. The total function obeys an eigenvalue equation which is given by the almost same analytical expression with the Schrödinger equation in vacuum, except that the mass of the carriers are given by the band dispersion and the Coulomb interaction is screened by a dielectric constant of the medium. Then the polyexcitonic state is given by solving the effective electron-hole few-body problem. Since the essence of the physical mechanism of polyexciton formation is the presence of the orbital degeneracy of the Bloch states, it must be included somehow in our model. The theoretical formalism for including it is first given by Luttinger and Kohn [24] and called the $\boldsymbol{k} \cdot \boldsymbol{p}$ perturbation theory. In this theoretical framework electrons and holes are assumed to be localized in the vicinity of extrema of electronic band structure. In most cases the extrema are on high symmetry points in the Brillouin zone. Small shift of the wave vector from extrema is regarded as a perturbation, then the multiple valley and band degrees of freedom is naturally included. In that case the total wave function of the particles is approximated by a product of an envelope function and the Bloch functions. This theory is well established and some text books are available [25].

Even if we use the effective mass theory, solving the eigenvalue problem to determine the ground state energy of strongly correlated system such as triexciton is computationally high costing. The important point is carefully choosing the numerically efficient basis set. We introduce several types of the major trial function to describe the wave functions of few-body quantum systems. The Hylleraas-type basis function or James-Coolidge-type functions [26] are frequently used types. Firstly it is because they satisfy the cusp condition. This condition is known to restrict the value of $\{\Psi^{-1}(\partial\Psi/\partial r)\}_{r=0}$, where Ψ is the wave function and r is an inter-particle distance. The exact value of $\{\Psi^{-1}(\partial\Psi/\partial r)\}_{r=0}$ is analytically known. Secondly they reproduce the long range behavior of the wave function of Coulombic few body system, decaying as $e^{-\alpha r}$, where α is a constant. On the other hand, they require numerical integrations

for calculating matrix elements of the Coulomb potential, which is computationally high costing. The other possible candidate is the explicitly-correlated-Gaussian (ECG) type basis [27]. The ECG type basis function is given by a Gaussian which depends on relative coordinates like

$$\psi(\boldsymbol{r}) \propto \exp\{-\sum_{i<j}^{N} \frac{1}{2} A_{ij}(\boldsymbol{r}_i - \boldsymbol{r}_j)^2\}, \tag{1.1}$$

where A_{ij} is a variational parameter. Briefly saying it determines the broadening of the Gaussian. A great advantage of the ECG type function is that all matrix elements of Hamiltonian of the Coulombic system can be calculated analytically, even if the effective masses are anisotropic. Considering the fact that the analytical form of the cusp condition has not been revealed in strongly anisotropic systems such as diamond, the ECG basis has a potential to be a more powerful choice.

1.3 Background of exciton confinement techniques

Next, we focus on the excitonic systems from a different view point. As we mentioned above, the technical difficulty of detecting polyexcitonic effects in photoluminescence spectrum is that we need to find weak signals of polyexcitons from much stronger peaks of free excitons and/or EHL. If we can spatially separate the target particles, the experimental detection of their formation will become much easier. Besides it will enable to investigate many-body properties of target particles. Actually there are many theoretical and experimental attempts for controlling excitonic motions in space. Most of them are motivated by a goal of manipulating an ensemble of exciton BEC. In this section we introduce variety of methods proposed so far. For a comprehensive reference, we also introduce preceding studies aiming at the trapping of electrons, holes and exciton-polaritons. The exciton-polariton is a quasi particle composed of a strongly coupled exciton and photon. It is characterized by its extremely light masses which is favorable for BEC. We classify those methods into six types according to its physical mechanisms.

Type I. Applying a local uniaxial strain on crystals – This method applies uniaxial strain on a crystal by using a small tip. The mechanism is that the applied stress locally shrinks the band gap and it works as an effective potential for electrons, holes, and also for excitons. The diameter of tip and the resulting potential is typically around 50μm - 100μm. The potential depth is the order of sub meV. Formation of exciton BEC and exciton-polariton BEC have been reported in this system [28, 29].

Type II. Locally modifying the boundary condition for exciton-polariton by metallic gates –In ordinary cases the exciton-polariton is formed in a layered quantum well where an incident light is perpendicular to stacked layers. In this method small metallic gates are attached on top of the quantum well. The metallic gates modify the boundary condition of incident light and it increase the energy of exciton-polariton. When the gates are periodically placed, it works as an effective periodic potential for exciton-polaritons. A group reported an experimental success of applying this periodic potentials for exciton-polariton BEC [30].

Type III. Utilizing the repulsive potential between spatially indirect excitons – This method is specialized to confine spatially indirect excitons. When two two-dimensional quantum wells are embedded in a substrate and a gate voltage is applied, a potential gradient is formed between

two quantum wells and electrons and holes occupy different quantum well. The spatially indirect exciton is formed by these spatially separated electron and hole. It is known that a repulsive potential works between these spatially indirect excitons [31–33]. This method utilizes this potential. The mechanism is that when the excitons are excited along *e.g.* closed ring-shaped region with high density, it works as repulsive potential walls for excitons in low density region due to the inter-exciton repulsive potential. Several experiments are reporting about the exciton confinement using this technique [31–33].

Type IV. Applying the periodic strain field by using surface acoustic wave (SAW) – The physical mechanism of this method is applying a spatially periodic strain field by using phonons. Especially utilization of surface acoustic wave is proposed [34–36], which is a phonon mode localized near a crystal surface.

Type V. Utilizing the Pauli repulsion between carriers and virtually excited carriers – This method uses the Pauli repulsion between fermionic particles (electrons and holes). Provided that there are excited carriers or excitons in a crystal, then an additional optical field is applied. When the field is tuned as nearly resonant to the optical gap, the excitonic states or electron-hole pair states will be mixed to the electronic states under irradiation. This "virtually" excited excitons or carriers interact with real carriers and excitons via the exchange interaction. It work as a repulsive potential for particles having same spin with that of virtually excited excitons or carriers. This mechanism has been proposed only theoretically [37–40].

Type VI. Utilizing the optical Stark shift driven by a resonance between free carriers and trionic states –This method is specialized for trapping electrons and holes. The physical mechanism is basically same with what is used for trapping atoms in vacuum. In this method an external field which almost resonates with the energy gap between an isolated electron (hole) and a trion is applied. Then the electron (hole) state is mixed with trionic states and an energy shift occurs. This is the optical Stark shift and the magnitude of the shift is proportional to the laser intensity. This method is only proposed by a theoretical work [41].

The optical manipulation techniques of ultra-cold atomic system

When discussing the manipulation techniques for quantum systems, inevitably we need to refer to the field of ultra-cold atomic system. A significant feature of this field is the high ability of designing the quantum systems. Rich applications have been developed such as atomic BEC and the quantum simulator [42, 43]. The central technique supporting the rise of this field is the optical confinement of neutral atoms. Briefly saying this technique is utilizing the energy shift of atoms caused by an irradiation of electromagnetic field which is nearly resonant to the energy gap of atoms. For example, an energy gap between the hydrogen ground state, the $1s$ state and the first excited state, $2p$ state, would be available. We will see the details of its physical mechanism in part II.

The important point is that the mechanism is quite general and, in principle, can be applied to other quantum systems. Since an exciton is a hydrogen-like complex particle, inner excitation levels which correspond to $2s$, $2p$, $3s$, etc. exist. Of course we need to keep it in our mind that the excitation spectrum is more complicated in realistic systems mainly due to the orbital degeneracies and the anisotropy of crystals. Similar mechanism is utilized in the type VI for trapping carriers in semiconductors. It uses resonance between two energy levels, the electronic

ground state and the trionic level in semiconductors. We emphasize that making use of the inner excitation levels seems rather natural since the trapping technique of the ultra-cold atomic system utilize such levels.

1.4 Objectives of this thesis

Here we summarize the goals of this thesis:

- *theoretical investigation of the stability of polyexcitons in diamond* – Considering the above situations we need to give priority to a theoretical investigation of the presence of polyexcitons. The existence of biexcitons or smaller particles have been experimentally and theoretically confirmed. Thus our goal is to examine the formation of triexcitons which is non-trivial in bulk systems. Recently an experimental observation of photo-emission spectrum which is interpreted as a signature of excitonic n-body bound states for $n = 6$ was reported [17]. If the proposed mechanism [14] quantitatively explains the formation of polyexcitons is quite non-trivial. We numerically tackle with this problem by considering the orbital degeneracy in the model.

- *the optical lattice* – We theoretically investigate the feasibility of a technique to confine excitons and/or excitonic complexes in a periodic optical potential. This technique is expected to contribute to experimental studies for physical properties of polyexcitons. The fundamental physical mechanism of this technique is the spatially local energy shift of quantum system induced by the optical Stark effect. The energy shift is roughly proportional to the intensity of laser field which is set to be nearly resonant to a certain excited level. When two counter-propagating laser fields are applied, they form a standing wave which brings about periodic modulation of the field intensity in space. Such periodic modulation effectively works as an array of optical potential : the optical lattice.

- *the optical exciton filter* – We also investigate the feasibility of a state-selective optical trap for excitons and/or excitonic complexes. This is an advanced version of the optical potential. It is quite common situation that the lowest excitonic states are degenerate. It is due to the presence of valence band or conduction band degeneracy. Typical covalent-bond crystals possess this feature. That means different types of excitons are coexisting in the excitonic gas phase. If we can selectively tune the coupling strength between the external laser field and these degenerate excitons, a state-selective optical trapping would be possible.

  One significant feature of these optical manipulation techniques is that the dimensionality and the symmetry of the optical trap or lattice can be almost arbitrarily designed. Another feature is that it doesn't require difficult micro processing techniques. These new techniques will definitely useful not only for the traditional purpose of realizing exciton BEC, but also for exploring the many-body physics of excitonic complexes which is still a frontier of the field of condensed matter physics.

For experimental implementation of these optical techniques, we have to choose a test system so that it satisfies desirable conditions. Firstly the electronic band structure of the test system

is simple for interpreting the results. Secondly the exciton binding energy of the test system is large enough for experimental identification of excitonic levels. By considering these conditions we chose a monolayer graphane. This material is a two-dimensional wide gap semiconductor. Graphane has a simple electronic structure where the conduction band minimum has no degeneracy and the valence band maximum has double degeneracy at Γ point. This degeneracy is originating from a two-dimensional representation of D_{3d} group to which graphane crystal structure belongs. The exciton binding energy of graphane is theoretically reported to exceed 1.5 eV [44]. A physical origin of this huge binding energy is due to the week screening of Coulomb interaction along a direction normal to the crystal.

1.5 Outline of this thesis

This thesis is composed of two parts. In part I we discuss the stability of polyexciton, the n-body complex particle of excitons in diamond. Because the presence of multiple valley and band degrees of freedom is expected to enable the formation of polyexcitons beyond biexcitons, the diamond is a promising material. In chapter 3 we introduce a theoretical framework to describe an electron-hole system with orbital degeneracy, and a concept of explicitly correlated Gaussian (ECG) basis set. We succeeded in showing the stability of several polyexcitonic states – trions, biexcitons, charged biexcitons, and triexcitons. Especially the numerical evidences for the presence of last two complexes (charged biexcitons and triexcitons) in bulk systems are shown for the first time by this work. The results are shown in chapter 4.

In part II we discuss the feasibility of the optical lattice and the optical exciton filter in graphane, a two-dimensional wide gap semiconductor. In chapter 7 we will see the details of the GW+BSE method and the theoretical framework of the formation of an optical potential. Then we show the computed results of the electronic and excitonic structure of graphane in chapter 8. We will see that the lowest five levels of graphane exciton are favorable for implementing the optical potential driven by the infrared light. Also we clarify it is possible to induce state-selective optical potential, the optical filter, by appropriately choosing the direction of circularly polarized light. Lastly we summarize the achievements of our studies and show the future works.

PART I

A numerical investigation of the stability of polyexcitons in diamond

2. OUTLINE OF PART I

In this part we show the numerical evidence for the presence of polyexcitons in solids. The formations of polyexciton (PE_n for $n > 2$) in bulk systems are non-trivial and our results provide an important step to discuss the feasibility of optical manipulation techniques for polyexcitons.

In part I, we theoretically show the stability of excitonic complexes in diamond including the triexcitons at maximum. Chapter 3 is aimed at introducing theoretical framework for describing the electron-hole few-body system. The effective Hamiltonian of this system is given in section 3.1.1. The kinetic energy terms of the Hamiltonian can be derived by using the $\boldsymbol{k}\cdot\boldsymbol{p}$ perturbation theory. The Coulomb interaction between particle is given by an isotropic potential screened by a static dielectric constant of medium. We use experimentally observed values for the effective masses and the dielectric constant. Characteristics of our model Hamiltonian is that the orbital degeneracy of the Bloch states are included as the inner degrees of freedom of particles. We are also considering the effective mass anisotropy. In section 3.2 we introduce the explicitly correlated Gaussian (ECG) basis. The ECG basis states is expressed by a product of a spherical Gaussian factor, a non-spherical factor with finite total angular momentum, spin function, and the Bloch function factors. In section 3.2.1 we explain an algorithm for optimizing the total wave function called the stochastic variational method (SVM). The biggest feature of the SVM is that a parameter set of a basis set is randomly sampled, and the set giving lowest total energy is added to the preexisting basis set.

In chapter 4 we introduce the simulated results. The total energies of excitonic complexes are shown in section 4.1. We calculated the states of excitons, trions, biexcitons, charged biexcitons, and triexcitons. We succeeded in showing the formation of triexcitons when the orbital degeneracy is included in the model. The formation of charged biexcitons and triexcitons in bulk system are the essential consequence of the presence of orbital degeneracy. We will see that the total energies reproduce about 80% of experimental results. We also discuss the separation energies of the excitons, trions (charged exciton), biexcitons, charged biexcitons(CBE), and triexcitons in section 4.2. Here we defined the separation energy as an energy to separate an exciton from a PE_n, trion, and CBE. This is just a comparison with the experimentally observed photoemission spectrum. Our achievement can be a milestone to develop optical techniques for manipulating polyexcitons. The main results of part I was published as a paper [45]. Principal contribution of the author in this study is a development of method. The original program given by the co-authors of [45] only treats isotropic single band models and hence we developed the program to include mass anisotropy and multiple valley and band degrees of freedom.

3. METHOD

3.1 Effective mass theory for the electron-hole system in solids

3.1.1 Hamiltonian of the electron-hole few-body system

One-particle orbitals of diamond have orbital degeneracy at some high-symmetry points in the Brillouin zone. The valence band maximum is triply degenerate and it belongs to $\Gamma_{25'}$ representation of the O_h group and the conduction minimum has six-fold degeneracy on the Δ axes and the one-particle orbitals at these point belong to the Δ_1 representation of the C_{4v} group (See Fig. 3.1). In this thesis we assign the notation Γ_{xy}, Γ_{yz}, Γ_{zx} for one-particle orbitals at the valence band maximum and similarly $\Delta_{(\pm k_c 00)}$, $\Delta_{(0 \pm k_c 0)}$, $\Delta_{(00 \pm k_c)}$ for the six-fold degenerate conduction band minimum. We employed the following $\boldsymbol{k} \cdot \boldsymbol{p}$ effective mass Hamiltonian for an electron-hole system in diamond composed of general $N = N_h + N_e$ particles, where N_h is the number of holes and N_e is the number of electrons. The multiple band and valley degrees of freedom are effectively included in this model as follows:

$$\begin{aligned} \mathcal{H} \quad &= \sum_{i=1}^{N_h} \sum_{\Gamma} t_{h,i}^{(\Gamma)} \cdot |\Gamma_i\rangle\langle\Gamma_i| + \sum_{i}^{N_h} \sum_{\Gamma,\Gamma'} t_{h,i}^{(\Gamma\Gamma')} \cdot |\Gamma_i\rangle\langle\Gamma'_i| \\ &+ \sum_{i=1}^{N_e} \sum_{\Delta} t_{e,i}^{(\Delta)} \cdot |\Delta_i\rangle\langle\Delta_i| + \sum_{i,j}^{N_e,N_h} V_{ij} + \sum_{i<j}^{N_e} V_{ij} + \sum_{i<j}^{N_h} V_{ij}. \end{aligned} \tag{3.1}$$

The first and third terms corresponds to kinetic energy terms of the holes and electrons, respectively. The second term is the inter-band coupling terms which works only on the holes. We will see in the next chapter that the contribution of inter-band coupling in binding energy is negligibly small in the case of excitons with zero center-of mass momentum and hence we will omit it in the calculations of polyexcitons. The last three terms are the isotropic screened Coulomb interaction characterized by the macroscopic dielectric constant ϵ of diamond as follows :

$$V_{ij} = \frac{e_i e_j}{\epsilon r_{ij}}. \tag{3.2}$$

$e_{i(j)}$ is the electric charge of $i(j)$ th particle and r_{ij} is the absolute value of inter-particle distance $r_{ij} = |\boldsymbol{r}_i - \boldsymbol{r}_j|$, where $\boldsymbol{r}_{i(j)}$ is the $i(j)$ th particle's spatial coordinate. In the present notation, the subscripts Γ and Δ run over all six valleys and three bands, respectively. $|\gamma_i\rangle$ ($\gamma = \Delta,\ \Gamma$) is the Bloch function factor of i th particle which satisfies a condition of orthonormality :

$$\langle\gamma_i|\gamma'_i\rangle = \delta_{\gamma_i\gamma'_i}. \tag{3.3}$$

Here we show an example for calculating the kinetic energy term $\sum_\gamma t_{h,i}^{(\gamma)} \cdot |\gamma_i\rangle\langle\gamma_i|$ by a trial wave function $|\psi\rangle = f(\{\mathbf{x}\}) \cdot \prod_{i=1}^{N_e} |\Delta_i\rangle \prod_{i=1}^{N_h} |\Gamma_i\rangle$:

$$\begin{aligned}\langle\psi'|\sum_\gamma t_{h,i}^{(\gamma)} \cdot |\gamma_i\rangle\langle\gamma_i||\psi\rangle &= \sum_\gamma \int d\boldsymbol{r}^{3N} f'(\{\mathbf{x}\}) t_{h,i}^{(\gamma)} f(\{\mathbf{x}\}) \prod_{j=1}^{N_e}\langle\Delta'_j| \prod_{j=1}^{N_h}\langle\Gamma'_j||\gamma_i\rangle\langle\gamma_i| \prod_{j=1}^{N_e}|\Delta_j\rangle \prod_{j=1}^{N_h}|\Gamma_j\rangle \\ &= \int d\boldsymbol{r}^{3N} f'(\{\mathbf{x}\}) t_{h,i}^{(\Gamma_i)} f(\{\mathbf{x}\}) \cdot \delta_{\Gamma'_i\Gamma_i} \prod_{j=1}^{N_e} \delta_{\Delta'_j\Delta_j} \prod_{j(\neq i)}^{N_h} \delta_{\Gamma'_j\Gamma_j}. \end{aligned} \tag{3.4}$$

Here, f is the envelope function factor and $|\Delta\rangle$ and $|\Gamma\rangle$ are the Bloch function factors. $\{\mathbf{x}\}$ is a set of relative coordinates ($\mathbf{x}_i$, $i = 1, \cdots, (N-1)$). We excluded the spin function just for simplicity. Although in practical calculation each basis function is antisymmetrized by applying a particle permutation operator resulting a linear combination of basis function, this example is still general. The analytical form of the kinetic energy terms is given by

$$\begin{cases} t_{h,i}^{(\Gamma_{yz})} = L\frac{\partial^2}{\partial x^2} + M(\frac{\partial^2}{\partial y^2} + \frac{\partial^2}{\partial z^2}) \\ t_{h,i}^{(\Gamma_{zx})} = L\frac{\partial^2}{\partial y^2} + M(\frac{\partial^2}{\partial x^2} + \frac{\partial^2}{\partial z^2}) \\ t_{h,i}^{(\Gamma_{xy})} = L\frac{\partial^2}{\partial z^2} + M(\frac{\partial^2}{\partial x^2} + \frac{\partial^2}{\partial x^2}) \end{cases} \tag{3.5}$$

$$\begin{cases} t_{e,i}^{(\Delta_{(\pm k_c 00)})} = -\frac{1}{2}\{\frac{1}{m_l}\frac{\partial^2}{\partial x^2} + \frac{1}{m_t}(\frac{\partial^2}{\partial y^2} + \frac{\partial^2}{\partial z^2})\} \\ t_{e,i}^{(\Delta_{(0\pm k_c 0)})} = -\frac{1}{2}\{\frac{1}{m_l}\frac{\partial^2}{\partial y^2} + \frac{1}{m_t}(\frac{\partial^2}{\partial x^2} + \frac{\partial^2}{\partial z^2})\} \\ t_{e,i}^{(\Delta_{(00\pm k_c)})} = -\frac{1}{2}\{\frac{1}{m_l}\frac{\partial^2}{\partial z^2} + \frac{1}{m_t}(\frac{\partial^2}{\partial x^2} + \frac{\partial^2}{\partial y^2})\}. \end{cases} \tag{3.6}$$

Similarly, the inter-band coupling terms are given by

$$\begin{cases} t_{h,i}^{(\Gamma_{yz}\Gamma_{zx})} = N\frac{\partial^2}{\partial x \partial y} \\ t_{h,i}^{(\Gamma_{zx}\Gamma_{xy})} = N\frac{\partial^2}{\partial y \partial z} \\ t_{h,i}^{(\Gamma_{xy}\Gamma_{yz})} = N\frac{\partial^2}{\partial z \partial x}. \end{cases} \tag{3.7}$$

We used experimentally observed values for the effective mass parameters and the macroscopic dielectric constant [46]. $L = -2.06$, $M = -4.48$, $N = 5.32$ in units of $\hbar^2/2m_0$, where m_0 is the free electron mass. Similarly, $m_l = 1.56, m_t = 0.280$ in units of m_0, and the dielectric constant is $\epsilon = 5.70$. In Eqs. (3.5) and (3.6), the effective mass along one axis is heavier than along the other directions. Here we call the axis as the heavy mass axis. Then each valley and band is distinguished by the direction of their heavy mass axis.

The spin-orbit splitting on the valence band maximum, the inter-valley scattering effect, and the electron-hole exchange interaction are neglected in our model for simplicity. In diamond, the spin-orbit splitting is 6 meV and the electron-hole exchange interaction is also of the same order [47], and these values are not significant compared with the observed binding energy of exciton in diamond (80 meV [48]). We also made a brief estimation for the magnitude of the inter-valley Coulomb interaction by a simple calculation. The resulting value amounts to 0.9[meV] in the case of diamond (See Appendix C.2). These values are small enough for justifying above approximations neglecting these three effects. Under this approximation, the valley degree of freedom can be regarded as a good quantum number of electrons.

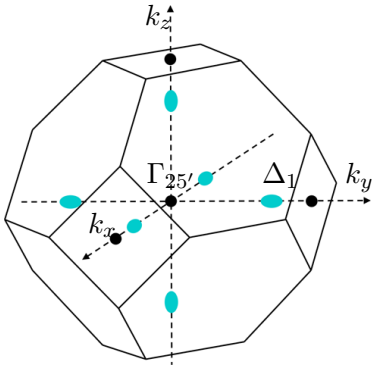

Figure 3.1: A schematic picture of the first Brillouin zone of diamond. The six blue spots denote energetically equivalent valleys on Δ axes.

3.2 Explicitly correlated Gaussian basis set and the stochastic variational method

The principal difficulties of calculating polyexcitons in diamond are the strongly anisotropic energy dispersion of carriers and the high computational cost for treating a strongly correlated system. We use the explicitly correlated Gaussian (ECG) basis in Eq. (1.1) for the trial wave function in this thesis. This is a frequently used type of basis set. As we discussed in the introduction of this part, the Hylleraas-type function and James-Coolidge-type functions [26] may be more frequently used for describing quantum Coulombic few-body systems. These basis sets explicitly depend on the absolute value of the inter-particle distances *e.g.* $r_{12} = |\boldsymbol{r}_1 - \boldsymbol{r}_2|$ as

$$\psi_k \propto r_{12} \exp\{-\alpha_k r_{12}\}. \tag{3.8}$$

Their significant features are (i)they satisfy the so-called "cusp condition" which restricts the value of the derivative of wave function at the origin of inter-particle distance $\Psi^{-1}(\partial\Psi/\partial r)|_{r=0}$, and (ii)they reproduce the exponential decaying behavior of the wave function of the Coulombic few-body system at large inter-particle distances. In particular (i) is expected to greatly reduce the number of basis states. A serious problem of using these basis state is that it requires high computational cost for evaluating matrix elements of Hamiltonian since numerical integrations are needed. On top of that, the analytical form of the exact cusp condition is unknown for anisotropic systems. Therefore, the validity of property (i) are quite uncertain in our case. Turning to the ECG basis state, it reproduces the value of the exact wave function in the vicinity of origin with a sufficient number of basis states and so does for the long range behavior [27], although the ECG basis state in Eq. (1.1) does not satisfy the exact cusp condition. This property would be valid even in the case of the anisotropic Hamiltonian in Eq.(3.1). The biggest advantage of using the ECG basis is that it allows us to compute all matrix elements of the Hamiltonian Eq. (3.1) analytically, and that is the very reason the ECG basis is promising for doing efficient calculations of PE_n $(n > 2)$ in strongly anisotropic systems.

We express the total wave function of a system composed of $N = N_e + N_h$ particles as a linear combination of non-orthogonal ECG basis as $|\Psi\rangle = \sum_k C_k |\psi_k\rangle$ where C_k is a real number expansion coefficient. Each $|\psi_k\rangle$ is factorized into the envelope function $f_k(\{\mathbf{x}\})$, the total spin

function χ_{sm_s}, and the Bloch functions $|\Delta_i\rangle$ and $|\Gamma_i\rangle$ as follows :

$$|\psi_k\rangle = \mathcal{A}\{f_k(\{\mathbf{x}\}) \cdot \chi_{sm_s} \cdot \prod_{i=1}^{N_e} |\Delta_i\rangle \prod_{i=1}^{N_h} |\Gamma_i\rangle\}. \tag{3.9}$$

$\{\mathbf{x}\}$ is a set of relative coordinates introduced below. $|\Delta_i\rangle$ ($|\Gamma_i\rangle$), the Bloch function of the i th electron(hole) satisfies the orthonormality condition Eq. (3.3). $\mathcal{A}$ is an antisymmetrizing operator acting on the trial wave function so that the Fermi statistics is satisfied. For constructing the envelope function, we used the Jacobi coordinate x_i for a set of relative coordinates. It is defined by a linear transformation of one-particle coordinates by

$$\mathrm{x}_i = \sum_{j=1}^{N_e+N_h} U_{ij} \boldsymbol{r}_j, \tag{3.10}$$

where

$$U = \begin{pmatrix} 1 & -1 & 0 & \cdots & 0 \\ m_1/M_2 & m_2/M_2 & -1 & \cdots & 0 \\ m_1/M_3 & m_2/M_3 & \cdots & \cdots & 0 \\ \cdot & \cdot & & & \cdot \\ \cdot & \cdot & & & \cdot \\ \cdot & \cdot & & & \cdot \\ m_1/M_N & m_2/M_N & \cdots & \cdots & m_N/M_N \end{pmatrix}. \tag{3.11}$$

Here M_n is a sum of the geometric mean of the effective mass, *i.e.* $M_n = m_1 + m_2 + \cdots + m_n$

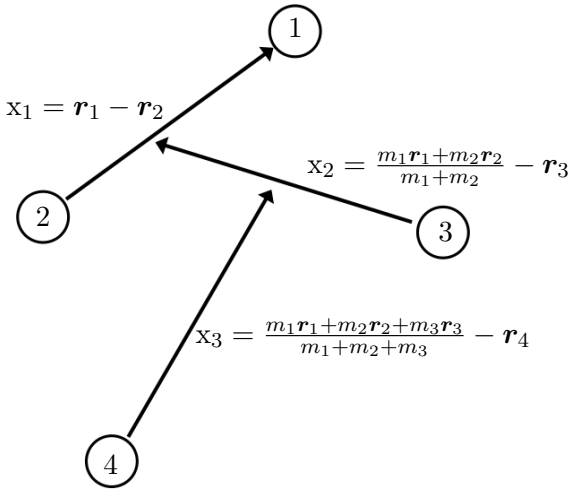

Figure 3.2: Schematic diagram of the way to construct the Jacobi coordinate set in a four-particle system.

and $m_i = \{m_{i,x}m_{i,y}m_{i,z}\}^{1/3}$ where $m_{i,j}$ $(j = x, y, z)$ is the effective mass of i th particle along axis j of Cartesian coordinate and $\boldsymbol{r}_i$ is a one-particle coordinate of i th particle. We show a schematic picture of the way to construct the Jacobi coordinate in figure 3.2. The i th Jacobi coordinate is constructed by subtracting i th one-particle coordinate from the center-of-mass coordinate of $(i-1)$-particle system. In an N-particle system N th Jacobi coordinate gives the

center-of-mass coordinate of the whole system. The envelope function is constructed from the ECG basis [49] by using the Jacobi coordinates as follows :

$$f_k(\{\mathbf{x}\}) = \theta_L(\boldsymbol{v_k}) \cdot \exp\{-\frac{1}{2}\mathrm{xA_kx}\} \tag{3.12}$$

Here $\theta_L(\boldsymbol{v_k})$ possesses a finite total angular momentum L and consists of a real solid spherical harmonic which depends on the *global vector* $\boldsymbol{v} = \sum_{i=1}^{N_e+N_h-1} u_{k,i}\mathrm{x}_i$ [50]. The expansion coefficient $u_{k,i}$ is a variational parameter.

$$\theta_L(\boldsymbol{v}) = \begin{cases} |\boldsymbol{v}|^L\{Y_{LM}(\hat{\boldsymbol{v}}) + Y_{L-M}(\hat{\boldsymbol{v}})\} & (M > 0) \\ i|\boldsymbol{v}|^L\{Y_{LM}(\hat{\boldsymbol{v}}) - Y_{L-M}(\hat{\boldsymbol{v}})\} & (M < 0) \\ |\boldsymbol{v}|^L Y_{LM}(\hat{\boldsymbol{v}}) & (M = 0) \end{cases} \tag{3.13}$$

In Eq. (3.13), $Y_{LM}(\hat{\boldsymbol{v}})$ is a spherical harmonic depending on a unit vector $\hat{\boldsymbol{v}} = \boldsymbol{v}/|\boldsymbol{v}|$. M is z component of the angular momentum. In the envelope function Eq. (3.12), the Gaussian factor is characterized by a variational parameter $\mathrm{A}_{k,ij}$ where $\mathrm{xA_kx} = \sum_{i,j}^{N_e+N_h-1} \mathrm{x}_i\mathrm{A}_{k,ij}\mathrm{x}_j$. The ECG basis has been used to obtain accurate energies for many different few-body systems [49]. Superposition of different angular-momentum states is aimed at describing the orbital deformation of the envelope function caused by the strong effective mass anisotropy. We fixed the total spin quantum number of the trial wave function as a singlet in neutral (or even particle number) systems and 1/2 in charged (or odd particle number) systems.

3.2.1 Parameter optimization

To optimize the trial wave function given in the previous subsection, we employed an algorithm called "stochastic variational method" (SVM) [51]. In the SVM, the number of basis states is increased one by one up to an arbitrary number, and in each increasing step the variational parameters $u_{k,i}$ and $\mathrm{A}_{k,ij}$ are randomly sampled and a parameter set which provides lowest energy is added to existing basis set. The original SVM is composed of the following two processes.

(i)*Increasing process.* Assume that there are K basis states with the ground state energy E_K. Firstly P basis states are randomly generated within a range of physically reasonable parameter values. New ground state energies are calculated by using existing K basis states plus one of the newly generated P basis states. Then new P ground state energies E_i $(i = 1, \cdots, P)$ are given. The $(K+1)$ th basis state is chosen so that it gives the lowest ground state energy among P ground state energies, and is added to the existing K basis states. This increasing process is repeated until the number of basis states reaches a predetermined number which is chosen so that the binding energy converges within the desired accuracy. In the case of our thesis, we repeatedly increased the maximum number of basis states until predetermined precision was achieved.

(ii)*Refinement process.* In this process, the parameter set of the K-dimensional basis set is improved by alternating basis states by new states which provides lower energy. The dimension of basis set K is given by the process (i) and the value of dimension is kept unchanged through this process. Firstly P' basis states are randomly generated as alternative states for the k-th basis states $(1 \leq k \leq K)$. Then new ground state energies E_i $(i = 1, \cdots, P')$ are given by

replacing the k-th basis state by the alternatives. If the energy which is lowest among the newly calculated E_i $(i = 1, \cdots, P')$ is lower than that of the original basis set, the existing k-th basis state is altered by the new basis state. This procedure is repeated for $k = 1, \cdots, K$.

After the operation of refinement process, an energy improvement less than 0.1% is reported for a ground state calculation of positronium molecule [52]. We also confirmed energy improvements by 0.04% after applying refinement process twice for a case of positronium molecule with zero total angular momentum and 50 basis states. We obtained the convergence of binding energies within 1 % in the following results without imposing the process (ii), and it is sufficiently accurate to show the stability of excitonic complexes. In the following section we show the energies calculated only by using the process (i). Typical number of basis states in our calculations ranged from 50 to 100 in excitons and from 1000 to 1800 in triexcitons. Computational time was about one month for longest case of triexciton calculation by serial calculation in our machine (CPU is Intel X5570).

4. RESULTS AND DISCUSSIONS

4.1 Stability of polyexcitons

4.1.1 Contribution of the inter-band coupling to exciton binding energies

For a verification of the accuracy of present method, we first applied it for estimating exciton binding energies in GaN with anisotropic effective masses with no orbital degeneracy. In this calculation two types of hole are considered: the light and heavy hole. Each type has different effective mass anisotropy. Here we defined the exciton binding energy as an energy required to separate an exciton into a free electron-hole pair. We obtained 24.809 meV for a heavy-hole exciton, 15.445 meV for a light-hole exciton, respectively. These values are in excellent agreement with earlier theoretical binding energies obtained by exact diagonalization of a single-band electron-hole effective mass Hamiltonian [53]: 24.809 meV for the heavy-hole exciton, 15.458 meV for the light-hole exciton, respectively.

Before showing the binding energies of excitons in diamond, we investigate the contribution of the inter-band coupling Eq. (3.7) to the binding energy. Since any inter-band coupling is proportional to $\frac{\partial^2}{\partial x_i \partial x_j}$ ($x_{i(j)=x,y,z}$, $x_i \neq x_j$), two orbitals with different parity cannot be coupled with each other. In addition, s-type orbitals are not coupled with one another due to the symmetry. And also from the parity conservation, d-type orbitals are the lowest finite angular-momentum states which can be coupled with s-type orbitals. More specifically, matrix elements of the inter-band coupling between two angular momentum eigenstates $|lm\rangle$ and $|l'm'\rangle$ are non-zero only if $|l'm'\rangle$ satisfies the condition:

$$\begin{cases} t_{h,i}^{(\Gamma_{yz}\Gamma_{zx})} & : |l'm'\rangle = |l\ m \pm 2\rangle,\ |l \pm 2\ m \pm 2\rangle \\ t_{h,i}^{(\Gamma_{xz}\Gamma_{xy})} & : |l'm'\rangle = |l\ m \pm 1\rangle,\ |l \pm 2\ m \pm 1\rangle \\ t_{h,i}^{(\Gamma_{xy}\Gamma_{yz})} & : |l'm'\rangle = |l\ m \pm 1\rangle,\ |l \pm 2\ m \pm 1\rangle. \end{cases} \tag{4.1}$$

Figs. 4.1(a) shows interconnection between s- and five d-type orbitals. If a matrix elements of the kinetic energy term and inter-band coupling term gives non-zero value, two orbitals are connected by a solid line and a dotted line, respectively. As a test case, we compare the following two trial functions to see the contribution of the inter-band coupling terms.

$$\begin{cases} \text{(i)}\{f_s + f_{d_{z^2+c}} + f_{d_{x^2-y^2}}\}|\Delta_{(0k_c0)}\rangle|\Gamma_{xy}\rangle + f_{d_{zx}}|\Delta_{(0k_c0)}\rangle|\Gamma_{yz}\rangle + f_{d_{xy}}|\Delta_{(0k_c0)}\rangle|\Gamma_{zx}\rangle \\ \text{(ii)}\{f_s + f_{d_{z^2+c}} + f_{d_{x^2-y^2}}\}|\Delta_{(00k_c)}\rangle|\Gamma_{yz}\rangle \end{cases} \tag{4.2}$$

Here f is the envelope function and $|\Delta\rangle$ and $|\Gamma\rangle$ are the Bloch function factors of trial wave function. The subscripts of the envelope function f denote the orbital type of the real number solid spherical harmonic. Eqs. (4.2)(i) corresponds to the second cluster from the right hand side in Figs. 4.1(a). It forms a fully connected cluster and completely separated from others.

Eqs. (4.2)(ii) corresponds to the same cluster but no inter-band coupling is concerned. In the above expressions, we omitted the spin function for simplicity. We obtained the binding energy from the trial wave function in Eqs. (4.2)(i) as 67.7 meV and in Eqs. (4.2)(ii) as 67.9 meV. The energy improvement from the inter-band coupling amounts to only 0.3 %. The contributions from the second and third terms in Eqs. (4.2)(i) are small enough to be neglected. In the following calculations, we therefore omit the inter-band coupling. Then each bound state is characterized by a single product of the Bloch states, an envelope function, and a spin function such as shown in Eqs. (4.2)(ii). Hereafter we denote a combination of valleys and bands by, for example $\Delta_{(00k_c)}/\Gamma_{yz}$ in the case of Eqs. (4.2)(ii).

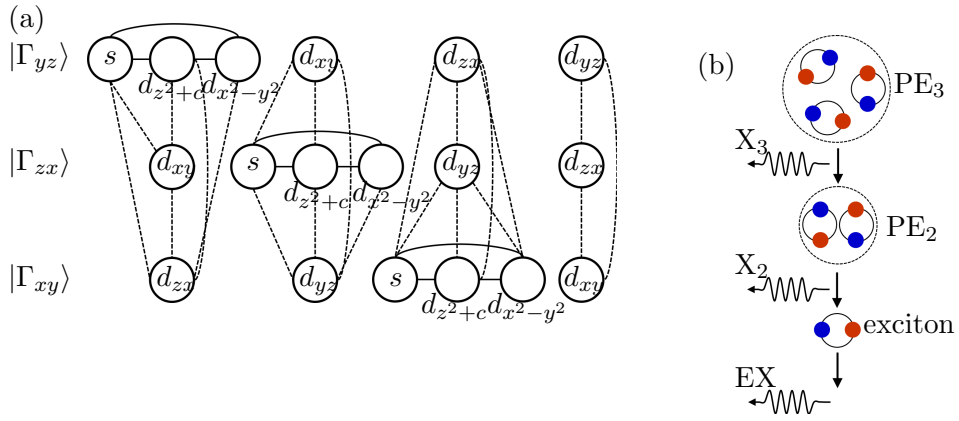

Figure 4.1: (a)Diagrammatic expression of interconnections between orbitals by the kinetic energy (solid lines) and inter-band coupling (dotted lines) of the Hamiltonian Eq. (3.1). Orbitals in the first, second and third rows corresponds to the envelope function of the $|\Gamma_{yz}\rangle$, $|\Gamma_{zx}\rangle$ and $|\Gamma_{xy}\rangle$ bands. (b)Schematic picture of the exciton decay processes in polyexcitons (PE$_n$). X$_3$ and X$_2$ are photons emitted from exciton recombination in PE$_3$ and PE$_2$, respectively. EX is photoemission from a free exciton recombination.

4.1.2 Experimentally observed binding energy of polyexciton

Now we introduce our method of estimating the binding energies of polyexcitons from the experimentally observed photoluminescence spectrum. Omachi *et al.* [17] observed five peaks (X$_2$ – X$_6$) below the peak of the free exciton recombination(EX) in the photoluminescence spectrum. They attributed X$_n$(n = 2 – 6) to exciton decays in PE$_n$. Fig. 4.1(b) is a schematic diagram of the process. The energy gap

$$S_{\mathrm{PE}_n} = E_{\mathrm{X}_n} - E_{\mathrm{EX}} \tag{4.3}$$

is interpreted as the energy to separate PE$_n$ into PE$_{n-1}$ and an isolated exciton. Here E_{X_n} and E_{EX} are energies of the peak X$_n$ and a photon emitted from the free exciton recombination process, respectively. According to the paper of Omachi *et al.*, $S_{\mathrm{PE}_2}/R = 0.15$, and $S_{\mathrm{PE}_3}/R = 0.31$, where $R = 80$ meV is the binding energy of a free exciton. Then the binding energy of a biexciton E_{biex} and a triexciton E_{triex} can be calculated as $E_{\mathrm{biex}} = 2R + S_{\mathrm{PE}_2} = 172$ meV, $E_{\mathrm{triex}} = E_{\mathrm{biex}} + R + S_{\mathrm{PE}_3} = 277$ meV.

4.1.3 Stability of excitonic complexes in diamond

We show the total binding energies of excitons in Figs. 4.2(a). Here, we defined the total binding energy as an energy which is required to separate an excitonic complex into free electrons and holes. Resulting values are 71.8 meV for the combination of $\Delta_{00k_c}/\Gamma_{xy}$ (black broken line) and 67.7 meV for the combination of $\Delta_{00k_c}/\Gamma_{zx}$(black solid line). The energy gap between these two states is attributed to the difference of heavy effective mass axis of the Γ_{xy} band and the Γ_{zx} band. These results amount to 90% and 85% of the experimentally observed value (80 meV [48]), respectively. These are sufficiently accurate values to obtain bound states of triexcitons as we will see later.

The energy discrepancy between the calculated and experimentally observed values may possibly due to the approximations in our model where the electron-hole exchange interaction and the weak screening of Coulomb interaction in short distance are omitted. By including those effects, we can expect that the former effect reduce the exciton binding energy since the exchange interaction lowers the binding energy of singlet excitons, whereas the latter should increase the binding energy as the net Coulomb attraction is enhanced.

Although the inter-valley scattering effect by phonon may also be present, quantitative estimation of the sum of these correction exceeds the ability of our model.

In the case of the trions, we depicted the threshold energies in Fig. 4.2 for the sake of eye guide to see the stability of trions. If the binding energy of trions are smaller than the threshold energy, the trion is unstable and will spontaneously dissociate into an exciton and a free electron or a free hole. The total binding energies and threshold energies of the trion$^+$ and trion$^-$ are shown in Figs. 4.2(b) and (c), respectively.

The number of possible combinations of valleys and bands inequivalent under the symmetry operations are six for trion$^+$ and four for trion$^-$. The averaged binding energies are 72.6 meV for trion$^+$ and 73.1 meV for trion$^-$. These results show that trion binding energies are insensitive to the huge discrepancy of the carrier effective masses. We also depicted the threshold energies for trion$^+$ and trion$^-$ by black solid lines and broken lines in Fig. 4.2. The averaged binding energy of the trion$^+$ and trion$^-$ are 105% and 106% of the exciton binding energy, and these values are close to the results of an earlier theoretical study for trions with isotropic effective mass [2]. There is no experimentally observed value comparable for the trion in diamond, to our knowledge. Note that the arrangement of the energy levels in Fig.2 is reflecting the effect of the mass anisotropy but is not firm: If the omitted effects (the spin-orbit coupling, intervalley Coulomb interaction etc.) are considered, the degeneracy and order of levels possibly be rearranged.

Next, we show the binding energies of biexcitons, charged biexcitons (CBE$^+$ and CBE$^-$), and triexcitons in Figs. 4.3(a)–(d). Depending on the combination of orbital degrees of freedom, the binding energies of biexcitons vary from 140 meV to 148 meV, that amount to 83% of the experimentally observed value on average. In the case of triexcitons, the binding energies reproduce 81% of the experimental value on average, and vary within a range from 223 meV to 229 meV. The calculated biexciton binding energies showed that all combinations of valleys and bands allows formation of biexciton rather than dissociating into a pair of free excitons. The stabilization of charged biexcitons and triexcitons is considered to be unique in systems having the orbital degeneracy and hence has a great significance. In direct gap semiconductors

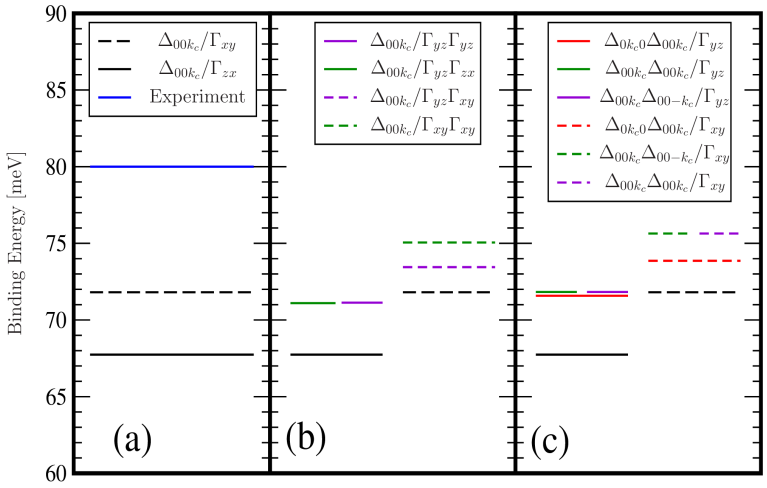

Figure 4.2: (a)Binding energies of excitons [45]. Black lines are calculated values. Blue solid line is the experimentally observed value [48]. (b)Binding energies of trion$^+$ (exciton + hole) [45]. Black solid lines show threshold energy of dissociation into a pair of a free exciton and a hole for $\Delta_{00k_c}/\Gamma_{yz}\Gamma_{yz}$ and $\Delta_{00k_c}/\Gamma_{yz}\Gamma_{zx}$. Black broken lines show threshold energies of dissociation into a pair of free exciton and a hole for $\Delta_{00k_c}/\Gamma_{yz}\Gamma_{xy}$ and $\Delta_{00k_c}/\Gamma_{xy}\Gamma_{xy}$. Colored lines are calculated values. (c)Binding energies of trion$^-$ (exciton + electron) [45]. Black solid lines and black broken lines are threshold energies of dissociation into a pair of free exciton and an electron.

without any band degeneracy, the triexcitons are predicted to be unstable because of the Pauli blocking effect. According to an earlier accurate numerical calculation [2], the charged biexciton is known to be unstable unless the condition $\sigma = m_e/m_h < 0.2$ is satisfied. If we take the geometric mean of effective masses of electron and hole in diamond as $m^* = \{m_x m_y m_z\}^{1/3}$, the effective mass ratio becomes $\sigma = m_h^*/m_e^* = 0.58$ and does not satisfy this condition. Our results of triexciton and charged biexciton binding energies in Fig. 4.3(d) are the first numerical evidence supporting the presence of the triexcitons and charged biexcitons in semiconductors possessing orbital degeneracy.

We also emphasize that we got unbound states for the case of the charged biexciton and triexciton when the three identical particles occupy same single valley or band. For example, when two electrons occupy valleys on $\Delta_{(00k_c)}$ and $\Delta_{(00-k_c)}$, and all three holes occupy Γ_{yz} band, CBE$^+$ is not formed. This calculation condition corresponds to the case of a single band system and does not contradict with the results of the earlier calculations [2]. This is indicating that the stability of charged biexcitons and triexcitons originates from the multiple valley and band degrees of freedom. We summarize values of polyexciton binding energies in appendix D for all inequivalent combination of valleys and bands. Furthermore the variation of energy levels originating from the effective mass anisotropy of the respective valleys or bands is also an important outcome. The width of the energy level distribution varies from about 4 meV to 8 meV depending on the combinations of orbital degrees of freedom. We expect that the width of the binding energy distribution affects the shape of the experimental photoemission spectra. In the next subsection, we will do further discussions about the separation energies to see this effect.

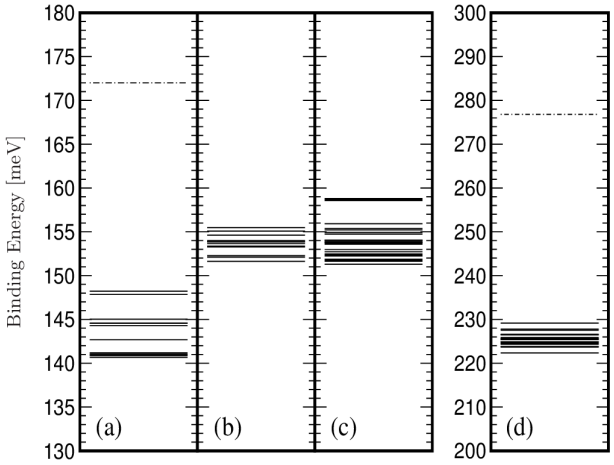

Figure 4.3: Binding energies of (a)biexciton, (b)CBE$^+$(biexciton + hole), (c) CBE$^-$(biexciton + electron), and (d)triexciton [45]. Solid lines are the calculated binding energy. The dashed-dotted line is the binding energy of the biexciton calculated from experimentally observed peak positions in the photoluminescence spectrum [17].

4.2 Separation energy

For a direct comparison with the experimentally observed photoemission spectra, we calculate the separation energies. We defined the separation energy S_{PE_n} is as a minimum energy required to separate PE_n into a PE_{n-1} and a free exciton as follows:

$$E_{\mathrm{PE}_n} = E_{\mathrm{PE}_{n-1}} + E_{\mathrm{exciton}} + S_{\mathrm{PE}_n}, \tag{4.4}$$

where E_{PE_n}, $E_{\mathrm{PE}_{n-1}}$, and E_{exciton} are binding energies of a PE_n, PE_{n-1}, and an exciton, respectively. In the cases of trion and CBE,

$$E_{\mathrm{trion}^\pm} = E_{\mathrm{e}^-(\mathrm{hole})} + E_{\mathrm{exciton}} + S_{\mathrm{trion}^\pm} \tag{4.5}$$

$$E_{\mathrm{CBE}^\pm} = E_{\mathrm{trion}^\pm} + E_{\mathrm{exciton}} + S_{\mathrm{CBE}^\pm}. \tag{4.6}$$

Here $E_{\mathrm{e}^-(\mathrm{hole})}$ is the energy of free electron or hole, and we set it to be zero in our calculation. $E_{\mathrm{trion}^\pm}$ and $E_{\mathrm{CBE}^\pm}$ are the binding energies of the trion$^\pm$ and CBE$^\pm$, respectively. We assumed that the valley and band degrees of freedom are unchanged under the dissociation processes. S_{PE_n} corresponds to the energy gaps between experimentally observed peak positions in exciton recombination spectra X_n in PE_n as defined in section 4.1.2. Calculated separation energies are shown in Fig. 4.4. The black solid lines are separation energies of PE_n and charged bound states. We can see that the separation energies are distributed within a certain energy range whose width is few meV in Fig. 4.4, similarly with the biexciton binding energies in Fig. 4.3. To compare with the experimentally observed values, we emphasize the value of the most stable biexciton($\Delta_z\Delta_z/\Gamma_{xy}\Gamma_{xy}$) and triexciton($\Delta_z\Delta_z\Delta_{-z}/\Gamma_{xy}\Gamma_{xy}\Gamma_{yz}$) in our calculations by green diamonds (See Appendix B). These values are most likely to be measured if the most stable states are solely formed. This is justified in the low-temperature limit and when the difference of the transition probability to the respective states is negligibly small. Nevertheless, we also show the separation energies calculated for the other biexciton/triexciton states to imply the possible

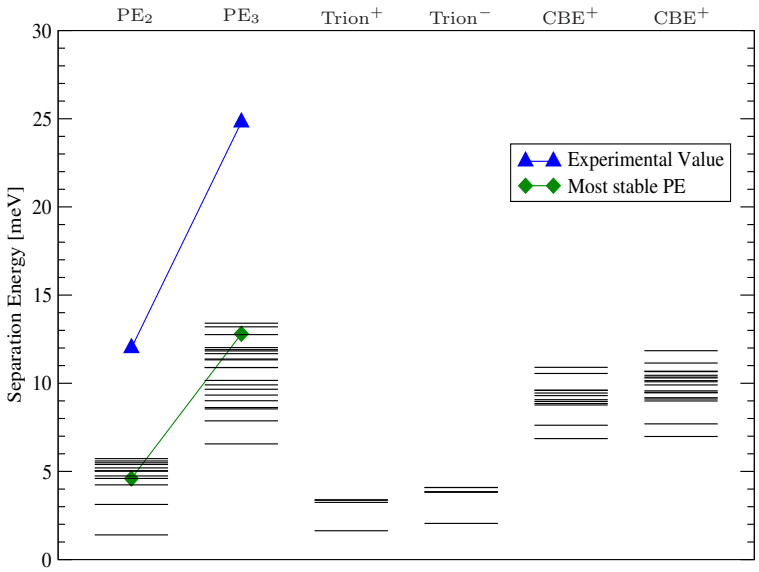

Figure 4.4: Separation energies of PE_n(n = 2,3,4), Trions (trion$^{+,-}$)), and Charged Biexcitons (CBE$^{+,-}$)) [45]. The black lines are values calculated from the theoretical binding energies. The green diamonds are those for most stable polyexcitons. The blue triangles are the experimentally observed values [17].

broadening of the measurable peaks due to the occupations of various combinations of the valley and band degrees of freedom. Here we didn't consider the excited states for the respective combinations. We also simply ignore the possible difference in the transition probability. The separation energies for most stable PE_n amount to 38% and 52% of the experimental values for PE_2 and PE_3, respectively. See Table 4.1 and green diamonds in Fig. 4.4. The ratio S_{PE_3}/S_{PE_2} gives 136% of the experimental value and hence our results agree qualitatively well with the experimental values. S_{PE_2} can be physically interpreted as the strength of inter-exciton bonding. A resulting fact that S_{PE_3} is almost two times larger than S_{PE_2} suggests a simple picture that three excitons are weakly bound with each other to form PE_3.

	S_{PE_2}[meV]	S_{PE_3}[meV]	S_{PE_3}/S_{PE_2}
Calculated Value	4.60	12.8	2.79
Experimental Value	12.0	24.8	2.06

Table 4.1: Comparison of calculated and experimentally observed value [17] of the separation energy S_{PE_n} for $n = 2, 3$ [45].

We can make two predictions by comparing the separation energy distribution with the photoluminescence spectra. Firstly the experimentally observed photoemission spectrum of PE_2 and PE_3 (*i. e.* X_2 and X_3) possibly contain photoemission spectrum originating from the trion and CBE, respectively. Secondly, in addition to the temperature of the excitonic complex gas, the separation energy distribution also contributes to the peak width of EX and X_n.

This is because the distribution of the separation energy is roughly interpreted as that of the peak position of the X_n in the photoluminescence spectrum, since the separation energies has a correspondence with the energy gap between the peak positions of the free exciton emission

(EX) and the complex particle decay (X_n). In particular the second point will make it tough to isolate the broadening effect of the temperature of the excitonic complex gas from the peak width of X_n. We also have to note that the effects ignored in our model, such as the inter-valley Coulomb interaction, would have contribution of similar order with the width of separation energy distribution(See Appendix C.2). It will cause the rearrangement of levels and possibly expand their width by a few meV.

5. SUMMARY OF PART I

In part I, we investigated the stability of excitonic complexes in diamond by numerical simulations. Its purpose is verifying the validity of the proposed stabilization mechanism [14] where the multiple valley and band degrees of freedom play a central role. The orbital degeneracy of the Bloch states in diamond was included in our model based on the $\boldsymbol{k} \cdot \boldsymbol{p}$ perturbation theory. The spin-orbit coupling, electron-hole exchange interaction, and the inter-valley Coulomb interaction were neglected for simplicity. The explicitly correlated Gaussian (ECG) basis was used for the accurate description of the total wave function. The ECG basis set has been used for precise calculations of binding energies in many few-body systems [49]. For including the anisotropic mass effect and multiple band and valley degrees of freedom, we developed a program given by co-authors in [45] which originally treats isotropic single band models.

We successfully showed the stability of triexciton and charged biexciton. The stabilization of these particles is one of the most significant consequences of the multiple valley and band degrees of freedom in bulk semiconductors. We obtained 81% to 90% of the experimentally observed binding energies of PE_n, and 113% of the separation energy ratio $S_{\mathrm{PE}_3}/S_{\mathrm{PE}_2}$. These results support the presence of polyexcitons which were hitherto suggested only through experimental observations.

We also clarified the stability of smaller excitonic complexes such as excitons, trions, biexcitons, and charged biexcitons. However, the formation of trion$^{\pm}$ and CBE$^{\pm}$ is not yet verified by experiments using diamond. In addition we analyzed separation energies. The results indicate that peak positions of an electron-hole pair recombination in trion$^{\pm}$ and CBE$^{\pm}$ will be adjacent to those of biexcitons and triexcitons respectively, in the photoemission spectrum. Experimental observations of these charged species in photoluminescence spectrum probably be feasible. One possible way is applying a gate voltage for injecting excess carriers in a doped environment so that excitons and biexcitons capture an extra particle and form trions and charged biexcitons [54], [55].

PART II

A theoretical investigation of an optical potential and an optical exciton filter for excitons in graphane

6. OUTLINE OF PART II

Part II of this thesis is the theoretical investigation of the feasibility of optical techniques to control exciton motion in solids. We propose two types of such techniques – the optical lattice and the optical filter. The former technique traps excitons in a periodic optical potential and the latter technique traps selected type of exciton. The ultimate goals of this part is to show in what conditions such optical techniques can be feasible. Not only the laser intensity, polarizability and the possible depth of potential, but also an important side effect of heating by the radiation pressure is examined. There is also a problem of how to simulate the excitonic states which are essential to evaluate physical quantities such as coupling strength between external fields. Thus a combination of different theoretical frameworks must be used for discussing the feasibility of those techniques, and they are basically independent with each other.

Here we introduce the structure of this part. Chapter 7 is devoted to explain theoretical methods. In the section 7.1 firstly we derive the physical mechanism to implement the optical potential in a quantum system. More specifically the interaction Hamiltonian between matter and light in section 7.1.1, and the three distinct mechanisms of emergence of optical potentials: far off-resonant system where the energy shift is obtained by a diagonal perturbative correction (7.1.2), and nearly on-resonant two-level system (7.1.3), and the nearly on resonant three-level system (7.1.4). We are keeping applications to excitons in our mind, but those theoretical frameworks are quite general and applicable to quantum system possessing a group of few discrete levels, except that the external field is treated as classical electromagnetic field and the translational motion of the particles is not considered. In section 7.2 we introduce theoretical frameworks to discuss the heating effect by the radiation pressure. Since the coupling between a quantum system and light mixes higher energy levels, it essentially accompanies spontaneous emission of photons. In this event a quantum system receives finite momentum and it results in the heating of the quantum system. To include this effect the electromagnetic field must be quantized. In section 7.2.1 we derive a master equation of the density matrix of a quantum system driven by a quantized coherent laser field. Several important approximations are introduced in this section such as the Born-Markov approximation which greatly simplifies the treatment of quantized electro-magnetic field. In this framework the lifetime of excitation is naturally introduced. In section 7.2.2 an approximate treatment of the heating process by radiation pressure is given. By calculating a stationary solution of the master equation of density matrix, we can obtain the population of excited states. The above framework is well established method and we summarized based on [42, 43]. By multiplying the lifetime of excitation levels and the recoil energy to the population of excitation level, we can approximately estimate the kinetic energy income per unit time. We finally introduce an approximate treatment of the cooling process by phonon-emission process in section 7.3. When the heating is balanced with the cooling process, we can briefly estimate the equilibrium temperature of the system. This is

based on the methodology of [41]

After the introduction of theories describing the light-matter interaction, we introduce the first principles method to simulate the excitonic states. As we mentioned in the introduction of this thesis, there are a couple of theories to describe excitonic systems in solids. Although our ultimate goal is the optical manipulation of excitonic complexes, we give priority to calculating excitonic states by quantitatively most reliable methods. It is because these optical techniques are newly proposed in excitonic systems. Thus we chose first principles method, the GW+BSE method for describing excitonic systems. In section 7.4, we briefly introduce three deferent method. The density functional theory (7.4.1), the GW approximation (7.4.2), and the Bethe-Salpeter equation (7.4.2). The DFT provides orbital functions of the system based on a self-consistent eigenvalue equation where the electron-electron interaction is given by a functional of the electron density distribution. Though it provides good estimations of lattice structures in many compounds, the band gap is sometimes greatly underestimated. To solve this problem, we apply a Green's function method called the GW approximation. It describes the electron-electron interaction by a screened Coulomb interaction and greatly improve the problem of band gap underestimation. Basically the GW approximation provides an equation of motion for the one-particle Green's function which must be solved self consistently. But in our thesis we use the so-called one-shot GW or G_0W_0 method which does not update the wave function. It is known that this treatment still provides good estimation for the band gap. The previous DFT calculation give the wave function as an input of the GW calculation. Lastly we solve the Bethe-Salpeter equation by using the orbital function by DFT calculation and the one-particle energy levels by GW calculation as inputs. The BSE is an equation of motion of the two-particle correlation function and provides excitonic states of solids, and we can obtain the wave function of excitons as an amplitude of electron-hole pair excitation states.

In chapter 8 we show the results in the case of graphane, the two-dimensional wide gap semiconductor. The graphane is synthesized by reacting graphene with hydrogen. The graphane has a good test case for several reasons. The simple electronic structure, huge excitonic binding energy, and the current absence of techniques for trapping excitons different from bulk systems. In section 8.1 we show the computed results of electronic band structure, and the excitonic spectrum. Simulated crystal structure shows good agreement with preceding studies, though the electronic band gap by GW approximation show relatively large discrepancy with recently reported values. The cause is considered to be the extremely small number of empty bands used to calculate GW energy correction in those studies. In spite of such discrepancy the exciton binding energy well agrees. By calculating the transition dipole moment between excitonic states, we clarify that the lowest five excitonic levels can be decomposed into two almost independent two-level-system and one three-level system. In section 8.2 we discuss the feasibility of the optical lattice in graphane. As a result we see the possible depth of the potential will be sub meV under the irradiation of laser field of typical intensity in the trapping experiments of cold atom systems. We also see the optical filter can be implemented by tuning the polarizability and the incident angle of laser light. In section 8.4 we examine the heating effect of radiation pressure. By analyzing the damping constant between excitonic states and the electronic ground states, it turns out that the heating effect cannot be serious as long as we try to trap spin-singlet excitons.

7. METHOD

7.1 Exciton dressed state and optical potential

In this section we introduce theoretical frameworks to derive optical potential for quantum system driven by an external electromagnetic field. The derivation is well-established and based on textbooks [42, 43]. In 7.1.1 we introduce a fundamental Hamiltonian which describes the interaction between matter and light. Several important approximations like the dipole approximation which neglects the spatial dependency of the external field is introduced. In 7.1.2 we examine a problem of far-off-resonant system. In this case the energy shift originating from the light-matter coupling is just given by a second order perturbation. The energy shift is called the *AC Stark shift* that provides the simplest form of optical potential. In 7.1.3 we treat a non-degenerate two-level system by a non-perturbative method. The time-evolution of the system and its stationary solution are well understood by using an idea of *pseudospin* description. This is more precise treatment than 7.1.2 and being capable of describing on-resonant case. In 7.1.4 we teat a three-level system where two of the levels are degenerate. Though the pseudospin description is difficult in this case, the Hamiltonian is easily diagonalized and we can see obvious correspondence with the result of two-level system. This three-level system plays an essential role to induce state-selective optical potential for excitonic system.

7.1.1 Light-matter Interaction

This subsection is aimed at introducing how we treat the interaction between light and matter. We derive one-body Hamiltonian for an electron by using dipole approximation. The starting point of the derivation is a well-known form of Hamiltonian for an electron in electromagnetic field:

$$H = \frac{1}{2m}\{\boldsymbol{p} - e\boldsymbol{A}(\boldsymbol{r},t)\}^2 + e\phi(\boldsymbol{r},t) + U_I(\boldsymbol{r}). \tag{7.1}$$

Here m is the free electron mass, $\boldsymbol{p}$ is the momentum operator, $\boldsymbol{A}$ is the vector potential, ϕ is the scalar potential, e the charge of electron, and U_I is the ion potential. $\boldsymbol{A}$ and ϕ satisfy the Maxwell equation in Coulomb gauge :

$$(\nabla^2 - \frac{1}{c^2}\frac{\partial^2}{\partial t^2})\boldsymbol{A}(\boldsymbol{r},t) = \boldsymbol{0}, \tag{7.2}$$

$$(\nabla^2 - \frac{1}{c^2}\frac{\partial^2}{\partial t^2})\phi(\boldsymbol{r},t) = 0, \tag{7.3}$$

$$\boldsymbol{E}(\boldsymbol{r},t) = -\frac{\partial}{\partial t}\boldsymbol{A}(\boldsymbol{r},t) - \nabla\phi, \tag{7.4}$$

$$\boldsymbol{B}(\boldsymbol{r},t) = \nabla \times \boldsymbol{A}(\boldsymbol{r},t). \tag{7.5}$$

$\boldsymbol{A}$ and ϕ also satisfy following relations:

$$\nabla \cdot \boldsymbol{A}(\boldsymbol{r},t) + \frac{1}{c^2}\frac{\partial}{\partial t}\phi = 0 \tag{7.6}$$

$$\nabla \cdot \boldsymbol{A}(\boldsymbol{r},t) = 0. \tag{7.7}$$

By utilizing the gauge invariance and an assumption that the system is vacuum, we can further simplify the equations. With a gauge transformation :

$$\boldsymbol{A} \to \boldsymbol{A}' = \boldsymbol{A} + \nabla\chi, \tag{7.8}$$

$$\phi \to \phi' = \phi - \frac{\partial}{\partial t}\chi, \tag{7.9}$$

$$\frac{\partial}{\partial t}\chi = \phi, \tag{7.10}$$

where χ satisfies :

$$(\nabla^2 - \frac{1}{c^2}\frac{\partial}{\partial t^2})\chi = 0, \tag{7.11}$$

ϕ vanishes from Eq. (7.1) and Eq. (7.5). This is known as the *radiation gauge*.

In the next step, we introduce a quantized radiation field. Then the $\boldsymbol{A}$, and also $\boldsymbol{E}$ in Eq. (7.5) are the field operator given by:

$$\boldsymbol{A}(\boldsymbol{r},t) = \sum_{\boldsymbol{k}} \left(\frac{\hbar}{2\omega_k \epsilon_0}\right)^{1/2} (\hat{a}_{\boldsymbol{k}} \boldsymbol{u}_{\boldsymbol{k}} e^{-i\omega_{\boldsymbol{k}} t} + \hat{a}^\dagger_{\boldsymbol{k}} \boldsymbol{u}^*_{\boldsymbol{k}} e^{i\omega_{\boldsymbol{k}} t}) \tag{7.12}$$

$$\boldsymbol{E}(\boldsymbol{r},t) = i\sum_{\boldsymbol{k}} \left(\frac{\hbar\omega_{\boldsymbol{k}}}{2\epsilon_0}\right)^{1/2} (\hat{a}_{\boldsymbol{k}} \boldsymbol{u}_{\boldsymbol{k}} e^{-i\omega_{\boldsymbol{k}} t} - \hat{a}^\dagger_{\boldsymbol{k}} \boldsymbol{u}^*_{\boldsymbol{k}} e^{i\omega_{\boldsymbol{k}} t}). \tag{7.13}$$

Here the mode function $\boldsymbol{u}_{\boldsymbol{k}}$ is defined as :

$$\boldsymbol{u}_{\boldsymbol{k}}(\boldsymbol{r}) = \frac{1}{\sqrt{V}} \boldsymbol{e}^{(\lambda)} e^{i\boldsymbol{k}\cdot\boldsymbol{x}}. \tag{7.14}$$

V is the system volume. $\boldsymbol{e}^{(\lambda)}$ is a polarization vector and λ is an index of polarization. $\boldsymbol{u}_{\boldsymbol{k}}$ and $\boldsymbol{e}^{(\lambda)}$ obey the orthonormal relation:

$$\int_V \boldsymbol{u}^*_{\boldsymbol{k}} \cdot \boldsymbol{u}_{\boldsymbol{k}'} = \delta_{\boldsymbol{k}\boldsymbol{k}'},\ \boldsymbol{e}^{(\lambda)*} \cdot \boldsymbol{e}^{(\lambda')} = \delta_{\lambda\lambda'}. \tag{7.15}$$

Since $\nabla \cdot \boldsymbol{A}(\boldsymbol{r},t) = 0$ and $\nabla \cdot \boldsymbol{u}_{\boldsymbol{k}} = 0$, $\boldsymbol{e}_{\boldsymbol{k}}$ satisfies a condition $\boldsymbol{k} \cdot \boldsymbol{e}^{(\lambda)} = 0$. $\hat{a}_{\boldsymbol{k}}$ and $\hat{a}^\dagger_{\boldsymbol{k}}$ are the annihilation and creation operator, respectively. The first and second term of Eq. (7.13) can be interpreted as an annihilation and creation process of a quanta of light, the photon.

Now we introduce simpler form by assuming that the system we focused on is much smaller than the wave length $\lambda = 2\pi/|\boldsymbol{k}|$ of light. Then we can approximate the plane wave factor of the mode function Eq. (7.14) by

$$e^{i\boldsymbol{k}\cdot\boldsymbol{x}} \simeq 1. \tag{7.16}$$

This is the *dipole approximation*. We perform further gauge transformation:

$$\boldsymbol{A} \to \boldsymbol{A}' = \boldsymbol{A} + \nabla\chi,\ \phi \to \phi' = \phi - \frac{\partial}{\partial t}\chi, \text{where } \chi = -\boldsymbol{r}\cdot\boldsymbol{A}. \tag{7.17}$$

With this approximation and transformation, the Hamiltonian Eq. (7.1) becomes

$$H = \frac{1}{2m}(\boldsymbol{p} - e\boldsymbol{A})^2 + U_I \tag{7.18}$$

$$\simeq \frac{1}{2m}\boldsymbol{p}^2 + e\boldsymbol{r}\cdot\boldsymbol{E} + U_I. \tag{7.19}$$

Let us assume that now the total system is a direct product of matter field $|\Psi\rangle$ and monochromic laser field which can be well approximated by a *coherent state* $|\alpha_{\boldsymbol{k}}\rangle$, where $|\alpha_{\boldsymbol{k}}\rangle$ satisfies

$$\hat{a}_{\boldsymbol{k}}|\alpha_{\boldsymbol{k}}\rangle = \alpha_{\boldsymbol{k}}|\alpha_{\boldsymbol{k}}\rangle. \tag{7.20}$$

By sandwiching the Hamiltonian Eq. (7.19) with $|\alpha_{\boldsymbol{k}}\rangle$, we get the final form:

$$H = \frac{1}{2m}\boldsymbol{p}^2 + U_I + e\boldsymbol{r}\cdot(\varepsilon\boldsymbol{e}e^{-i\omega t} + \varepsilon^*\boldsymbol{e}^*e^{i\omega t}), \tag{7.21}$$

where we defined

$$\varepsilon\boldsymbol{e} \equiv i\left(\frac{\hbar\omega}{2\epsilon_o}\right)\alpha\boldsymbol{u}. \tag{7.22}$$

Although the introduction of the field might seem superfluous, it provides a starting point to discuss the effect of spontaneous photoemission process. Details of the process will be explained in the next section.

7.1.2 AC Stark shift

In this subsection we derive a static energy shift driven by an external electromagnetic field, the *AC Stark Shift*. The physical origin of the AC Stark shift is the perturbative contribution from off-resonant levels coupled by the field. For deriving such perturbative energy correction, firstly we expand the wave function of matter $|\Psi\rangle$ by the eigenstates of the Hamiltonian $H_0 = \frac{1}{2m}\boldsymbol{p}^2 + U_I$ as

$$|\Psi\rangle = \sum_n a_n(t)|n\rangle, \text{ where } H_0|n\rangle = \hbar\omega_n|n\rangle. \tag{7.23}$$

The initial condition is $a_n(0) = \delta_{ng}$. We assume that the external field $\boldsymbol{E}(t)$ is immediately turned on at $t = 0$ hence $\boldsymbol{E}(t) = 0$ for $t \leq 0$. Index g indicates the ground state. The equation of motion for $a_n(t)$ is given by

$$i\hbar\frac{\partial}{\partial t}a_n(t) = \langle k|H|\Psi(t)\rangle = \hbar\omega_{\boldsymbol{k}}a_m(t) + \sum_n \boldsymbol{d}_{mn}\cdot\boldsymbol{E}(t)a_n(t), \tag{7.24}$$

where $\boldsymbol{d}$ is the transition dipole moment

$$\boldsymbol{d}_{mn} \equiv e\langle m|\boldsymbol{r}|n\rangle. \tag{7.25}$$

A convenient transformation $a_n(t) = \tilde{a}_n(t)e^{-i\omega_n t}$ simplifies the Eq. (7.24) as

$$\frac{\partial}{\partial t}\tilde{a}_n(t) = -\frac{i}{\hbar}\sum_m \boldsymbol{E}(t)\cdot\boldsymbol{d}_{nm}\tilde{a}_m(t)e^{-i\omega_{mn}t}. \tag{7.26}$$

Here $\omega_{nm} \equiv \omega_n - \omega_m$. By integrating Eq. (7.26) for $t_1 \in [t', t]$ ($t' < 0$), we obtain

$$\tilde{a}_n(t) = -\frac{i}{\hbar}\sum_{m\neq g}\int_{t'}^{t} dt_1 \boldsymbol{d}_{nm}\cdot\boldsymbol{E}(t_1)\tilde{a}_m(t_1)e^{i\omega_{nm}t_1} - \frac{i}{\hbar}\int_{t'}^{t} dt_1 \boldsymbol{d}_{ng}\cdot\boldsymbol{E}(t_1)\tilde{a}_g(t_1)e^{i\omega_{ng}t_1}. \quad (7.27)$$

Provided that $|\omega - \omega_{nm}| \gg |\omega - \omega_{ng}|$ for any n and m ($n, m \neq g$), we can omit rapidly oscillating term. Thus

$$\tilde{a}_n(t) \simeq -\frac{i}{\hbar}\int_{t'}^{t} dt_1 \boldsymbol{d}_{ng}\cdot\boldsymbol{E}(t_1)\tilde{a}_g(t_1)e^{i\omega_{ng}t_1}, \quad (7.28)$$

and also assume that $\tilde{a}_g(t)$ varies much slower than oscillating factors, we can extract $\tilde{a}_g(t)$ from integration, then

$$\tilde{a}_n(t) \simeq -\frac{i}{\hbar}\tilde{a}_g(t)\int_{t'}^{t} dt_1 \boldsymbol{d}_{ng}\cdot\boldsymbol{E}(t_1)e^{i\omega_{ng}t_1}. \quad (7.29)$$

By substituting this result into the equation of motion for $\tilde{a}_g(t)$,

$$\begin{aligned}\frac{\partial}{\partial t}\tilde{a}_g(t) &= -\frac{i}{\hbar}\sum_n \boldsymbol{E}(t)\cdot\boldsymbol{d}_{gn}e^{i\omega_{gn}t}\tilde{a}_n(t) & (7.30)\\ &\simeq -\frac{i}{\hbar}\tilde{a}_g(t)\sum_n \frac{2\omega_{gn}}{\omega^2-\omega_{gn}^2}|\varepsilon\boldsymbol{e}\cdot\boldsymbol{d}_{gn}|^2. & (7.31)\end{aligned}$$

In the second line, we omitted rapidly oscillating terms proportional to $e^{-i2\omega t}$ and $e^{2i\omega t}$. This result means that a time independent and spatially localized energy shift δE_g, where

$$\delta E_g = \sum_n \frac{2\omega_{gn}}{\omega^2-\omega_{gn}^2}|\varepsilon\boldsymbol{e}\cdot\boldsymbol{d}_{gn}|^2, \quad (7.32)$$

appears for a far-off-resonant system. We preliminarily noted that we are focusing on the energy shift for the ground state, but the current derivation is valid for arbitrary levels as long as it is off resonant. This effect is called the *AC Stark shift*. When the intensity of field varies spatially slowly, the energy shift also varies and provides effective potential for electronic systems.

7.1.3 Two-level system

In this subsection our purpose is to introduce a way to treat on-resonant ($\omega - \omega_{nm} = 0$) or nearly on-resonant ($\omega - \omega_{nm} \simeq 0$) system. Now we focus on an on-resonant system with two levels $|k\rangle$ and $|l\rangle$, where $\omega_k > \omega_l$ and $|\omega - \omega_{kl}| \sim 0$. A schematic diagram is shown in figure 7.1.

Contribution from off-resonant levels can be treated as the static energy shift just as given in the previous subsection. Then the equation of motion for the two-level system is:

$$\begin{aligned}i\hbar\frac{\partial}{\partial t}a_k(t) &= (\hbar\omega_k + \delta E_k)a_k(t) - \boldsymbol{d}_{kl}\cdot\boldsymbol{\epsilon}\varepsilon e^{-i\omega t}a_l(t) & (7.33)\\ &= \hbar\omega_k' a_k(t) - \boldsymbol{d}_{kl}\cdot\boldsymbol{\epsilon}\varepsilon e^{-i\omega t}a_l(t) & (7.34)\\ i\hbar\frac{\partial}{\partial t}a_l(t) &= (\hbar\omega_l + \delta E_k)a_l(t) - \boldsymbol{d}_{lk}\cdot\boldsymbol{\epsilon}^*\varepsilon^* e^{i\omega t}a_k(t) & (7.35)\\ &= \hbar\omega_l' a_l(t) - \boldsymbol{d}_{lk}\cdot\boldsymbol{\epsilon}^*\varepsilon^* e^{i\omega t}a_k(t). & (7.36)\end{aligned}$$

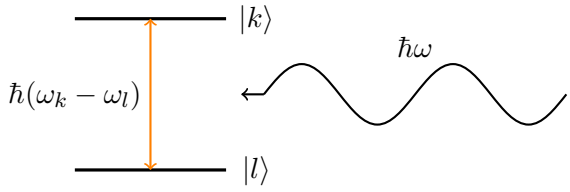

Figure 7.1: A schematic picture of a two-level system driven by an electromagnetic field with energy $\hbar\omega$ per single photon. $\hbar\omega$ is took as nearly resonant with the energy gap $\hbar(\omega_k - \omega_l)$.

In this case, the AC Stark Shift is given by

$$\delta E_k = \sum_{n\neq l} \frac{2\omega_{kn}}{\omega^2 - \omega_{kn}^2} |\varepsilon \boldsymbol{e} \cdot \boldsymbol{d}_{kn}|^2 \tag{7.37}$$

$$\delta E_l = \sum_{n\neq k} \frac{2\omega_{ln}}{\omega^2 - \omega_{ln}^2} |\varepsilon \boldsymbol{e} \cdot \boldsymbol{d}_{ln}|^2 \tag{7.38}$$

Next we transform the expansion coefficients in a similar way with the previous subsection :

$$a_k(t) = \tilde{a}_k(t) e^{-i(\omega+\omega_l')} \tag{7.39}$$

$$a_l(t) = \tilde{a}_l(t) e^{-i\omega_l' t}. \tag{7.40}$$

With this transformation, we obtain well known *Rabi Hamiltonian* H_{Rabi} as follows:

$$i\hbar \frac{d}{dt} \begin{pmatrix} \tilde{a}_k \\ \tilde{a}_l \end{pmatrix} = H_{\text{Rabi}} \begin{pmatrix} \tilde{a}_k \\ \tilde{a}_l \end{pmatrix}, \tag{7.41}$$

$$H_{\text{Rabi}} = \hbar \begin{pmatrix} -\Delta & -\boldsymbol{d}_{kl} \cdot \boldsymbol{\epsilon}\varepsilon/\hbar \\ -\boldsymbol{d}_{lk} \cdot \boldsymbol{\epsilon}^* \varepsilon^*/\hbar & 0 \end{pmatrix}, \tag{7.42}$$

and the Hamiltonian is not time dependent any more. Here we used the *rotational wave approximation* that neglects rapidly oscillating terms with frequency $\pm 2\omega$. Those rapidly oscillating terms correspond to a process of simultaneous matter excitation and photon emission, or simultaneous matter deexcitation and photon absorption. We defined two parameters that play central roles to characterize this two-level system as follows:

$$\text{Rabi frequency} : \Omega_R \equiv \left| \frac{2\varepsilon \boldsymbol{d}_{kl} \cdot \boldsymbol{\epsilon}}{\hbar} \right|, \tag{7.43}$$

$$\text{detuning} : \Delta \equiv \omega - \omega_{kl}', \ (\omega_{kl} = \omega_k' - \omega_l'). \tag{7.44}$$

Pseudospin formalism

We have to note again that our goal is to find stationary solution for Eq. (7.41). To find the solution, it is convenient to introduce the idea of pseudospin space for figuring out how the Rabi

Hamiltonian Eq. (7.42) evolve the two-level system. Here we transform Eq. (7.42) into the Pauli matrix expression:

$$H_{\mathrm{Rabi}} = -\frac{\hbar}{2}(\Delta + \Omega_{\mathrm{eff}}\boldsymbol{n}\cdot\boldsymbol{\sigma}) \tag{7.45}$$

$$\Omega_{\mathrm{eff}}\boldsymbol{n} = (\mathrm{Re}\{\boldsymbol{d}_{kl}\cdot\boldsymbol{\epsilon}\varepsilon\}, \mathrm{Im}\{\boldsymbol{d}_{kl}\cdot\boldsymbol{\epsilon}\varepsilon\}, \frac{1}{2}\Delta). \tag{7.46}$$

$\boldsymbol{n}$ is a unit vector and $\boldsymbol{\sigma}$ is the Pauli matrix:

$$\sigma_x = \begin{pmatrix} 0 & 1 \\ 1 & 0 \end{pmatrix},\ \sigma_y = \begin{pmatrix} 0 & -i \\ i & 0 \end{pmatrix},\ \sigma_z = \begin{pmatrix} 1 & 0 \\ 0 & -1 \end{pmatrix}. \tag{7.47}$$

The state vector

$$\begin{pmatrix} \tilde{a}_k \\ \tilde{a}_l \end{pmatrix} = \begin{pmatrix} \cos(\Theta(t)/2)e^{-i\Phi(t)/2} \\ \sin(\Theta(t)/2)e^{i\Phi(t)/2} \end{pmatrix} \tag{7.48}$$

is regarded as a pseudospin. We also introduce the *Bloch vector* $\boldsymbol{s}(t)$:

$$\rho(t) = \frac{1}{2}(1 + \boldsymbol{s}(t)\cdot\boldsymbol{\sigma}), \tag{7.49}$$

$$\boldsymbol{s}(t) = (\sin(\Theta(t))\cos(\Phi(t)), \sin(\Theta(t))\sin(\Phi(t)), \cos(\Theta(t))), \tag{7.50}$$

where ρ is a density matrix:

$$\rho(t) = \begin{pmatrix} \tilde{a}_k \\ \tilde{a}_l \end{pmatrix} \begin{pmatrix} \tilde{a}_k^* & \tilde{a}_l^* \end{pmatrix}. \tag{7.51}$$

Bloch sphere and Bloch equation

The Bloch vector can be mapped on a three dimensional sphere as illustrated in Figure (7.2), which is called the *Bloch sphere*. The equation of motion of the Bloch vector is given by calculating the time derivative of the density matrix Eq. (7.49) as follows:

$$i\hbar\frac{\partial}{\partial t}\rho(t) = [H_{\mathrm{Rabi}}, \rho(t)] \tag{7.52}$$

$$i\hbar\frac{\partial}{\partial t}\rho(t) = \frac{i\hbar}{2}\dot{\boldsymbol{s}}(t)\cdot\boldsymbol{\sigma} \tag{7.53}$$

$$[H_{\mathrm{Rabi}}, \rho(t)] = -i\hbar\Omega_{\mathrm{eff}}(\boldsymbol{n}\times\boldsymbol{s}(t))\cdot\boldsymbol{\sigma}, \tag{7.54}$$

which leads to

$$\dot{\boldsymbol{s}}(t) = -\Omega_{\mathrm{eff}}(\boldsymbol{n}\times\boldsymbol{s}(t)). \tag{7.55}$$

To derive Eq. (7.54), we used a formula for the Pauli matrices:

$$(\boldsymbol{\sigma}\cdot\boldsymbol{A})(\boldsymbol{\sigma}\cdot\boldsymbol{B}) = \boldsymbol{A}\cdot\boldsymbol{B} + i\sigma\cdot(\boldsymbol{A}\times\boldsymbol{B}), \tag{7.56}$$

where $\boldsymbol{A}$ and $\boldsymbol{B}$ are vectors containing only c-number components. The equation of motion Eq. (7.55) is the well-known *Bloch equation*.

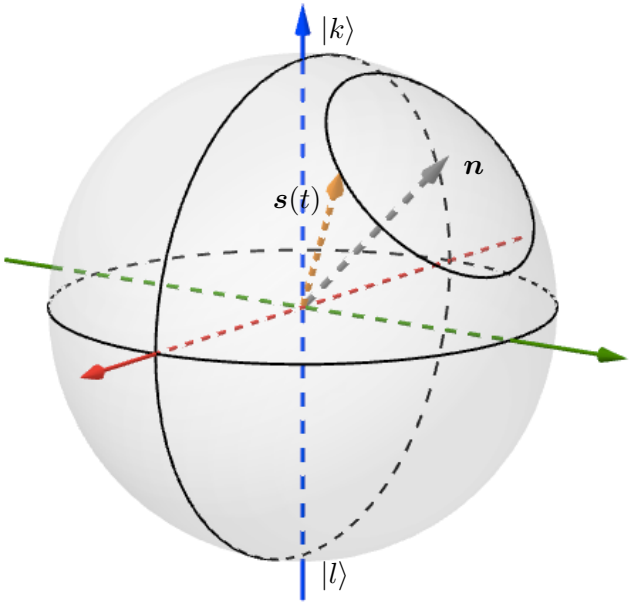

Figure 7.2: The Bloch Sphere and the Bloch vector (orange arrow). The Rabi Hamiltonian Eq. (7.42) rotates the Bloch vector $\boldsymbol{s}(t)$ about the vector $\boldsymbol{n}$.

Stationary solution of the Rabi Hamiltonian : the dressed state

The time evolution operator of the system is given by

$$\exp\{-iH_{\text{Rabi}}t/\hbar\} = e^{i\Delta t/2}\exp\{\frac{1}{2}i\boldsymbol{n}\cdot\boldsymbol{\sigma}\Omega_{\text{eff}}t\} \tag{7.57}$$

It is clearly shown that the Rabi Hamiltonian rotates the pseudospin by the angle of $\Omega_{\text{eff}}t$ around the axis $\boldsymbol{n}$. The polar notation of $\boldsymbol{n}$ is convenient to see this rotation.

$$\boldsymbol{n} \equiv -(\sin\theta\cos\phi, \sin\theta\sin\phi, \cos\theta) \tag{7.58}$$

$$\tan\theta = -\frac{\Omega_R}{\Delta},\ \sin\theta = \frac{\Omega_R}{\sqrt{\Delta^2+\Omega_R^2}},\ \cos\theta = -\frac{\Delta}{\sqrt{\Delta^2+\Omega_R^2}} \tag{7.59}$$

$$\Omega_{\text{eff}} = \sqrt{\Omega_R^2+\Delta^2} \tag{7.60}$$

ϕ is the phase of laser field. Now we can easily find the stationary solution of this system, since the Bloch equation Eq. (7.55) shows no time-evolution when the vectors $\boldsymbol{n}$ and $\boldsymbol{s}$ are parallel or anti-parallel with each other. Namely, Θ and Φ must be

$$(\Theta,\Phi) = \begin{cases} (\theta,\phi) \\ (\pi-\theta,\pi+\phi) \end{cases}. \tag{7.61}$$

By substituting these values, we can get two eigenstates:

$$|+\rangle = -\sin\frac{\theta}{2}e^{-i\phi/2}|k\rangle + \cos\frac{\theta}{2}e^{i\phi/2}|l\rangle, \tag{7.62}$$

$$|-\rangle = \cos\frac{\theta}{2}e^{-i\phi/2}|k\rangle + \sin\frac{\theta}{2}e^{i\phi/2}|l\rangle. \tag{7.63}$$

These states are known as the *dressed states*, and the eigenvalues are given by

$$E_{\pm} = -\frac{1}{2}\hbar\left\{\Delta \pm \sqrt{\Delta^2 + \Omega_R^2}\right\}. \tag{7.64}$$

When the field intensity varies very slowly in space, the eigenvalues also varies in space, and it effectively works as an optical potential for a particle. This is the mechanism of how the optical potential emerges. By neglecting the spatially constant part the optical potential is given by:

$$U_{op}^{(\pm)} = \mp\frac{\hbar}{2}(\sqrt{\Delta^2 + \Omega_R^2} - \sqrt{\Delta^2}) \tag{7.65}$$

$$\simeq \mp\frac{\hbar\Omega_R^2}{4|\Delta|} \text{ (for } \Delta \gg \Omega_R). \tag{7.66}$$

Since the energy correction from AC Stark Shift also depends on the field intensity, the detuning Δ also depends on the particle coordinate. By explicitly writing down the coordinate dependency, the eigenvalue of dressed state can be expressed by:

$$E_{\pm} = -\frac{1}{2}\hbar\{\Delta(\boldsymbol{r}) \pm \sqrt{\Delta(\boldsymbol{r})^2 + \Omega_R(\boldsymbol{r})^2}\}. \tag{7.67}$$

7.1.4 Three-level system

Three-level system, or sometimes called Λ-configuration system is also important for inducing a state-selective optical potential. Here we show a schematic diagram of this system in figure (7.3). We again express the total wave function of the system by a linear combination of the three

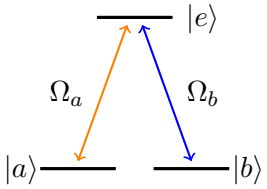

Figure 7.3: Schematic picture of the λ configuration system. The level $|a\rangle$ and $|b\rangle$ are almost degenerate. Ω_a and Ω_b scale the coupling strength between $|e\rangle$ and these two levels.

levels:

$$|\Psi\rangle = a_a(t)|a\rangle + a_b(t)|b\rangle + a_e(t)|e\rangle. \tag{7.68}$$

Then the Hamiltonian of this system is given by a tridiagonal matrix and the Scrödinger equation becomes

$$i\hbar\frac{d}{dt}\begin{pmatrix} a_a(t) \\ a_e(t) \\ a_b(t) \end{pmatrix} = \hbar\begin{pmatrix} \omega_a & \Omega_a e^{i\nu_a t}/2 & 0 \\ \Omega_a^* e^{-i\nu_a t}/2 & \omega_e & \Omega_b e^{i\nu_b t}/2 \\ 0 & \Omega_b^* e^{-i\nu_b t}/2 & \omega_b \end{pmatrix}\begin{pmatrix} a_a(t) \\ a_e(t) \\ a_b(t) \end{pmatrix}. \tag{7.69}$$

Here ν_a and ν_b are the frequency of two driving fields, respectively. To eliminate the explicit time-dependency of Equation (7.69), we transform $a_i (i = a, b, e)$ as

$$\tilde{a}_a(t) = a_a(t)e^{-i(\nu_a+\Delta+\omega_e)} \tag{7.70}$$

$$\tilde{a}_b(t) = a_b(t)e^{-i(\nu_b+\Delta+\omega_e)} \tag{7.71}$$

$$\tilde{a}_e(t) = a_e(t)e^{-i(\Delta+\omega_e)}, \tag{7.72}$$

then we can get a time-independent Hamiltonian

$$i\frac{d}{dt}\begin{pmatrix}\tilde{a}_a(t)\\ \tilde{a}_e(t)\\ \tilde{a}_b(t)\end{pmatrix} = \begin{pmatrix}0 & \Omega_a/2 & 0\\ \Omega_a^*/2 & -\Delta & \Omega_b/2\\ 0 & \Omega_b^*/2 & 0\end{pmatrix}\begin{pmatrix}\tilde{a}_a(t)\\ \tilde{a}_e(t)\\ \tilde{a}_b(t)\end{pmatrix}. \tag{7.73}$$

This is easily diagonalized and its eigenvalues and corresponding eigenvectors are given by

$$E = 0, -\frac{\hbar}{2}(\Delta \pm \Omega_{\text{eff}}) = E_0, E_\pm \tag{7.74}$$

and

$$u_0 = (-\Omega_b, 0, \Omega_a^*)/C_0,\ u_\pm = (\Omega_a, \Delta \pm \Omega_{\text{eff}}, \Omega_b^*)/C_\pm, \tag{7.75}$$

where C_0 and $C_\pm$ are normalization constants and $\Omega_{\text{eff}} \equiv \sqrt{\Delta^2 + |\Omega_a|^2 + |\Omega_b|^2}$. Obviously the $u_\pm$ corresponds to the dressed state of two-level system. Similarly we can induce the optical potential for these two states as

$$U_{op}^{(\pm)} = \mp\frac{\hbar}{2}\{\sqrt{\Delta^2 + |\Omega_a|^2 + |\Omega_b|^2} - \sqrt{\Delta^2}\}. \tag{7.76}$$

7.2 Radiation pressure and heating

The purpose of this section is to introduce the important side effects, the heating process due to *radiation pressure force*. The physical origin of this process is the momentum transfer from emitted/absorbed photons from excitons. Heating rate is directly related to the occupation probability of the excited states, and the *Optical Bloch equation* provides a way to evaluate such quantity. Our first task is introducing the *quantum stochastic Schrödinger equation* that also provides theoretical fundamentals to discuss the collective behavior of exciton gas driven by external field in the next section. Then we directly develop the optical Bloch equation from the quantum stochastic Schrödinger equation and extract its stationary solution.

7.2.1 The Quantum Stochastic Schrödinger equation and Lindblad Master equation

Hamiltonian

Hereafter the total system is made up of the matter and light field. Then the total Hamiltonian is given by

$$H_{total} = H_{sys} + H_{EM} + H_{int}. \tag{7.77}$$

The matter Hamiltonian H_{sys} in this case have a special form for systems with two or more levels:

$$H_{sys} = \hbar\sum_i(\omega_{e_i}|e_i\rangle\langle e_i| + \omega_{g_i}|g_i\rangle\langle g_i|) \tag{7.78}$$

with $\omega_0 = \omega_{e_i} - \omega_{g_j}$ for any i. The electromagnetic field Hamiltonian is

$$H_{EM} = \sum_{|\omega_k - \omega_0| < \theta} \hbar \omega_k b_k^\dagger b_k. \tag{7.79}$$

The frequency range θ, namely *coupling bandwidth* is much smaller than ω_0. The interaction Hamiltonian is

$$H_{int}^{(\theta)}(t) = i\hbar \sum_{|\omega_k - \omega_0| < \theta} (\kappa_k^* b_k^\dagger c - \kappa b_k c^\dagger). \tag{7.80}$$

κ_k is a coupling constant between matter and an electromagnetic field with wave vector k. Here c, $c^\dagger$ is defined to satisfy a commutation relation:

$$[H_{sys}, c] = -\hbar\omega_0 c, \tag{7.81}$$

as

$$c = \sum_i r_i |g_i\rangle\langle e_i|, \; c^\dagger = \sum_i r_i^* |e_i\rangle\langle g_i|. \tag{7.82}$$

r_i and r_i^* are the relative strength of the coupling between two level $|e_i\rangle$ and $|g_i\rangle$.

The Born-Markov Approximation

To construct a perturbation theory we introduce definitions of some quantities and approximations. The interaction picture is convenient to discuss the perturbation. The interaction picture is constructed from the wave function $|\Psi, t\rangle_S$ and operators O_S in Schrödinger picture as follows:

$$O_I(t) = U_I^\dagger(t) O_S U_I(t) \tag{7.83}$$

$$|\Psi_I, t\rangle = U_I(t) |\Psi, t\rangle_S \tag{7.84}$$

$$U_I(t) = \exp\{-\frac{i}{\hbar}(H_{EM} + H_{sys})t\}. \tag{7.85}$$

Then the Hamiltonian in the interaction picture is

$$H_{int,I}^{(\theta)} = i\hbar \sum_{|\omega_0 - \omega_k| < \theta} \left(\kappa_k^* b_k^\dagger e^{i(\omega_k - \omega_0)t} c - \kappa_k b_k e^{-i(\omega_k - \omega_0)t} c^\dagger \right). \tag{7.86}$$

Here we define an operator called the *noise operator* $f(t)$ and its commutation relation which will be an important building block of the *quantum Ito algebra* in latter sections.

$$f(t) \equiv \sum_{|\omega_0 - \omega_k| < \theta} \kappa_k b_k e^{-i(\omega_k - \omega_0)t}, \tag{7.87}$$

$$\gamma(t - t') = [f(t), f^\dagger(t')] \tag{7.88}$$

$$= \sum_{|\omega_0 - \omega_k| < \theta} |\kappa_k|^2 e^{-i(\omega_k - \omega_0)(t - t')} \to \int_{\omega_0 - \theta}^{\omega_0 + \theta} d\omega g(\omega) |\kappa(\omega)|^2 e^{-i(\omega - \omega_0)(t - t')}. \tag{7.89}$$

$\kappa(\omega)$ and $g(\omega)$ in the last line of Eq. (7.89) are the average of κ_k which satisfies $\omega_k = \omega$, and the density of states, respectively.

Our next step is discussing the time evolution of wave function during a short time step Δt. Since the equation of motion for the total wave function Eq. (7.85) in the interaction picture is given by:

$$\frac{d}{dt}|\Psi_I, t\rangle = -\frac{i}{\hbar} H^{(\theta)}_{int,I}(t)|\Psi_I, t\rangle \tag{7.90}$$

$$= \left\{ f^\dagger(t)c - c^\dagger f(t) \right\} |\Psi_I, t\rangle. \tag{7.91}$$

If we expand this equation to the second order of Hamiltonian we get:

$$\begin{aligned} |\Psi_I, t\rangle = & \quad \left\{ 1 + \int_0^t dt_1 \left(f^\dagger(t_1)c - c^\dagger f(t_1) \right) \right\} |\Psi_I, t\rangle \\ + & \quad \int_0^t dt_1 \left(f^\dagger(t_1)c - c^\dagger f(t_1) \right) \int_0^{t_1} dt_2 \left(f^\dagger(t_2)c - c^\dagger f(t_2) \right) |\Psi_I, t_2\rangle. \end{aligned} \tag{7.92}$$

For further development we have to specify the initial condition of the radiation field. We assume the initial state is a vacuum $|0\rangle_{EM}$ for the time being:

$$|\Psi_I, 0\rangle = |\Psi_S, 0\rangle = |\Psi_{sys}, 0\rangle \otimes |0\rangle_{EM}, \tag{7.93}$$

though we will soon develop our discussions to the case of coherent field and finite temperature field case.

Now, we introduce two approximations. The first one is assuming that $|\Psi_I, t_2\rangle$ is sufficiently close to the initial state within a short time interval Δt and put $|\Psi_I, t_2\rangle \to |\Psi, 0\rangle$, then the Eq. (7.92) is greatly simplified as

$$\begin{aligned} |\Psi_I, \Delta t\rangle = & \quad \left(1 - c^\dagger c \int_0^{\Delta t} dt_1 \int_0^{t_1} \gamma(t_1 - t_2) \right) |\Psi, 0\rangle \\ + & \quad c \int_0^{\Delta t} dt_1 f^\dagger(t)|\Psi, 0\rangle \\ + & \quad cc \int_0^{\Delta t} dt_1 \int_0^{t_1} dt_2 f^\dagger(t_1) f^\dagger(t_2)|\Psi, 0\rangle. \end{aligned} \tag{7.94}$$

This approximation is justified when the interaction is sufficiently small, and known as the *Born approximation*. The first, second and the third line in Eq. (7.94) correspond to zero photon, one photon, and two photon generation process, respectively.

The second approximation is just eliminating the rapidly oscillating terms from the double time integral of $\gamma(t_1 - t_2)$ as follows:

$$\int_0^{\Delta t} dt_1 \int_0^{t_1} \gamma(t_1 - t_2) \simeq \left(\frac{1}{2}\Gamma + i\delta\omega \right) \Delta t, \tag{7.95}$$

where the damping constant Γ and the line-shift $\delta\omega$ is

$$\Gamma = 2\pi g(\omega_0)|\kappa(\omega_0)|^2, \tag{7.96}$$

$$\delta\omega = -P \int_{\omega_0 - \theta}^{\omega_0 + \theta} d\omega \frac{g(\omega)|\kappa(\omega)|^2}{\omega - \omega_0}. \tag{7.97}$$

This result is easily derived by using the residue theorem. $P\int$ denotes the principal value integral. This approximation is called as the *Markov approximation*. The line-shift can be the origin of the dipole force between two particles. Physically this effect is coming from the reabsorption of emitted photons by other particles, hence its strength depends on the inter-particle distance. We will discuss details in next chapter. We also have to note that the treatment of γ in the Markov approximation is equivalent to take it as:

$$\gamma(\tau) \to (\Gamma + 2i\delta\omega)\delta(\tau). \tag{7.98}$$

Quantum stochastic Schrödinger equation and zero temperature quantum Ito algebra

We can omit the two-photon generation process in Eq. (7.94) by analyzing its probability amplitude. The norms of each term in the right hand side of Eq. (7.94) are given by

$$P_0(\Delta t) = 1 - \langle cc^\dagger\rangle_0 \Gamma \Delta t \tag{7.99}$$

$$P_1(\Delta t) = \langle cc^\dagger\rangle_0 \Gamma \Delta t \tag{7.100}$$

$$P_2(\Delta t) = \frac{1}{2}\Gamma^2 \langle ccc^\dagger c^\dagger\rangle_0 \Delta t^2 \to 0 \tag{7.101}$$

to the order of Δt. After omitting the two-photon generation process, we consider the difference of wave function:

$$\begin{aligned} \Delta|\Psi,0\rangle &\equiv |\Psi,\Delta t\rangle - |\Psi,0\rangle & (7.102)\\ &= \{-(\Gamma/2 + i\delta\omega)c^\dagger c\Delta t + \sqrt{\Gamma}c\Delta B^\dagger(0)\}|\Psi,0\rangle, & (7.103)\end{aligned}$$

where the *quantum Ito increment* $\Delta B^\dagger$ is defined by:

$$\Delta B^\dagger(t) \equiv \frac{1}{\sqrt{\Gamma}}\int_t^{t+\Delta t} f(t')dt'. \tag{7.104}$$

The Eq. (7.103) can be generalized to the form:

$$\begin{aligned} \Delta|\Psi,n\Delta t\rangle &\equiv |\Psi,(n+1)\Delta t\rangle - |\Psi,n\Delta t\rangle & (7.105)\\ &= \{-(\Gamma/2 + i\delta\omega)c^\dagger c\Delta t + \sqrt{\Gamma}c\Delta B^\dagger(n\Delta t)\}|\Psi,n\Delta t\rangle. & (7.106)\end{aligned}$$

By taking weak interaction limit so that we can assume the change in each time step is sufficiently small, the *quantum stochastic Schrödinger equation*

$$d|\Psi,t\rangle = \{-(\Gamma/2 + i\delta\omega)c^\dagger c dt + \sqrt{\Gamma}c dB^\dagger(t)\}|\Psi,t\rangle \tag{7.107}$$

is derived. Then we transform Eq. (7.107) back to the Schrödinger picture by using the inverse transformations of Eq. (7.84) and Eq. (7.85):

$$d|\Psi,t\rangle = \{-\frac{i}{\hbar}H_{\rm eff}dt + \sqrt{\Gamma}c dB^\dagger(t)_{\rm Sch}\}|\Psi,t\rangle, \tag{7.108}$$

where

$$dB_{\rm Sch}(t) = e^{i\omega_0 t} dB(t), \tag{7.109}$$

$$H_{\rm eff} \equiv H_{\rm sys} + H_{\rm EM} + \hbar\delta\omega c^\dagger c - \frac{1}{2} i\hbar\Gamma c^\dagger c, \tag{7.110}$$

$$\Gamma = 2\pi g(\omega_0)|\kappa(\omega_0)|^2, \tag{7.111}$$

$$\delta\omega = -P\int_{\omega_0-\theta}^{\omega_0+\theta} d\omega \frac{g(\omega)|\kappa(\omega)|^2}{\omega-\omega_0}. \tag{7.112}$$

The derivation is simple from the commutation relation between the Hamiltonian and creation/annihilation operators.

To go one step further, we must investigate the algebra which $dB(t)$ and $\Delta B(t)$ satisfies:

$$[dB(t), dB^\dagger(s)] = 0 \tag{7.113}$$

for non-overlapping intervals $(t, t+\Delta t)$, $(s, s+\Delta s)$, and

$$dB(t)dB^\dagger(t) = dt \tag{7.114}$$

$$dB^\dagger(t)^2 = dB(t)^2 = dB(t)^\dagger dB(t) = 0 \tag{7.115}$$

$$dB(t)dt = dtdB(t) = dB^\dagger(t)dt = dtdB^\dagger(t) = dt^2 = 0 \tag{7.116}$$

These rules are called the *zero temperature quantum Ito algebra*, and will be used for fundamental techniques to develop the optical Bloch equations in the next section.

A case of coherent electromagnetic field

Here we introduce a generalization of the present theoretical framework in vacuum field to the case of coherent light field.

In the case of coherent driving field, the electromagnetic field is expressed by a product of coherent states of modes:

$$|\boldsymbol{\beta}\rangle = |1,\beta_1\rangle \otimes |2,\beta_2\rangle \otimes \cdots \otimes |k,\beta_k\rangle \otimes \cdots, \tag{7.117}$$

where $b_k|k,\beta_k\rangle = \beta_k|k,\beta_k\rangle$. Then the noise operator $f(t)$ acts on $|\beta_k\rangle$ as:

$$f(t)|k,\beta_k\rangle = \mathcal{F}(t)|k,\beta_k\rangle. \tag{7.118}$$

Here $\mathcal{F}(t)$ is a c-number defined by:

$$\mathcal{F}(t) = \sum_{|\omega_k-\omega_0|<\vartheta} \kappa_k\beta_k e^{-i(\omega_k-\omega_0)t}. \tag{7.119}$$

We modify the quantum Ito increment by using $\mathcal{F}(t)$ as follows.

$$\Delta B(t) \equiv \frac{1}{\sqrt{\Gamma}}\int_t^{t+\Delta t} \{f(t') - \mathcal{F}(t)\}dt'. \tag{7.120}$$

This quantity follows exactly same quantum Ito algebra, and the quantum stochastic Schrödinger equation is reformulated as:

$$d|\Psi,t\rangle = \{-\frac{i}{\hbar}H_{\rm eff}dt + \sqrt{\Gamma}(\mathcal{F}^*(t)c - \mathcal{F}(t)c^\dagger)dt + \sqrt{\Gamma}cdB^\dagger_{\rm Sch}(t)\}|\Psi,t\rangle. \tag{7.121}$$

The term including $\mathcal{F}$, $\mathcal{F}^*$ corresponds to the interaction with classical driving field.

The Lindblad form master equation

Now we are ready to introduce the equation of motion of density operator, the master equation. The derivation is rather simple. We are interested in the time evolution of matter system, and we therefore consider reduced density operator $\bar{\rho}$:

$$\bar{\rho}(t) \equiv {\rm Tr}_{\rm EM}\{|\Psi,t\rangle\langle\Psi,t|\}. \tag{7.122}$$

Then the time derivative of ρ is:

$$\begin{aligned} d\rho(t) &\equiv \rho(t+dt) - \rho(t) && (7.123)\\ &= \mathcal{V}(t+dt)\rho(t)\mathcal{V}(t+dt)^\dagger - \rho(t) && (7.124)\\ &= -\frac{i}{\hbar}[H_{\rm eff},\rho(t)]dt - \Gamma\left(cdB^\dagger(t) - c^\dagger dB(t)\right)\rho(t)\left(cdB^\dagger(t) - c^\dagger dB(t)\right), && (7.125)\\ d\bar{\rho}(t) &\equiv {\rm Tr}_{\rm EM}\{d\rho(t)\}, && (7.126)\end{aligned}$$

where $\boldsymbol{\rho}$ is the full density operator. By using the cyclic property of trace and the finite temperature Ito algebra, we finally get the *master equation*:

$$\frac{d\bar{\rho}(t)}{dt} = -\frac{i}{\hbar}[H_{\rm eff},\bar{\rho}(t)] + \Gamma c\bar{\rho}c^\dagger \tag{7.127}$$

Or an another notation is to separate dissipative terms from $H_{\rm eff}$ as:

$$\begin{aligned} \frac{d\bar{\rho}(t)}{dt} &= -\frac{i}{\hbar}[H_{\rm sys},\bar{\rho}(t)] - i[\delta\omega^- c^\dagger c - \delta\omega^+ cc^\dagger,\bar{\rho}] && (7.128)\\ &\quad +\frac{1}{2}\Gamma(2c\bar{\rho}c^\dagger - c^\dagger c\bar{\rho} - \bar{\rho}c^\dagger c) && (7.129)\end{aligned}$$

and this is known as the *Lindblad form master equation*.

7.2.2 The optical Bloch equation and the radiation pressure

Our task of this section is to obtain the specific form of master equation for neutral two-level system and its stationary solution. Here, the Hilbert space of matter system is spanned by two levels $\{|k\rangle,\ |l\rangle\}$. Then the operators $c,\ c^\dagger$ are replaced by the Pauli matrices, and the system Hamiltonian is given by:

$$H_{\rm sys} = \hbar\omega_{kl}|k\rangle\langle k| - \sigma^+\boldsymbol{d}_{kl}\cdot\boldsymbol{E}^{(+)}_{\rm cl}(0,t) - \sigma^-\boldsymbol{d}^*_{kl}\cdot\boldsymbol{E}^{(-)}_{\rm cl}(0,t), \tag{7.130}$$

where the driving field is

$$\boldsymbol{E}_{\rm cl}^{(+)}(0,t) = \boldsymbol{\epsilon}_{\rm cl}\mathcal{E}(t)e^{-i\omega t}. \tag{7.131}$$

Provided that the temperature of external field is zero, the master equation is:

$$\begin{aligned}\frac{d}{dt}\rho_{\rm A}(t) &= -\frac{i}{\hbar}[H_{\rm sys} + \hbar\delta\omega|k\rangle\langle k|, \rho_{\rm A}(t)] &(7.132)\\ &\quad +\frac{1}{2}\Gamma\{2\sigma^-\rho_{\rm A}(t)\sigma^+ - \sigma^+\sigma^-\rho_{\rm A}(t) - \rho_{\rm A}(t)\sigma^+\sigma^-\}. &(7.133)\end{aligned}$$

Since the external field is treated as classical, we don't need to consider how to reduce the density operator. To eliminate the time dependency of external field, we transform the density operator as follows:

$$\bar{\rho}_{\rm A} = e^{i\omega|l\rangle\langle k|}\rho_{\rm A}e^{-i\omega|l\rangle\langle k|}. \tag{7.134}$$

This is exactly the same as what we did in section 7.1.3. The resulting master equation is:

$$\begin{aligned}\frac{d\bar{\rho}_{\rm A}}{dt} &= -\frac{i}{\hbar}[\bar{H}_{\rm eff}, \bar{\rho}_{\rm A}] + \mathcal{J}\bar{\rho}_{\rm A}, &(7.135)\\ \bar{H}_{\rm eff} &= \hbar(-\Delta - i\frac{1}{2}\Gamma)|k\rangle\langle k| - \frac{1}{2}\hbar\Omega_{\rm R}(t)^*\sigma^- + \frac{1}{2}\hbar\Omega_{\rm R}(t)\sigma^+, &(7.136)\\ \Delta &\equiv \omega - \omega_{kl} - \delta\omega, &(7.137)\\ \Omega_{\rm R}(t) &\equiv \frac{2\boldsymbol{d}_{kl}\cdot\boldsymbol{\epsilon}\mathcal{E}(t)}{\hbar}, &(7.138)\\ \mathcal{J}\bar{\rho}_{\rm A} &\equiv \Gamma\sigma^-\bar{\rho}_A(t)\sigma^+ \equiv \Gamma\bar{\rho}_{kk}|l\rangle\langle l| &(7.139)\end{aligned}$$

This is the well known *optical Bloch equation*. The significant difference contrast with the results of section 7.1.3 is the presence of damping and line shift, and they make difficulties to analyze time dependent solutions using the idea that the Bloch sphere rotating in Bloch sphere. The stationary solution is easy to derive, however. Explicitly writing down the components of $\bar{\rho}_{\rm A}$, the optical Bloch equation Eq. (7.136) can be expressed like:

$$\frac{d}{dt}\begin{pmatrix}\bar{\rho}_{{\rm A},kl}\\ \bar{\rho}_{{\rm A},lk}\\ \bar{\rho}_{{\rm A},kk}\\ \bar{\rho}_{{\rm A},ll}\end{pmatrix} = \begin{pmatrix} i\Delta-\Gamma/2 & 0 & -i\Omega_{\rm R}/2 & i\Omega_{\rm R}/2\\ 0 & -i\Delta-\Gamma/2 & i\Omega_{\rm R}/2^* & -i\Omega_{\rm R}/2\\ -i\Omega_{\rm R}/2^* & i\Omega_{\rm R}/2 & -\Gamma & 0\\ i\Omega_{\rm R}/2^* & -i\Omega_{\rm R}/2 & \Gamma & 0\end{pmatrix}\begin{pmatrix}\bar{\rho}_{{\rm A},kl}\\ \bar{\rho}_{{\rm A},lk}\\ \bar{\rho}_{{\rm A},kk}\\ \bar{\rho}_{{\rm A},ll}\end{pmatrix}. \tag{7.140}$$

The stationary solution can be obtained by solving a linear equation, *i.e.* the RHS = $\mathbf{0}$. The given solutions are as follows:

$$\begin{aligned}\bar{\rho}_{{\rm A},ll} &= \rho_{{\rm A},ll} = \frac{|\Omega_{\rm R}|^2/4}{\Delta^2 + \Gamma/4 + |\Omega_{\rm R}|^2/2}, &(7.141)\\ \bar{\rho}_{{\rm A},kk} &= \rho_{{\rm A},kk} = 1 - \bar{\rho}_{{\rm A},ll} = \frac{\Delta^2 + \Gamma/4 + |\Omega_{\rm R}|^2/4}{\Delta^2 + \Gamma/4 + |\Omega_{\rm R}|^2/2}, &(7.142)\\ \rho_{{\rm A},lk} &= \bar{\rho}_{{\rm A},lk}e^{-i\omega t} = -\frac{\Omega_{\rm R}(\Delta + i\Gamma/2)}{\Delta^2 + \Gamma/4 + |\Omega_{\rm R}|^2/2}e^{-i\omega t}. &(7.143)\end{aligned}$$

We can see some important features in these results like *saturation* of diagonal terms : $\rho_{\mathrm{A},kk},\ \rho_{\mathrm{A},ll} \to 1/2$, when Ω_{R} is huge. The non-diagonal elements are related to the expectation value of the electric polarization $\langle \boldsymbol{d}(t) \rangle$, since it is defined by:

$$\langle \boldsymbol{d}(t) \rangle = \mathrm{Tr}\{\boldsymbol{d}\rho_{\mathrm{A}}(t)\} = \boldsymbol{d}_{lk}\rho_{\mathrm{A},lk} + \boldsymbol{d}_{kl}\rho_{\mathrm{A},kl}. \tag{7.144}$$

The electric polarization of non-interacting n-atom system is then given by:

$$\boldsymbol{P} \equiv n\langle \boldsymbol{d}(t) \rangle. \tag{7.145}$$

Approximate treatment of the radiation pressure

Here we introduce a phenomenological way to include the heating process due to recoil effect. Theoretical formalism of this section and the next section 7.3 is based on the methodology of [41]. When the excitation by driving field and decay are balanced, emission of a photon per unit time is given by:

$$P = \rho_{\mathrm{A},kk}\Gamma. \tag{7.146}$$

Then the momentum transfer which accompanies the photon emission is:

$$\boldsymbol{F} = \hbar \boldsymbol{Q} P, \tag{7.147}$$

where $\boldsymbol{Q}$ is the wave vector of photon, and the kinetic energy change before and after the emission is:

$$\Delta E = \frac{\hbar^2(\boldsymbol{Q}+\boldsymbol{q})^2}{2m^*} - \frac{\hbar^2 q^2}{2m^*}, \tag{7.148}$$

where $\hbar\boldsymbol{q}$ is the initial momentum of particle, and m^* is its (effective) mass. ΔE will be a key quantity as a possible criterion to discuss the balance of energy when the system is coupled to both photon and phonon. By considering a fact that mostly $\boldsymbol{q} = 0$ excitons are generated by optical excitation processes, we can approximately put the ΔE as:

$$\Delta E \simeq \frac{\hbar^2 \boldsymbol{Q}^2}{2m^*} \tag{7.149}$$

Then the kinetic energy income per unit time R_{photon} is roughly given by:

$$R_{photon} \simeq \frac{\hbar^2 \boldsymbol{Q}^2}{2m^*}\rho_{\mathrm{A},kk}\Gamma. \tag{7.150}$$

An analytical form of the damping factor Γ must be given here. As we saw in the last section the Γ is given by a product of the density of states $g(\omega)$ and the light-matter coupling $\kappa(\omega)$ as $\Gamma = 2\pi g(\omega_0)|\kappa(\omega)|^2$. We have to note that the angler dependency and polarization dependency are omitted in this form. When those degrees of freedom are included, the damping factor Γ is modified by

$$\Gamma = \sum_{\lambda=1,2} \int d\Omega 2\pi g(\omega_0)|\kappa^{(\lambda)}(\omega_0)|^2 \tag{7.151}$$

where

$$g(\omega) = \frac{V}{2\pi c^3}\omega^2 \tag{7.152}$$

$$|\kappa^{(\lambda)}(\omega)|^2 = \frac{\omega}{2\hbar\epsilon_0 V}|\boldsymbol{d}_{kl}\cdot\boldsymbol{e}^{(\lambda)}|^2. \tag{7.153}$$

Here Ω is the solid angle, c is the speed of light in vacuum, ϵ_0 is the dielectric constant in vacuum, and V is the volume of the system.

7.3 Cooling by the lattice system

In this section we introduce a theoretical framework to discuss the cooling process by emitting phonons based on the methodology of [41]. In the last section we showed that the spontaneous photo-emission from excited states leads to the heating of the system. In the case of condensed matter system, there is a lattice system. There is a process that the heated excitons can lose their kinetic energy by emitting acoustic phonons. We consider the time evolution of excitonic states during short time period. To restrict our discussion within one-phonon creation process, we perturbatively expand the wave function by the first order of V_{phonon}, the electron-phonon interaction potential. Then we get:

$$|\Psi,t\rangle = U(t)|\Psi,0\rangle - \frac{i}{\hbar}\int_0^t dt_1 U(t-t_1)V_{phonon}U(t_1)|\Psi,0\rangle, \tag{7.154}$$

where $U(t)=\exp\{iH_0t/\hbar\}$ and H_0 is a Hamiltonian of excitonic system.

On the other hand, it would be reasonable to assume that the phonon heat bath is still thermal equilibrium after the one-phonon absorption and/or emission process from an exciton. Then we can express $|\Psi,t\rangle$ as:

$$|\Psi,t\rangle = c_0(t)|\Psi,0\rangle + \sum_q\{c_{+q}(t)|T,+q\rangle + c_{-q}(t)|T,-q\rangle\}, \tag{7.155}$$

where

$$|\Psi,0\rangle = |S,\boldsymbol{k}\rangle\otimes|T\rangle \tag{7.156}$$

$$|T,+\boldsymbol{q}\rangle = \frac{1}{\sqrt{n_q+1}}|S,\boldsymbol{k}-\boldsymbol{q}\rangle\otimes b_q^\dagger|T\rangle \tag{7.157}$$

$$|T,-\boldsymbol{q}\rangle = \frac{1}{\sqrt{n_q}}|S,\boldsymbol{k}+\boldsymbol{q}\rangle\otimes b_q|T\rangle. \tag{7.158}$$

Here T is the temperature of lattice system and n_q is the Bose-Einstein distribution. S, $\boldsymbol{k}$, and $\boldsymbol{q}$ are an index of inner degree of freedom of exciton, a center-of-mass momentum of exciton, and a wave vector of an emitted or absorbed phonon, respectively. Of course these amplitude must satisfy the conservation of norm as:

$$|c_0(t)|^2 + \sum_q\{|c_{+q}(t)|^2 + |c_{-q}(t)|^2\} = 1. \tag{7.159}$$

By multiplying $\langle T, +\boldsymbol{q}|$, $\langle T, -\boldsymbol{q}|$ from left hand side, these amplitude can be relatively easily calculated. The results are as follows:

$$|c_{+q}(t)|^2 \simeq \frac{2\pi}{\hbar}(\bar{n}_q + 1)|G_{k-q,k}|^2\delta\{E_i - E_f - \hbar\omega_q\}t, \tag{7.160}$$

$$|c_{-q}(t)|^2 \simeq \frac{2\pi}{\hbar}\bar{n}_q|G_{k-q,k}|^2\delta\{E_i - E_f + \hbar\omega_q\}t. \tag{7.161}$$

Here $G_{k-q,k}$ is a coupling constant between two excitonic states with wave vector $\boldsymbol{k}-\boldsymbol{q}$ and $\boldsymbol{k}$, respectively. Explicit form is given in appendix A.1.2. Then the energy change during the time range $[0,\ t]$ is given by

$$\Delta E_k(t) = \sum_q\{-\hbar\omega_q|c_{+q}(t)|^2 + \hbar\omega_q|c_{-q}(t)|^2\} \tag{7.162}$$

$$= \frac{2\pi}{\hbar}\sum_q\{-\hbar\omega_q(\bar{n}_q+1)|G_{k-q,k}|^2\delta\{E_i - E_f - \hbar\omega_q\} \tag{7.163}$$

$$+\hbar\omega_q\bar{n}_q|G_{k+q,k}|^2\delta\{E_i - E_f + \hbar\omega_q\}\}t \tag{7.164}$$

$$= R_{ph}(T)t. \tag{7.165}$$

When

$$R_{photon} = R_{ph}(T^*) \tag{7.166}$$

T^* provides a simple estimation of the temperature where the heating process balances with the cooling process.

7.4 First principles methods for calculating excitonic states in solids

7.4.1 Density functional theory

The density functional theory (DFT) have been reigning as the most standard method to simulate the ground state properties of condensed matter systems. The correctness of the DFT is based on the Hohenberg-Kohn theorem [56] which ensures that there is one-to-one correspondence between external field and the density distribution of an electronic system in which electrons are mutually interacting under the external field. The theorem also ensures that, in particular, the total energy of the system can be expressed as a functional of the electron density distribution of the ground state though its exact form have been unknown.

In practical calculation we solve the self-consistent Kohn-Sham equation for one-particle orbital $\phi^{\mathrm{DFT}}_{n\boldsymbol{k}}$, as

$$\{-\frac{\hbar^2}{m}\nabla^2 + V_{\mathrm{ion}} + V_{\mathrm{H}} + V^{\mathrm{DFT}}_{\mathrm{xc}}\}\phi^{\mathrm{DFT}}_{n\boldsymbol{k}} = E^{\mathrm{DFT}}_{n\boldsymbol{k}}\phi^{\mathrm{DFT}}_{n\boldsymbol{k}}. \tag{7.167}$$

V_{ion} and V_{H} are the electron-ion interaction term and the direct electron-electron Coulomb interaction term, respectively. Here the exchange-correlation potential $V^{\mathrm{DFT}}_{\mathrm{xc}}$ is defined by a functional derivative of the exchange-correlation energy E_{xc} with respect to the density $n(\boldsymbol{r})$ as

$$V^{\mathrm{DFT}}_{\mathrm{xc}} \equiv \frac{\delta E_{xc}}{\delta n(\boldsymbol{r})}. \tag{7.168}$$

In this thesis we utilize a widely used approximation

$$E_{xc} = \int d\boldsymbol{r} n(\boldsymbol{r}) \epsilon_{xc}(\boldsymbol{r}) \tag{7.169}$$

called *local density approximation (LDA)* [57]. The analytical form of $\epsilon_{xc}(\boldsymbol{r})$ is obtained from the Monte Carlo calculation of uniform electron gas system.

7.4.2 GW approximation

The density functional theory achieved great success. Nevertheless it still has a problem of systematic underestimation of the band gap of materials. The GW approximation is a many-body perturbation theory classified to a kind of Green's function method and being well known for its ability to considerably improve this situation. In the theory of GW approximation one particle orbit is determined by a Dyson equation where the self energy Σ is approximated by a product of Green's function G and the screened Coulomb interaction W as $\Sigma = i\hbar GW$ as follows:

$$\{-\frac{\hbar^2}{2m}\nabla^2 + V_{\text{ion}} + V_{\text{H}} + \Sigma(E^{\text{GW}}_{n\boldsymbol{k}})\}\psi^{\text{GW}}_{n\boldsymbol{k}} = E^{\text{GW}}_{n\boldsymbol{k}}\psi^{\text{GW}}_{n\boldsymbol{k}}. \tag{7.170}$$

The expression of self energy in GW approximation is truncated by the first order of W. Actually it is, in principle, possible to expand the self energy by arbitrary order of W by following a group of equations called *Hedin's equation*. The Hedin's equation expresses the mutual relation between self energy Σ, polarization P, screened Coulomb interaction W, and so called vertex function Γ as follows:

$$\text{Self energy } : \Sigma(\mathbf{1},\mathbf{2}) = i\hbar \int W(\mathbf{1}^+,\mathbf{3})G(\mathbf{1},\mathbf{4})\Gamma(\mathbf{4},\mathbf{2};\mathbf{3})d\mathbf{34} \tag{7.171}$$

$$\text{Polarization } : P(\mathbf{1},\mathbf{2}) = -i\hbar \int G(\mathbf{2},\mathbf{3})G(\mathbf{4},\mathbf{2}^+)\Gamma(3,4;1)d\mathbf{34} \tag{7.172}$$

$$\text{Screened Coulomb } : W(\mathbf{1},\mathbf{2}) = v(\mathbf{1},\mathbf{2}) + \int W(\mathbf{1},\mathbf{3})P(\mathbf{3},\mathbf{4})v(\mathbf{4},\mathbf{2})d\mathbf{34} \tag{7.173}$$

$$\text{Vertex Function } : \Gamma(\mathbf{1},\mathbf{2};\mathbf{3}) = \delta(\mathbf{1},\mathbf{2})\delta(\mathbf{1},\mathbf{3}) + \frac{\delta\Sigma(\mathbf{1},\mathbf{2})}{\delta V(\mathbf{3})}. \tag{7.174}$$

Here we used a compressed notation *e.g.* $\mathbf{1} = (\boldsymbol{x}_1, s_1, t_1)$, where $\boldsymbol{x}_1$, s_1, and t_1 are the spatial coordinate, spin and time of a particle, respectively. Higher order terms of Γ are given by functional derivative of Σ by the Hartree term V. When the expansion is truncated by $\Gamma \simeq \delta(\mathbf{1},\mathbf{2})\delta(\mathbf{1},\mathbf{3})$, the GW approximation is given.

For carrying out the GW+BSE calculation we utilized a program package *BerkeleyGW* [23]. The BerkeleyGW package is composed of several calculation steps, namely the calculation of i). inverse dielectric matrix ϵ^{-1}, ii). GW self energy correction, iii). electron-hole interaction kernel, and iv). diagonalization of the Bethe-Salpeter equation. We have to note that "the BerkeleyGW does not update the wave function, hence the other quantities being built from the Green's function". In other words, the Dyson equation (7.170) must be solved self-consistently, but the BerkeleyGW doesn't do that. It is because the variation of wave function after self-consistent calculation is known to be sufficiently small [20]. Sometimes this method of shortcutting is called G_0W_0 or one-shot GW. Thus the BerkeleyGW receives the wave function given

by pre-calculation of Quantum-ESPRESSO as an input and it remains to be the wave function of quasi-particle. In the followings we briefly show more detailed theoretical framework we used to compute when using BerkeleyGW.

Static dielectric matrix approximation

The first central quantity we have to compute is the screened Coulomb interaction W, and to construct W we need to prepare the dielectric matrix ϵ. Hereafter we use the Fourier transformed form for $W(\mathbf{1},\mathbf{2})$:

$$W(\boldsymbol{x},\boldsymbol{x}',E) = \int W(\boldsymbol{x},t;\boldsymbol{x}',t')e^{-iE(t-t')/\hbar}d(t-t') \tag{7.175}$$

$$= \sum_{\boldsymbol{q},\boldsymbol{G},\boldsymbol{G}'} e^{i(\boldsymbol{q}+\boldsymbol{G})\cdot\boldsymbol{r}}W_{\boldsymbol{G}\boldsymbol{G}'}(\boldsymbol{q},\omega)e^{-i(\boldsymbol{q}+\boldsymbol{G}')\cdot\boldsymbol{r}}, \tag{7.176}$$

and also for relevant quantities. Here $\boldsymbol{G}$, $\boldsymbol{G}'$ are reciprocal lattice vectors and $\boldsymbol{q}$ is a wave vector in the first Brillouin zone. $W_{\boldsymbol{G}\boldsymbol{G}'}(\boldsymbol{q},\omega)$ and the bare Coulomb interaction $v(\boldsymbol{q}+\boldsymbol{G}) = 4\pi/|\boldsymbol{q}+\boldsymbol{G}|^2$, polarization $P_{\boldsymbol{G}\boldsymbol{G}'}(\boldsymbol{q},\omega)$ are mutually connected via dielectric matrix $\epsilon_{\boldsymbol{G}\boldsymbol{G}'}(\boldsymbol{q},\omega)$ as follows:

$$W_{\boldsymbol{G}\boldsymbol{G}'}(\boldsymbol{q},\omega) = \epsilon_{\boldsymbol{G}\boldsymbol{G}'}(\boldsymbol{q},\omega)^{-1}v(\boldsymbol{q}+\boldsymbol{G}) \tag{7.177}$$

$$\epsilon_{\boldsymbol{G}\boldsymbol{G}'}(\boldsymbol{q},\omega) = \delta_{\boldsymbol{G},\boldsymbol{G}'} - v(\boldsymbol{q}+\boldsymbol{G})P_{\boldsymbol{G}\boldsymbol{G}'}(\boldsymbol{q},\omega). \tag{7.178}$$

Thus the W has a energy or frequency dependency. For numerical cost of evaluating full dynamical dielectric constant $\epsilon_{\boldsymbol{G}\boldsymbol{G}'}(\boldsymbol{q},\omega)$ we use the static dielectric matrix which omits the frequency dependency of polarizability as follows:

$$P_{\boldsymbol{G}\boldsymbol{G}'}(\boldsymbol{q},\omega=0) = \sum_{n}^{\text{occupied}}\sum_{n'}^{\text{empty}}\sum_{\boldsymbol{k}} M_{nn'}(\boldsymbol{k},\boldsymbol{q},\boldsymbol{G})M^*_{nn'}(\boldsymbol{k},\boldsymbol{q},\boldsymbol{G}')\frac{1}{E_{n\boldsymbol{k}+\boldsymbol{q}}-E_{n'\boldsymbol{k}+\boldsymbol{q}}} \tag{7.179}$$

$$\epsilon_{\boldsymbol{G}\boldsymbol{G}'}(\boldsymbol{q},0) = \delta_{\boldsymbol{G},\boldsymbol{G}'} - v(\boldsymbol{q}+\boldsymbol{G})P_{\boldsymbol{G}\boldsymbol{G}'}(\boldsymbol{q},0). \tag{7.180}$$

Here $E_{n\boldsymbol{k}+\boldsymbol{q}}$ is one-particle energy given by DFT calculation. Then W become independent of frequency as $W_{\boldsymbol{G}\boldsymbol{G}'}(\boldsymbol{q},0) = \epsilon_{\boldsymbol{G}\boldsymbol{G}'}(\boldsymbol{q},0)^{-1}v(\boldsymbol{q}+\boldsymbol{G})$.

Self energy with Hybertsen-Louie generalized plasmon pole (HL-GPP) model

Although the static dielectric matrix is frequency independent, dynamical property of self energy is include by using the Hybertsen-Louie generalized plasmon pole model in BerkeleyGW. In the GW approximation the self energy Σ is decomposed into two part: $\Sigma = \Sigma_{\mathrm{SX}} + \Sigma_{CH}$. The first term is called the screened-exchange operator, and the second is the Coulomb hole

operator. Matrix elements of each operators are given by:

$$\begin{aligned}\langle n\boldsymbol{k}|\Sigma_{\rm SX}|n'\boldsymbol{k}\rangle &= -\sum_{n''}^{\rm occupied}\sum_{\boldsymbol{qGG'}} M^*_{n''n}(\boldsymbol{k},-\boldsymbol{q},-\boldsymbol{G})M_{n''n'}(\boldsymbol{k},-\boldsymbol{q},\boldsymbol{G'}) \\ &\times \left\{\delta_{\boldsymbol{GG'}}+\frac{\Omega^2_{\boldsymbol{GG'}}(\boldsymbol{q})(1-i\tan\phi_{\boldsymbol{GG'}}(\boldsymbol{q}))}{(E-E_{n''\boldsymbol{k}-\boldsymbol{q}})^2-\tilde{\omega}^2_{\boldsymbol{GG'}}(\boldsymbol{q})}\right\} v(\boldsymbol{q}+\boldsymbol{G}), \qquad (7.181)\\ \langle n\boldsymbol{k}|\Sigma_{\rm CH}|n'\boldsymbol{k}\rangle &= \frac{1}{2}\sum_{n''}^{\rm occupied}\sum_{\boldsymbol{qGG'}} M^*_{n''n}(\boldsymbol{k},-\boldsymbol{q},-\boldsymbol{G})M_{n''n'}(\boldsymbol{k},-\boldsymbol{q},\boldsymbol{G'}) \\ &\times \frac{\Omega^2_{\boldsymbol{GG'}}(\boldsymbol{q})(1-i\tan\phi_{\boldsymbol{GG'}}(\boldsymbol{q}))}{\tilde{\omega}_{\boldsymbol{GG'}}(\boldsymbol{q})(E-E_{n''\boldsymbol{k}-\boldsymbol{q}}-\tilde{\omega}_{\boldsymbol{GG'}}(\boldsymbol{q}))} v(\boldsymbol{q}+\boldsymbol{G}), \qquad (7.182)\end{aligned}$$

in HL-GPP model [23]. Here $\Omega_{\boldsymbol{GG'}}$ and $\tilde{\omega}_{\boldsymbol{GG'}}$ are called the effective bare plasma frequency and the GPP mode frequency defined as:

$$\Omega^2_{\boldsymbol{GG'}} = \omega_p^2\frac{(\boldsymbol{q}+\boldsymbol{G})(\boldsymbol{q}+\boldsymbol{G'})\rho(\boldsymbol{G}-\boldsymbol{G'})}{|\boldsymbol{q}+\boldsymbol{G}|^2\rho(\boldsymbol{0})} \qquad (7.183)$$

$$\tilde{\omega}^2_{\boldsymbol{GG'}} = \frac{|\lambda_{\boldsymbol{GG'}}(\boldsymbol{q})|}{\cos\phi_{\boldsymbol{GG'}}(\boldsymbol{q})}, \qquad (7.184)$$

$$|\lambda_{\boldsymbol{GG'}}(\boldsymbol{q})|e^{i\phi_{\boldsymbol{GG'}}(\boldsymbol{q})} = \frac{\Omega^2_{\boldsymbol{GG'}}}{\delta_{\boldsymbol{GG'}}-\epsilon^{-1}_{\boldsymbol{GG'}}(\boldsymbol{q};0)}. \qquad (7.185)$$

Thus the energy dependency of the self energy can be included using the HL-GPP model and there is no adjustable parameter, although the static dielectric matrix has no dependency on frequency.

Now we are ready to evaluate the GW energy correction. The GW Hamiltonian on the left hand side of Eq. (7.170). The matrix element is given by:

$$\langle n\boldsymbol{k}|(-\frac{\hbar^2}{2m}\nabla^2+V_{\rm ion}+V_{\rm H}+\Sigma(E))|m\boldsymbol{k}\rangle = E^{\rm DFT}_{n\boldsymbol{k}}\delta_{nm}+\langle n\boldsymbol{k}|\Sigma(E)-\Sigma^{\rm DFT}(E)|m\boldsymbol{k}\rangle \qquad (7.186)$$

As an empirical fact the DFT wave function is sufficiently close to the GW wave function [20], we therefore only consider diagonal elements:

$$E^{\rm GW}_{n\boldsymbol{k}} = E^{\rm DFT}_{n\boldsymbol{k}}+\langle n\boldsymbol{k}|\Sigma(E)-\Sigma^{\rm DFT}(E)|n\boldsymbol{k}\rangle \qquad (7.187)$$

When we use the LDA functional for DFT calculation, $\Sigma^{\rm DFT}$ is independent of the energy. To compute the Eq. (7.187) the first step is to set $\Sigma(E)=\Sigma(E^{\rm DFT})$, and then we get first estimation of one-particle energy $E^1_{n\boldsymbol{k}}$ by

$$E^1_{n\boldsymbol{k}} = E^{\rm DFT}_{n\boldsymbol{k}}+\langle n\boldsymbol{k}|\{\Sigma(E^{\rm DFT}_{n\boldsymbol{k}})-\Sigma^{\rm DFT}\}|n\boldsymbol{k}\rangle. \qquad (7.188)$$

One may reach self-consistency by repeating this process. Fortunately in many system $\Sigma(E)$ is known to be a linear function of E. The BerkeleyGW takes advantage of this feature and avoids frequent reevaluation of self energy using Newton's method as:

$$\begin{aligned}E^{\rm GW}_{n\boldsymbol{k}} &= E^1_{n\boldsymbol{k}}+(E_{n\boldsymbol{k}}-E^{\rm DFT}_{n\boldsymbol{k}})Z, \qquad (7.189)\\ Z &= \frac{\Delta\Sigma_{n\boldsymbol{k}}(E^{\rm DFT}_{n\boldsymbol{k}})/\Delta E}{1-\Delta\Sigma_{n\boldsymbol{k}}(E^{\rm DFT}_{n\boldsymbol{k}})/\Delta E}, \qquad (7.190)\end{aligned}$$

where Z is called the quasi particle renormalization factor. Thus the one-particle energy can be repeatedly improved until the self-consistency is achieved.

Bethe-Salpeter equation

Our next task is to introduce a way to describe electron-hole pair excitation states by a first principles method. Here, we discuss the derivation based on Refs. [21]. The starting point is the Dyson equation for two-particle correlation function $L(1,2;1',2')$:

$$L(1,2;1',2') = L_0(1,2;1',2') + \int d(3456) L_0(1,4;1',3) K(3,5;4,6) L(6,2;5,2'). \tag{7.191}$$

The definition of $L(1,2;1',2')$ is:

$$L(1,2;1',2') \equiv -G_2(1,2;1',2') + G_1(1,2)G_1(1',2') \tag{7.192}$$

where G_2 is the two-particle Green's function. $K(3,5;4,6)$ is the interaction kernel which is defined by:

$$K(3,5;4,6) = -i\hbar\delta(34)\delta(56)v(3,6) + \frac{\delta\Sigma(3,4)}{\delta G_1(6,5)}. \tag{7.193}$$

By considering the time translational symmetry we can define $L(1,2;1',2';\omega)$, the Fourier transformed form of $L(1,2;1',2')$. In this case, 1, 2, 1′, 2′ do not contain time variables anymore. $L(1,2;1',2';\omega)$ can be written by:

$$L(1,2;1',2';\omega) = i\sum_s \left\{ \frac{\chi_s(x_1,x_{1'})\chi_s^*(x_2,x_{2'})}{\omega-\Omega_s} - \frac{\chi_s^*(x_1,x_{1'})\chi_s(x_2,x_{2'})}{\omega+\Omega_s} \right\}, \tag{7.194}$$

where χ_s is the electron-hole pair amplitude:

$$\chi_s(x,x') = -\langle N,0|\psi^\dagger(x)\psi(x)|N,s\rangle. \tag{7.195}$$

Our approach is to expand χ_s using the one-particle orbit $\psi_i(x)$ as:

$$\chi_s(x,x') = \sum_i^{\text{occupied}} \sum_j^{\text{empty}} \{A_{ij}^s \psi_i(x)\psi_j^*(x') + B_{ij}^s \psi_i^*(x')\psi_j(x)\}. \tag{7.196}$$

Here we abbreviated a sum over wave vector. By using those expression of $L(1,2;1',2')$, Eq. (7.191) turns into a couple of eigenvalue equations:

$$(E_c - E_v)A_{cv}^s + \sum_{c'v'} K_{cv,c'v'}^{AA}(\Omega_s)A_{c'v'}^s + \sum_{c'v'} K_{cv,c'v'}^{AB}(\Omega_s)B_{c'v'}^s = \Omega_s A_{cv}^s \tag{7.197}$$

$$(E_c - E_v)B_{cv}^s + \sum_{c'v'} K_{cv,c'v'}^{BB}(\Omega_s)B_{c'v'}^s + \sum_{c'v'} K_{cv,c'v'}^{BA}(\Omega_s)A_{c'v'}^s = -\Omega_s B_{cv}^s. \tag{7.198}$$

The coupling term $K^{AA(BB)}$ and $K^{AB(BA)}$ are given by:

$$K_{cv,c'v'}^{AA}(\Omega_s) = i\int d(3456)\phi_v(x_4)\phi_c^*(x_3)K(35,46;\Omega_s)\phi_{v'}^*(x_5)\phi_{c'}(x_6) \tag{7.199}$$

$$K_{cv,c'v'}^{AB}(\Omega_s) = i\int d(3456)\phi_v(x_4)\phi_c^*(x_3)K(35,46;\Omega_s)\phi_{v'}^*(x_6)\phi_{c'}(x_5). \tag{7.200}$$

A^s and B^s are coupled by off-diagonal term $K^{AB(BA)}$. It was found that the contribution of off-diagonal term in excitation energies is negligibly small in some systems, though several

quantities such as macroscopic dielectric possibly be affected [21]. In BerkeleyGW K^{AB} and K^{BA} are set to be zero, and only the eigenvalue equation of A^s is considered:

$$(E^{GW}_{c\boldsymbol{k}} - E^{\mathrm{GW}}_{v\boldsymbol{k}})A^S_{vc\boldsymbol{k}} + \sum_{v'c'\boldsymbol{k}} \langle vc\boldsymbol{k}|K^{eh}|v'c'\boldsymbol{k}'\rangle A^S_{v'c'\boldsymbol{k}'} = \Omega_S A^S_{vc\boldsymbol{k}}. \tag{7.201}$$

The interaction kernel K^{eh} is decomposed into a sum of screened Coulomb K^d and direct exchange K^x as $K^{eh} = K^d + K^x$, and K^d, K^x are given by:

$$\langle vc\boldsymbol{k}|K^d|v'c'\boldsymbol{k}'\rangle = -\sum_{\boldsymbol{GG'}} M_{cc'}(\boldsymbol{k},\boldsymbol{q},\boldsymbol{G})W_{\boldsymbol{GG'}}(\boldsymbol{q};0)M^*_{vv'}(\boldsymbol{k},\boldsymbol{q},\boldsymbol{G'}) \tag{7.202}$$

$$\langle vc\boldsymbol{k}|K^x|v'c'\boldsymbol{k}'\rangle = \sum_{\boldsymbol{GG'}} M_{cv}(\boldsymbol{k},\boldsymbol{q},\boldsymbol{G})v(\boldsymbol{q}+\boldsymbol{G})M^*_{c'v'}(\boldsymbol{k},\boldsymbol{q},\boldsymbol{G'}) \tag{7.203}$$

in $\boldsymbol{G}$ space expression. By diagonalizing Eq. (7.201) we can obtain excitonic spectrum Ω_s and the exciton wave function A^s_{vc}.

8. RESULTS AND DISCUSSIONS

8.1 Electronic and excitonic states of graphane

In this section we introduce the results for graphane, the hydrogenated graphene. The crystal structure of graphane is a 2D-like monolayer and several metastable structures have been reported such as *chair*-type, *boat*-type, *stirrup*-type [44]. The *chair*-type structure has been reported as the most stable structure among them by almost 100 meV per unit cell [44]. The unit cell has a hexagonal symmetry and the crystal structure is invariant under the space group operations which form a group being isomorphic to the D_{3d} point group. The analytical expressions of operations and a list of the representations are summarized in Appendix B. The *chair*-type structure of graphane is shown in Figure 8.1.

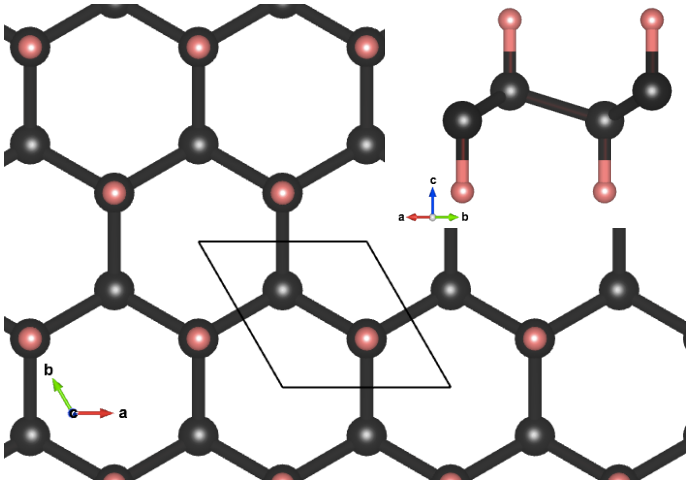

Figure 8.1: The crystal structure of graphane. The black balls indicate carbon atoms and the pink balls indicate hydrogen atoms.

To examine the feasibility of optical lattice for exciton, the graphane is a good candidates from several reasons.

1. The exciton binding energy E_{ex} has been reported to be quite large ($E_{\text{ex}} \sim 1.5$ eV). It makes easier to identify excitonic energy levels by experiments.

2. The electronic band structure is simple. The band gap opens at Γ-point and there is only double degeneracy of valence band maximum. It will benefit the interpretation of results and comparison with other compounds.

3. No experimental confinement technique for excitons has been realized in two-dimensional materials.

Actually there is a way to confine exciton motion in bulk system by inducing local uniaxial strain on the crystal. The high pressure slightly reduce the band gap and it works confinement potential [29]. This method, however, would be hard to apply to two-dimensional system. It is well known that the electronic structure of atomically thin two-dimensional systems is sensitive to the screening of Coulomb interaction by surroundings. Thus, this work may provide a hopeful experimental technique for manipulating excitonic states. In this section we show the electronic band structure of graphane by DFT calculation in 8.1.1, the excitonic energy spectrum in 8.1.2 and the matrix elements of exciton-exciton transition dipole moment in 8.2.1.

8.1.1 Electronic structure of graphane

We implemented the *ab initio* electronic state calculation based on the density functional theory using the local density approximation for the exchange-correlation potential and the norm-conserving pseudo potential for ionic potentials of carbon and hydrogen atoms. This calculation was done by using *Quantum-ESPRESSO* package [22]. In table 8.1 detailed structure parameters are shown. This structure was obtained by a structure relaxation calculation with wave function energy cutoff 150Ry and $8 \times 8 \times 1$ k points. The interlayer distance was fixed to be 15Å. The bond length of C-C and C-H bonding are in good agreement with the results of

Wave function energy cutoff	150Ry		
Lattice constant a [Å]	2.557		
Inter layer distance	15 Å		
Atomic position [a]	x	y	z
C1	1/2	$\sqrt{3}/6$	-9.03×10^{-2}
C2	0	$\sqrt{3}/3$	9.03×10^{-2}
H1	1/2	$\sqrt{3}/6$	-0.523
H2	0	$\sqrt{3}/3$	0.523
Bond length [Å]			
C-C	1.547		
C-H	1.105		

Table 8.1: Structure parameters of graphane given by our structure relaxation calculation. Note that the atomic positions are in units of the lattice constant a.

density functional calculations (C-C is 1.54 $\mathring{A}$ and C-H is 1.10 $\mathring{A}$ by using PBE functional) [44]. In figure 8.2 we show the calculated electronic band structure of graphane. The band structure clearly shows a direct band gap opens at Γ point and the gap width was 3.60eV. The valence band maximum is doubly degenerate and it has been predicted to belong to E_g representation of D_{3d} group [58]. We also show a calculated phonon band structure in figure 8.3. Our calculation well reproduced the results of previous studies [44, 58].

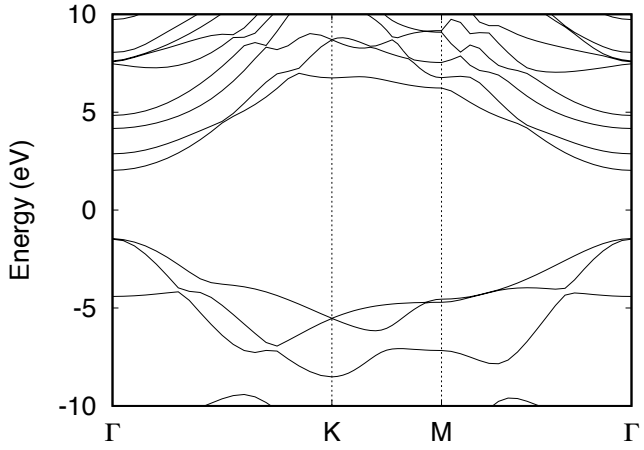

Figure 8.2: The electronic band structure of graphane calculated by doing DFT calculation using local density approximation.

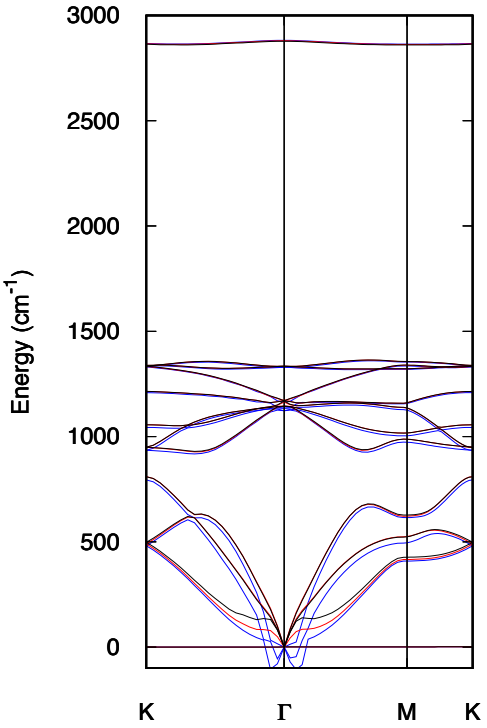

Figure 8.3: The phonon band structure of graphane calculated by using the density functional perturbation theory for three energy cutoff values (blue line : 130Ry, red line : 140Ry, black line : 150Ry).

8.1.2 Energy spectrum of exciton

In this work the excitonic states are numerically simulated by using the GW+BSE method. We used the *BerkeleyGW* program package [23]. In this subsection we introduce the calculated GW quasi particle energy and the excitonic spectrum given by solving the Bethe-Salpeter equation. In table 8.2 we summarize the calculation condition. Total computational time of DFT and GW+BSE calculation was about 23 hour with this condition. The number of CPU used for parallel computation is 72 nodes $\times$ 24 CPUs = 1724 CPUs, at maximum. Convergence of

Dielectric matrix		GW energy	
Energy cutoff	35Ry	Screened Coulomb cutoff	35 Ry
Number of empty bands	2000	Number of empty bands	2000
Number of k points	$18 \times 18 \times 1$	Number of k points	$18 \times 18 \times 1$
BSE interaction kernel		Diagonalization of BSE	
Number of bands	26	Number of bands	12
Number of k points	$18 \times 18 \times 1$	Number of k points	$36 \times 36 \times 1$

Table 8.2: Calculation conditions of GW+BSE calculation in graphane.

GW energy band gap at Γ point within 100meV required 2000 empty bands and this is quite larger than that of previous studies [58]. As a consequence we obtained GW band gap at Γ point as 6.8eV, and this is also greater than the results of previous studies summarized in table 8.3 [58–61] . The origin of band gap discrepancy is possibly due to the small number of empty bands for making up the dielectric matrix and for calculating the GW energy, which is typically the order of 10% of our case. Actually when we used the small number of empty bands (100 bands) we obtained the GW band gap as 6.0eV and this is much closer to the values of preceding studies [58–61].

E_{gap}^{GW} at Γ[eV] point	method	functional	literature
5.64	G_0W_0	PBE	F. Karlicky et al. (2012) [60]
5.83	G_0W_0	HSE06	F. Karlicky et al. (2012) [60]
5.89	GW_0	PBE	F. Karlicky et al. (2012) [60]
5.95	GW_0	HSE06	F. Karlicky et al. (2012) [60]
6.28	GW	PBE	F. Karlicky et al. (2012) [60]
6.17	GW	HSE06	F. Karlicky et al. (2012) [60]
5.4	G_0W_0	LDA	P. Cudazzo et al. (2010) [58]
6.05	GW	PBE	O. Leenaerts et al. (2010) [61]

Table 8.3: Theoretically calculated GW band gap in literatures.

In the figure 8.4 we show the energy spectrum of spin-singlet exciton. The energy is measured from the valence band maximum and hence the lowest exciton binding energy amounts to 1.55eV. Although this binding energy is quite larger than that of exciton in diamond (80meV) for example, this is typical in monolayer material system of graphene derivatives since exciton

binding energies of chlorographene and fluorographene are reported to be 1.3 eV and 1.9 eV by using GW+BSE calculation [60]. In spite of the large discrepancy of GW band gap, the lowest exciton binding energy shows good agreement with the results of previous studies. In the region close to GW conduction band minimum, the level spacing is small and being almost continuum. For optical manipulation of excitonic states, large energy level interval is favorable and hence we show the first ten excitonic levels in figure 8.5. We named these levels as A_1, A_2, ..., E_3 from the energetically lower levels. We also plotted the real part of excitonic wave function $\Psi(\boldsymbol{r}_e, \boldsymbol{r}_h)$, where $\Psi(\boldsymbol{r}_e, \boldsymbol{r}_h)$ is defined as

$$\Psi(\boldsymbol{r}_e, \boldsymbol{r}_h) = \sum_{\boldsymbol{k}} \sum_{i}^{\text{c.b.}} \sum_{j}^{\text{v.b.}} A_{\boldsymbol{k}ij} \phi_i(\boldsymbol{r}_e) \phi_j(\boldsymbol{r}_h)^*. \tag{8.1}$$

To depict the wave function, the hole position is fixed on the middle point of C-C bonding. In the next section, we will see how each states can be coupled via electromagnetic field and what models can be constructed for trapping the A_1 and A_2 state.

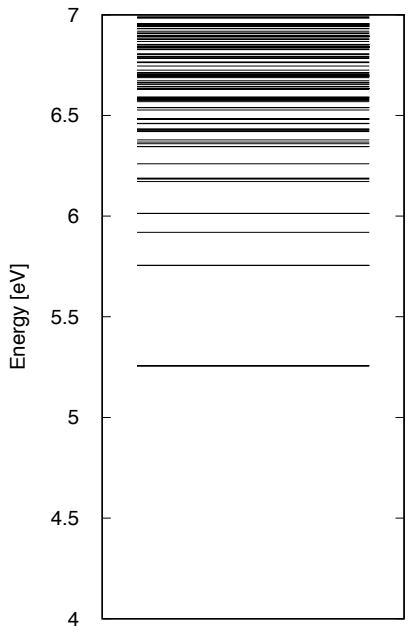

Figure 8.4: The excitonic energy spectrum of graphane given by solving the Bethe-Salpeter equation. The vertical axis is measured from the valence band maximum at Γ point.

8.2 Optical lattices and optical exciton filters

In the last section we introduced the energy level structure of spin-singlet exciton of graphane and found that the lowest few levels have wide level spacing and would be superior for optical manipulation. In this section we focus on the first five excitonic levels and show that the two-level system and the three-level system we introduced in chapter 7.1 can be actually realized. Our main achievements of this section are showing the feasibility of, firstly the optical potential, secondly the state-selective optical filter.

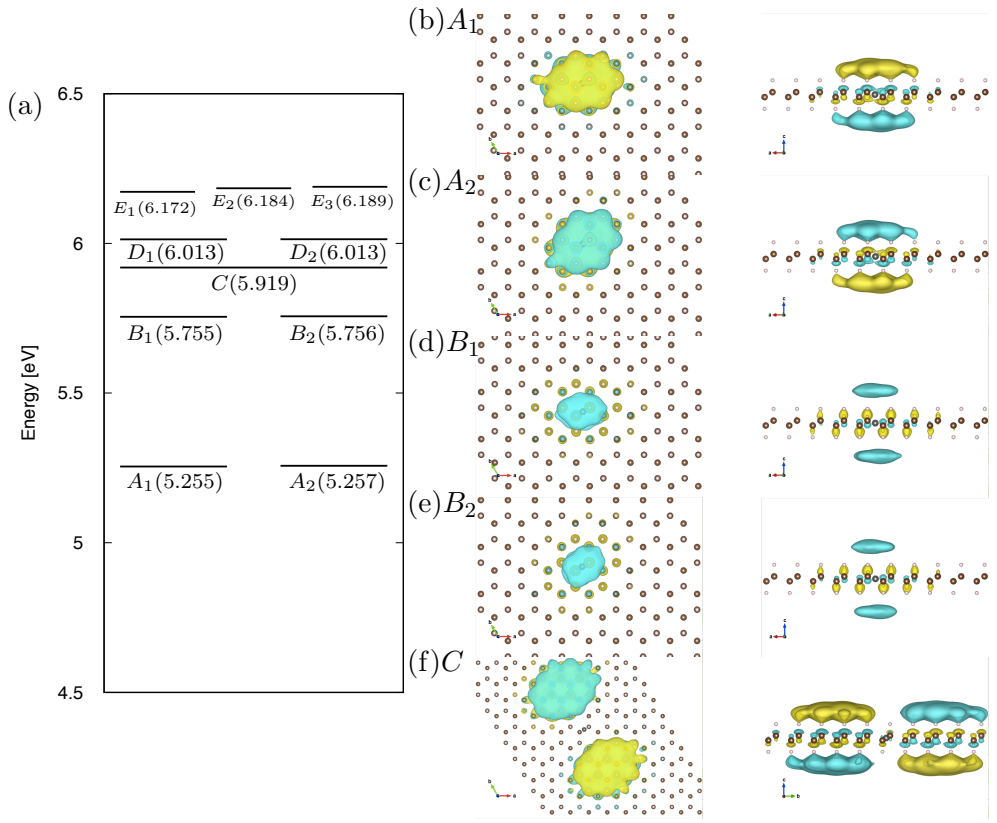

Figure 8.5: (a) The lowest ten excitonic levels. Their energy are shown in brackets in units of eV. The real part of wave function of (b)A_1, (c)A_2, (d)B_1, (e)B_2 and (f)C level are shown in right hand side.

8.2.1 Transition dipole moment

As we showed in 7.1, when we used the dipole approximation about the interaction between matter and light, the coupling strength between two quantum states i and j are given as the Rabi frequency Ω_{ij} which is defined by

$$\Omega_{ij} \equiv \left| \frac{2\boldsymbol{d}_{ij} \cdot \boldsymbol{E}}{\hbar} \right|, \tag{8.2}$$

where $\boldsymbol{d}_{ij}$ is the transition dipole moment and the $\boldsymbol{E}$ is the electric field. In table 8.4 we show the calculated value of $\boldsymbol{d}_{ij}$ divided by the unit charge e for the lowest five excitonic levels in the atomic unit. Important point is that the coupling between $|A_1\rangle$ and $|B_2\rangle$, and between $|A_2\rangle$ and $|B_1\rangle$ is smaller than one tenth the value of other couplings. This is a reasonable result. The two excitonic state pairs, A_1 and A_2, B_1 and B_2, are almost degenerate. Assuming that each states belong to the representations of D_{3d} group, only E_g and E_u are two-dimensional representation and can be the origin of degeneracy. The wave function plot in figure 8.5 indicates $A_{1,2}$ belong to E_u and $B_{1,2}$ belong to E_g. Then the transition dipole moment clearly vanishes judging from the typical basis function of $E_{g,u}$. The Rabi frequency appears squared form in the dressed state and its eigenvalue hence we can neglect the weak coupling.

Thus the troublesome lowest four-level system can be divided into independent two two-level systems. Then the whole five-level system can be decomposed into two two-level systems $((A_1, B_1),(A_2, B_2))$ and single three-level system(A_1, A_2, C) and they can be treated within the framework we introduced in the last section. In the next two subsections, we will see how the

	x	y	z
$\boldsymbol{d}_{A_1,B_1}$	$(-7.0\times10^{-3}, 1.3\times10^{-2})$	$(-5.0\times10^{-3}, 2.3\times10^{-2})$	$(4.1\times10^{-1}, 7.1\times10^{-1})$
$\boldsymbol{d}_{A_1,B_2}$	$(3.0\times10^{-3}, -2.0\times10^{-3})$	$(-2.0\times10^{-3}, -8.0\times10^{-3})$	$(6.1\times10^{-2}, -2.3\times10^{-2})$
$\boldsymbol{d}_{A_2,B_1}$	$(2.0\times10^{-3}, -1.0\times10^{-3})$	$(-2.0\times10^{-3}, 6.0\times10^{-3})$	$(-6.1\times10^{-2}, 2.4\times10^{-2})$
$\boldsymbol{d}_{A_2,B_2}$	$(6.0\times10^{-3}, 1.6\times10^{-2})$	$(3.0\times10^{-3}, 2.6\times10^{-2})$	$(-5.1\times10^{-1}, -8.1\times10^{-1})$
$\boldsymbol{d}_{A_1,C}$	$(-5.2\times10^{-1}, 1.8\times10^{-1})$	$(-5.5\times10^{-1}, 7.1\times10^{-1})$	$(-4.5\times10^{-4}, -2.5\times10^{-4})$
$\boldsymbol{d}_{A_2,C}$	$(-8.1\times10^{-1}, 5.2\times10^{-1})$	$(-1.8, 7.6\times10^{-1})$	$(-1.0\times10^{-3}, 1.0\times10^{-3})$

Table 8.4: Theoretically calculated transition dipole moment $\boldsymbol{d}_{ij}$ divided by the unit charge e, where $\boldsymbol{d}_{ij} = \langle i|e\boldsymbol{r}|j\rangle$, between excitonic states in the atomic unit. Since $\boldsymbol{d}_{ij}$ is complex value, both real and imaginary components are shown for x, y, and z component.

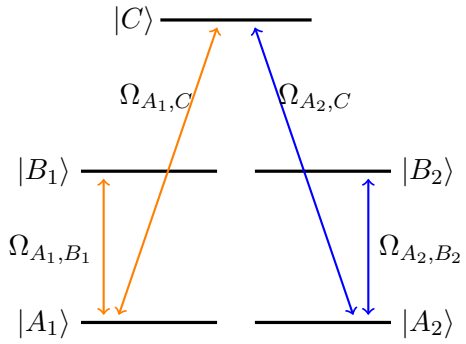

Figure 8.6: Schematic picture of the lowest five excitonic levels of graphane. This five-level system is decomposed into two two-level system $((A_1, B_1),(A_2, B_2))$ and a three-level system(A_1, A_2, C).

optical potential (8.2.2) and the optical filter(8.2.3) can be applied in these systems. Before discussing each of the systems, we estimate the order of recoil energy $\hbar^2\boldsymbol{k}^2/2m_{\rm ex}$, where $\boldsymbol{k}$ is the wave vector of emitted photon from a higher energy level, and $m_{\rm ex}$ is the exciton effective mass. Approximating that the energy spacing between $A_{1,2}$ and $B_{1,2}$ equals 0.50eV and that of $A_{1,2}$ and C equals 0.76eV, the recoil energy E_R amounts to 1.36×10^{-4}meV and 3.14×10^{-4}meV, respectively. Here we used the theoretically calculated exciton effective mass of graphane $m_{\rm ex}\simeq 1.8m_0$ using GW+BSE calculation in a recent work [62].

8.2.2 Optical potential in a two-level system

As we showed in the previous section the four excitonic states $A_{1,2}$ and $B_{1,2}$ forms two independent two-level system when the system is driven by $\hbar\omega\sim 500$meV. Here we introduce the analytical form of the dressed state Eq. (7.63) and the optical potential Eq. (7.66) again:

$$|+\rangle = -\sin\frac{\theta}{2}e^{-i\phi/2}|k\rangle+\cos\frac{\theta}{2}e^{i\phi/2}|l\rangle, \tag{8.3}$$

$$|-\rangle = \cos\frac{\theta}{2}e^{-i\phi/2}|k\rangle+\sin\frac{\theta}{2}e^{i\phi/2}|l\rangle. \tag{8.4}$$

$$U_{op}^{(\pm)} = \mp\frac{\hbar}{2}(\sqrt{\Delta^2+\Omega_R^2}-\sqrt{\Delta^2}). \tag{8.5}$$

In this case, $|k\rangle=|B_1\rangle(|B_2\rangle)$ and $|l\rangle=|A_1\rangle(|A_2\rangle)$. It is helpful to see how the amplitude of $A_{1,2}$ and $B_{1,2}$ in the dressed state $|\pm\rangle$ changes depending on the value of detuning Δ. For two limit cases, $\Delta\gg\Omega_R$ and $\Delta\ll\Omega_R$, the dressed states $|\pm\rangle$ converges to $|k\rangle$ or $|l\rangle$ as follows:

$$|+\rangle\simeq\begin{cases}|k\rangle & (\Delta\gg\Omega_R)\\ |l\rangle & (\Delta\ll\Omega_R)\end{cases},\ |-\rangle\simeq\begin{cases}|l\rangle & (\Delta\gg\Omega_R)\\ |k\rangle & (\Delta\ll\Omega_R).\end{cases} \tag{8.6}$$

The condition $\Delta>\Omega_R$ is called *blue detuning* and the condition $\Delta<\Omega_R$ is called *red detuning*. Then we show the $U_{op}^{(\pm)}$ in figure 8.7 by taking the detuning for vertical axis and the laser intensity for horizontal axis. The Rabi frequency and the laser intensity has one to one correspondence. In figure 8.7 $\hbar\Omega_R$ runs from 8.66×10^{-3}meV to 8.66×10^{-2}meV for the pair of A_1 and B_1, and from 1.01×10^{-2}meV to 1.01meV for the pair of A_2 and B_2. Since the direction of transition dipole moment between $A_{1,2}$ and $B_{1,2}$ is almost normal to the graphane crystal, we fixed the polarization vector normal to the graphane plane. In figure 8.7(a), U_{op}^- has positive value that means for far blue detuning case, where $|-\rangle\sim|A_1\rangle$, the A_1 exciton will be trapped on the nodes of electromagnetic standing wave. On the other hands, in figure 8.7(c), U_{op}^+ has negative value that means for far red detuning case, where $|+\rangle\sim|A_1\rangle$, the A_1 exciton will be trapped on the antinodes. And so does for the case of figure 8.7(b) and (d). These behaviors are qualitatively same with those of a two-level atomic system. Due to the difference of the magnitude of $\boldsymbol{d}_{A_1,B_1}$ and $\boldsymbol{d}_{A_2,B_2}$, the potential depth for A_2 and B_2 is deeper.

8.2.3 State-selective potential and exciton type conversion in a three-level system

In this subsection we discuss the three-level system composed of A_1, A_2, and C excitonic levels. As we mentioned in the previous section the eigenstates of this three-level system is

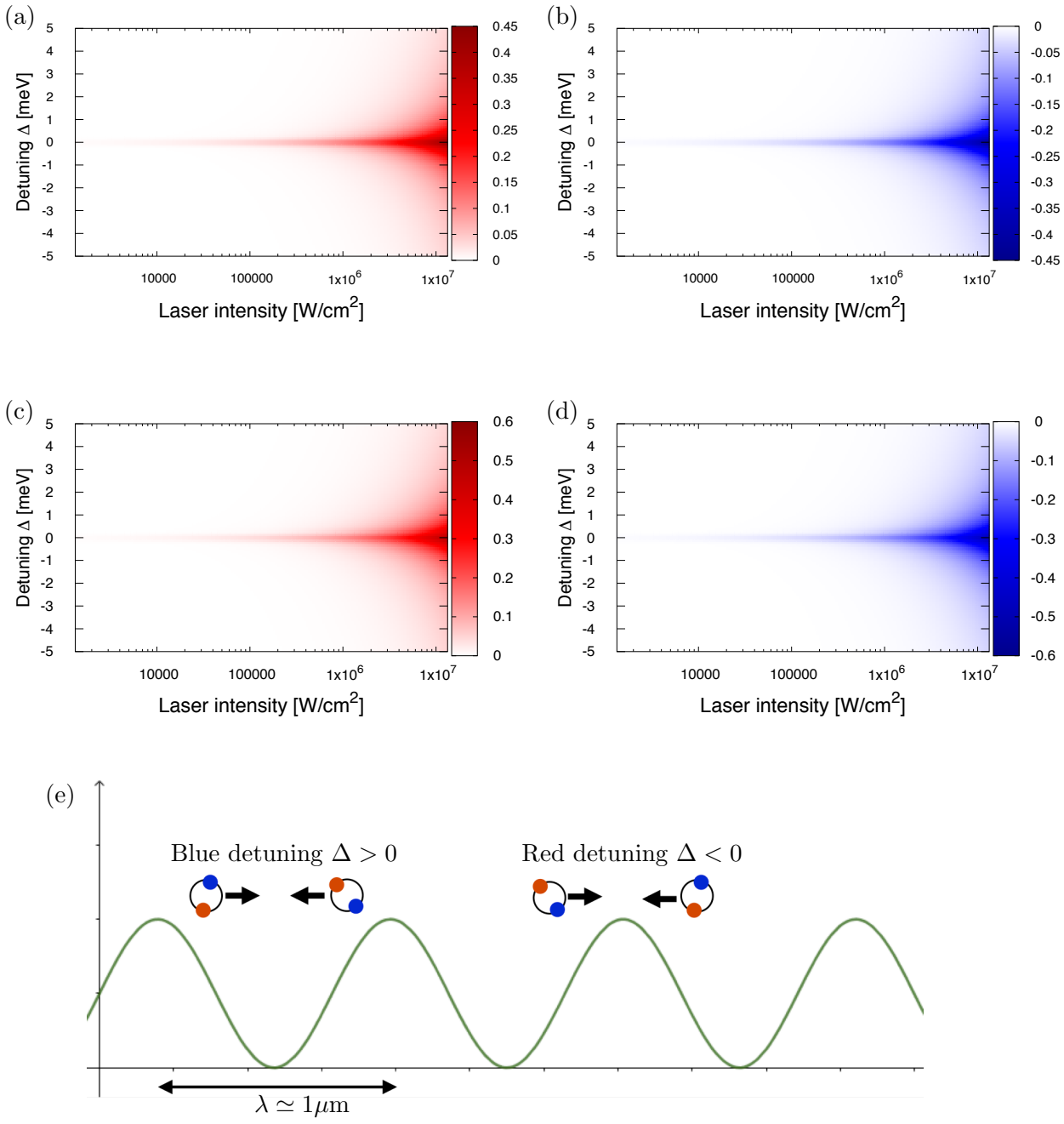

Figure 8.7: Dependency of the optical potential $U_{op}^{(\pm)}$ on the laser intensity [W/cm^2] in units of meV. (a) U_{op}^{-} for (A_1, B_1), (b) U_{op}^{+} for (A_1, B_1), (c)U_{op}^{-} for (A_2, B_2) , (d) U_{op}^{+} for (A_2, B_2). (e)Schematic picture of exciton trapping by a laser standing wave (green line). When the detuning is set as $\Delta > 0$, A_1 and A_2 excitons will be trapped on nodes (blue detuning), and when $\Delta < 0$ A_1 and A_2 excitons will be trapped on antinodes (red detuning). λ is the lattice periodicity which is given by a half of laser wave length.

given by:

$$|0\rangle = (-\Omega_{A_2,C}, 0, \Omega^*_{A_1,C})/C_0,\ |\pm\rangle = (\Omega_{A_1,C}, \Delta \pm \Omega_{\rm eff}, \Omega^*_{A_2,C})/C_\pm, \tag{8.7}$$

and the optical potential for $u_\pm$ states is

$$U^{(\pm)}_{op} = \mp\frac{\hbar}{2}\{\Omega_{\rm eff} - \sqrt{\Delta^2}\}. \tag{8.8}$$

Characteristic of this system is that u_0 has no energy shift. In the far detuned limit, $u_\pm$ behave as follows:

$$|+\rangle \simeq \begin{cases} |C\rangle & (\Delta \gg \Omega_{\rm eff}) \\ \Omega_{A_1,C}|A_1\rangle + \Omega^*_{A_2,C}|A_2\rangle & (\Delta \ll \Omega_{\rm eff}) \end{cases}, \tag{8.9}$$

$$|-\rangle \simeq \begin{cases} \Omega_{A_1,C}|A_1\rangle + \Omega^*_{A_2,C}|A_2\rangle & (\Delta \gg \Omega_{\rm eff}) \\ |C\rangle & (\Delta \ll \Omega_{\rm eff}). \end{cases} \tag{8.10}$$

Thus, if $|\Omega_{A_1,C}|^2 \gg |\Omega_{A_2,C}|^2$ we can selectively trap the A_1 exciton, and vice versa.

Our interest is that if we can realize this situation. In this three-level system, the component of transition dipole moment $\boldsymbol{d}_{A_1,C}$ and $\boldsymbol{d}_{A_2,C}$ is almost confined in the xy-plane which is parallel to the graphane crystal. We analyzed the value of two Rabi frequency $\hbar|\Omega_{A_1,C}|$ and $\hbar|\Omega_{A_2,C}|$ for three cases, where the polarization of the external field is circularly polarized against the wave vector as *i.* clockwise (σ_+) and *ii.* counter clockwise (σ_-), or *iii.* linearly polarized. For *i* and *ii* we defined the direction of the wave vector $\boldsymbol{e}_k$ as:

$$\boldsymbol{e}_k = R_z(\phi - \pi/2)R_x(-\theta)\begin{pmatrix}0\\0\\1\end{pmatrix} = \begin{pmatrix}\sin\theta\cos\phi\\ \sin\theta\sin\phi\\ \cos\theta\end{pmatrix}, \tag{8.11}$$

then the polarization vector $\boldsymbol{e}_{\sigma_+}$ and $\boldsymbol{e}_{\sigma_-}$ become

$$\boldsymbol{e}_{\sigma_+} = R_z(\phi - \pi/2)R_x(-\theta)\frac{1}{\sqrt{2}}\begin{pmatrix}0\\1\\i\end{pmatrix} = \frac{1}{\sqrt{2}}\begin{pmatrix}\sin\phi + i\cos\theta\cos\phi\\ -\cos\phi + i\sin\phi\cos\phi\\ -i\sin\theta\end{pmatrix}, \tag{8.12}$$

$$\boldsymbol{e}_{\sigma_+} = R_z(\phi - \pi/2)R_x(-\theta)\frac{1}{\sqrt{2}}\begin{pmatrix}0\\1\\-i\end{pmatrix} = \frac{1}{\sqrt{2}}\begin{pmatrix}\sin\phi - i\cos\theta\cos\phi\\ -\cos\phi - i\sin\phi\cos\phi\\ i\sin\theta\end{pmatrix}. \tag{8.13}$$

And for *iii.* , we defined the linearly polarized vector $\boldsymbol{e}$ as just a real vector:

$$\boldsymbol{e} = (\sin\theta\cos\phi, \sin\theta\sin\phi, \cos\theta). \tag{8.14}$$

Here we introduced the rotational operation about x-axis (R_x) and z-axis (R_z).

The calculated results are plotted in figure 8.8 as a function of angle θ and ϕ. The laser intensity is fixed in 1.33×10^7W/cm^2 in this figure. We can see strong angular dependency for all polarization type, and its dependency is different between $\hbar|\Omega_{A_1,C}|$ and $\hbar|\Omega_{A_2,C}|$. To see how strongly one state can be suppressed, we also plotted the squared ratio $|\Omega_{A_2,C}|^2/|\Omega_{A_1,C}|^2$ in figure 8.9 for the cases of *i* , *ii* and *iii* . Figure 8.9 (a) means when the wave vector $\boldsymbol{e}_k$ is

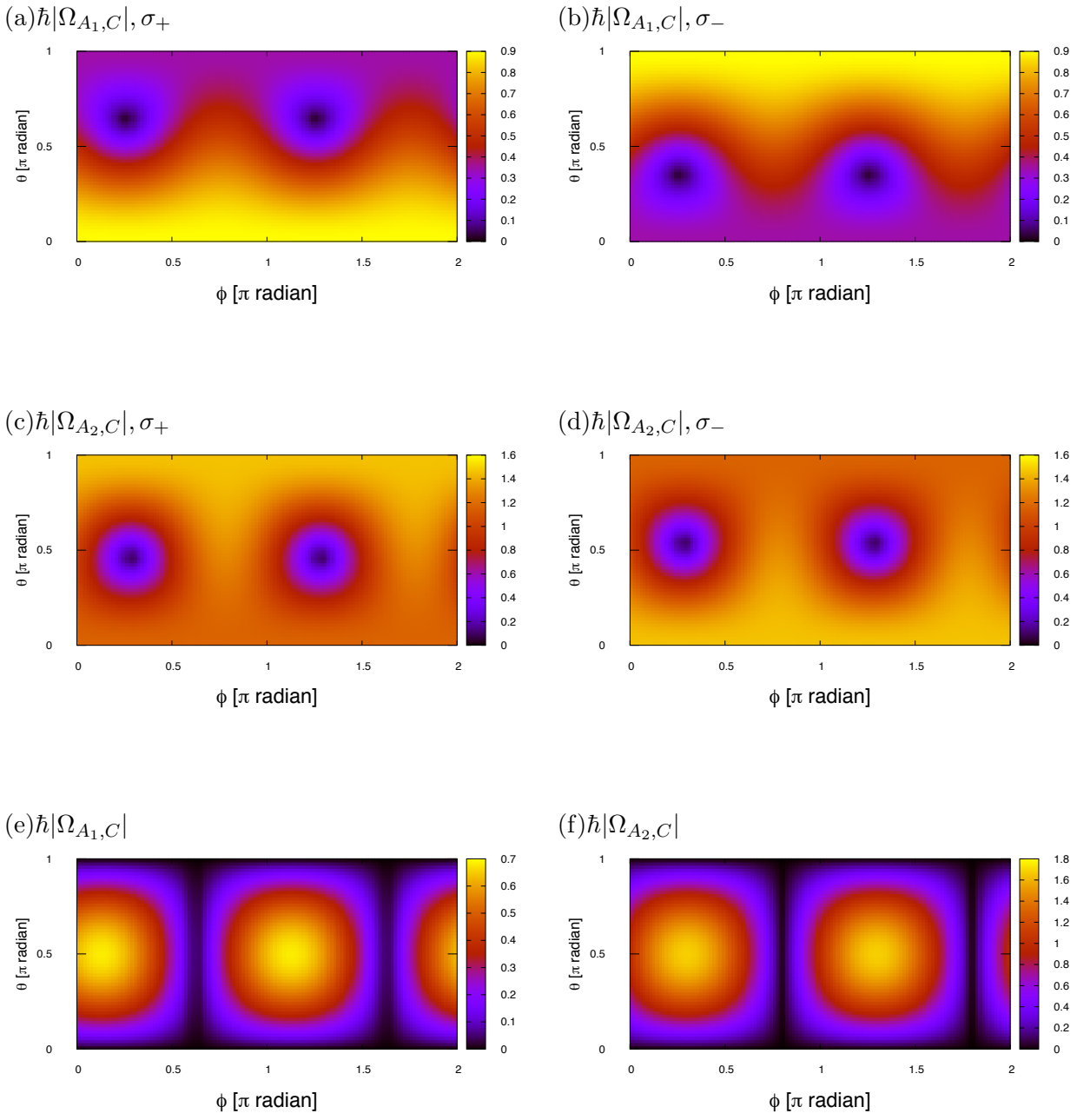

Figure 8.8: Angular dependency of the Rabi frequency on the polarization vector in units of meV. The value of (a) $\hbar|\Omega_{A_1,C}|$ coupled by $\boldsymbol{e}_{\sigma_+}$, (b) $\hbar|\Omega_{A_1,C}|$ coupled by $\boldsymbol{e}_{\sigma_-}$, (c)$\hbar|\Omega_{A_2,C}|$ coupled by $\boldsymbol{e}_{\sigma_+}$, (d) $\hbar|\Omega_{A_2,C}|$ coupled by $\boldsymbol{e}_{\sigma_-}$, (e) $\hbar|\Omega_{A_2,C}|$ coupled by linearly polarized field and (f) $\hbar|\Omega_{A_2,C}|$ coupled by linearly polarized field. The laser intensity is fixed in $1.33\times10^7\mathrm{W/cm}^2$.

directed along $(\theta, \phi) \sim (0.65\pi, \pi/4),\ (0.65\pi, 5\pi/4)$, where bright spots are on this figure, the population of A_1 exciton is suppressed below 1% and we can apply the optical potential only for A_2 exciton. Same discussion can be done for the case of figure 8.9 (b) and figure 8.9 (c). We plotted the value of U_{op}^{-} in figure 8.9 (d) where the polarization vector of laser is $\boldsymbol{e}_{\sigma_+}$ and the wave vector $\boldsymbol{e_k}$ is directed at $(\theta, \phi) = (3\pi/4, \pi/4)$. In this condition the population of A_1 exciton is about 2.3% of the value A_2 exciton in $|-\rangle$. Thus, with an appropriate choice of the angle of wave vector and polarization type, we can induce a sub meV depth optical potential only for A_2 exciton.

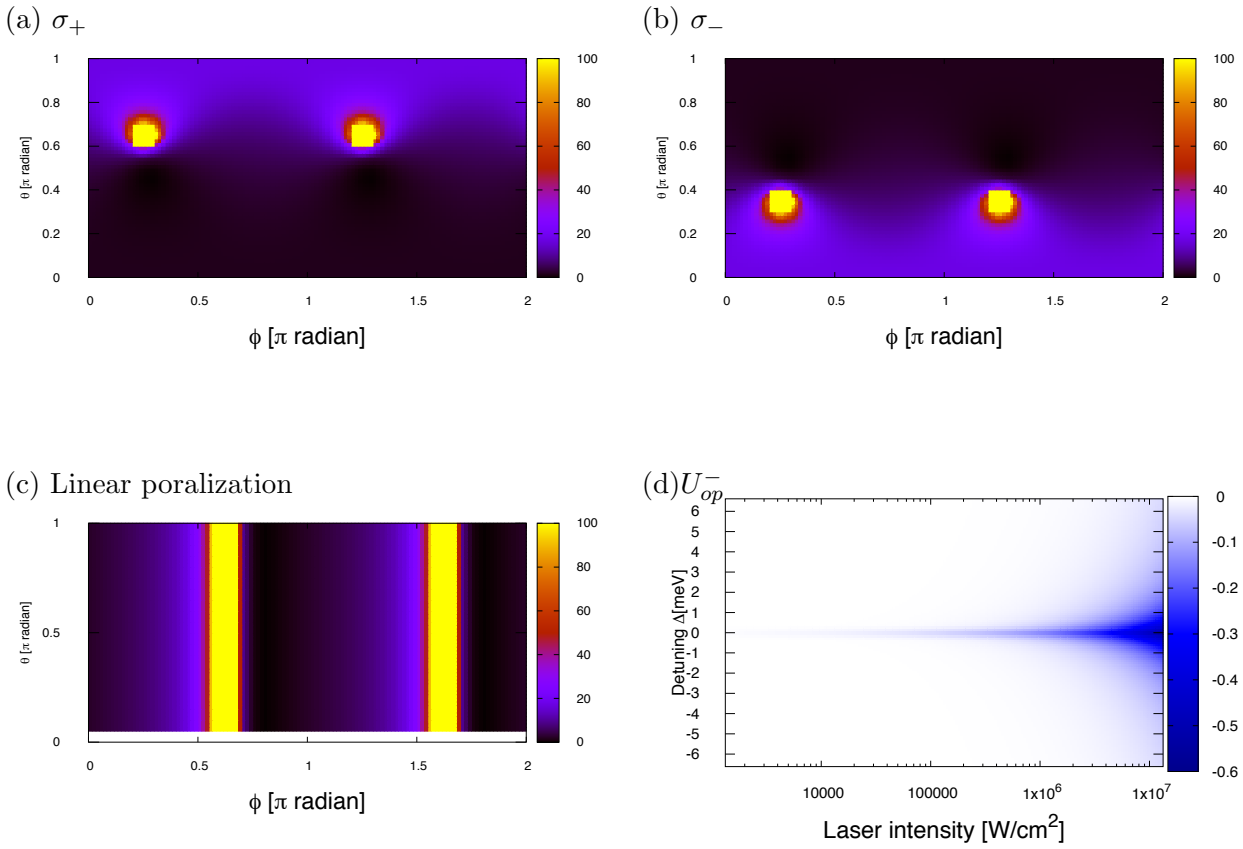

Figure 8.9: The angular dependency of $|\Omega_{A_2,C}|^2/|\Omega_{A_1,C}|^2$ when the polarization vector of laser is (a)$\boldsymbol{e}_{\sigma^+}$, (b)$\boldsymbol{e}_{\sigma^-}$, and (c)linearly polarized. (d)The value of U_{op}^{-} in units of meV when the polarization vector of laser is $\boldsymbol{e}_{\sigma^+}$ and the angle of wave vector is $(\theta, \phi) = (3\pi/4, \pi/4)$.

8.3 Energy correction by higher energy levels

In this section we verify the validity of our few-level model by numerical diagonalization. Starting from Eq. (7.24) we firstly transform expansion coefficients a_n as:

$$a_n(t) = \tilde{a}_n(t)e^{-i\eta_n t} \tag{8.15}$$

$$\eta_n = \begin{cases} \omega_A \ (n = A_1, A_2) \\ \omega + \omega_A \ (n = B_1, B_2) \\ \omega + \omega_B - \Delta_{BA} \ (\text{otherwise}) \end{cases} . \tag{8.16}$$

Here we regarded $A_1(B_1)$ and $A_2(B_2)$ are degenerate with each other. ω is the frequency of external field and $\hbar\omega_{A(B)}$ is the energy of $A_1(B_1)$ level. Δ_{BA} is defined by $\Delta_{BA} \equiv \omega - (\omega_B - \omega_A)$. By neglecting rapidly oscillating term with frequency $\pm\omega$ we can obtain an equation of motion for $\tilde{a}_n(t)$ as:

$$i\hbar\dot{\tilde{a}}_{A_m} = \frac{\hbar}{2}\sum_n \Omega^*_{B_n A_m}\tilde{a}_{B_n}, \tag{8.17}$$

$$i\hbar\dot{\tilde{a}}_{B_m} = -\hbar\Delta_{BA} + \frac{\hbar}{2}\sum_n \Omega_{B_m A_n}\tilde{a}_{A_n}, \tag{8.18}$$

$$i\hbar\dot{\tilde{a}}_k = -\hbar(\Delta_{nB} + \Delta_{BA}) + \frac{\hbar}{2}\sum_n \Omega^*_{B_n k}\tilde{a}_{B_n}, \tag{8.19}$$

where $A_m = A_1, A_2$, $B_m = B_1, B_2$, $k \neq A_1, A_2, B_1, B_2$, and $\Delta_{nB} \equiv \omega - (\omega_n - \omega_B)$. When $\Omega_{B_n k}, \Omega_{A_1 B_2}, \Omega_{A_2 B_1} = 0$, this model becomes equivalent to what we introduced in two-level system. Though the number of higher energy levels must be infinite, we can only include a finite number of levels. In figure 8.10 we show how the $U^{\pm}_{op}$ depend on the number of levels

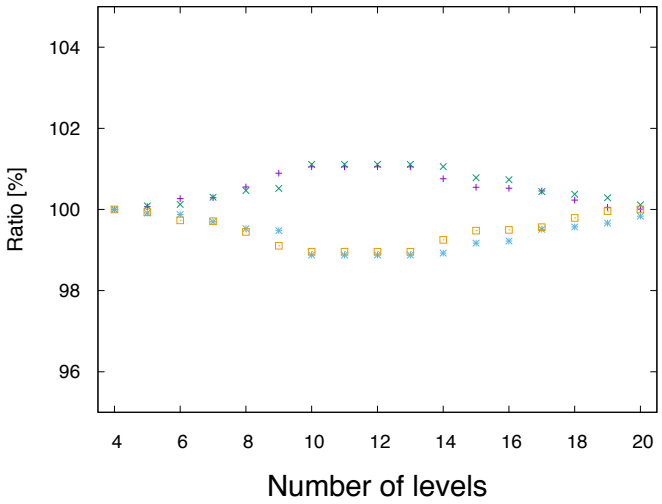

Figure 8.10: This picture shows how the $U^{\pm}_{op}$ depends on the number of levels in Eqs. (8.19). Vertical axis denotes ratio by percentage. When the number of levels is four, it gives 100 %.

in Eqs. (8.19). In this calculation the polarization vector $\boldsymbol{e} = (0, 0, 1)$, the field intensity is 1.33×10^7 W/cm^2, and the detuning $\Delta_{BA} = 0$. When the number of levels is 20, the energy

discrepancy from the case of four-level system is 0.2% at maximum. We also emphasize that the contribution of $\Omega_{B_1A_2}$ and $\Omega_{B_2A_1}$ is 0.3% at maximum in this condition. It means the four-level system composed of A_1, A_2, B_1, and B_2 is well described by independent two two-level systems as we saw in the previous sections. We also examined polarization vector $\boldsymbol{e} = (\sin\theta, 0, \cos\theta)$ dependency for $\theta : 0 \to \pi/2$ in figure 8.11. When $\theta = 0$ the polarization vector is normal to the

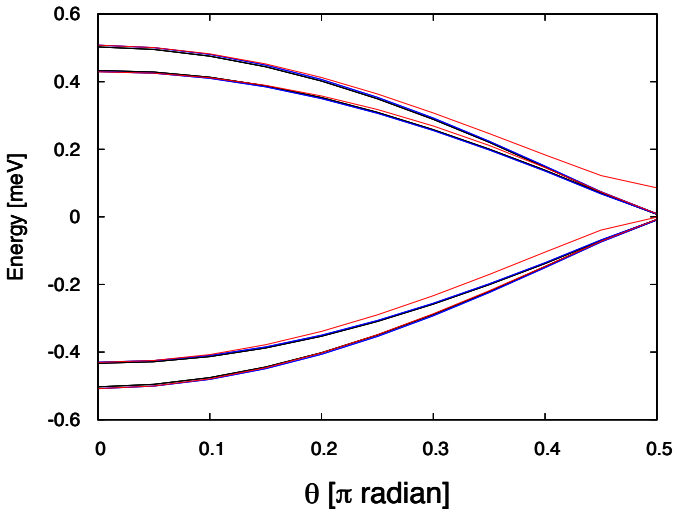

Figure 8.11: This picture shows how the $U_{op}^{\pm}$ depend on the polarization vector of external field $\boldsymbol{e} = (\sin\theta, 0, \cos\theta)$. The blue lines is the case of four-level system and the red lines are the case of 20-level sytem.

lattice and when $\theta = \pi/2$ it is parallel. The $U_{op}^{\pm}$ show large deviation when $\boldsymbol{e}$ is close to parallel with lattice plain. When $\theta = 0.4\pi$ the deviation exceeds 24 %. The stronger the field intensity is, the larger the amplitude of deviation becomes. When the field intensity is 1.33×10^8 W/cm^2 the deviation amounts to 40 % with $\theta = 0.35\pi$. Thus we can conclude that the four-level model which neglects higher energy levels quantitatively well describes the system within the range of field intensity we used in the previous sections.

8.4 Heating process by the radiation pressure

As we saw in 7.2.2, it is possible to roughly estimate the inflow of energy via the spontaneous photoemission. At this moment it is not certain if a mechanism of balancing between the photon heating process and the phonon cooling process is important in our system. Firstly we estimate the relaxation time of transitions between states by calculating the inverse lifetime Γ in Eq. (7.151). By integrating over the solid angle and by doing sum over two polarizations, we can derive

$$\Gamma_{ij} = \frac{\omega_{ij}^3}{3\pi\hbar\epsilon c^3}|\boldsymbol{d}_{ij}|^2 \tag{8.20}$$

for a pair of states, i and j. Here we show the calculated value of the lifetime $\tau_{ij} = \Gamma_{ij}^{-1}$ in table 8.5 for five excitonic states A_1, A_2, B_1, B_2, and C. A state g denotes the ground state. The lifetime of transitions between the ground state and A_1, A_2 are in the order of nano seconds

state	g	g	B_1	B_1	B_2	B_2	A_1	A_2
	A_1	A_2	A_1	A_2	A_1	A_2	C	C
τ_{ij}[ns]	105	68	11×10^3	1.7×10^6	1.8×10^6	8.4×10^3	3.9×10^3	1.0×10^3

Table 8.5: The calculated lifetime τ_{ij} of transitions between two states i and j in units of nano second.

and much shorter than other possible transitions. This result is indicating that the A_1 and A_2 excitons decay before receiving the momentum transfer from photons emitted by transitions between A_1, A_2 excitons and B_1, B_2, C excitons.

Nevertheless the heating process can be expected to be negligible, we show R_{photon} in Eq. 7.150, the kinetic energy income per unit time for a reference in figure 8.12. In figure 8.12 the

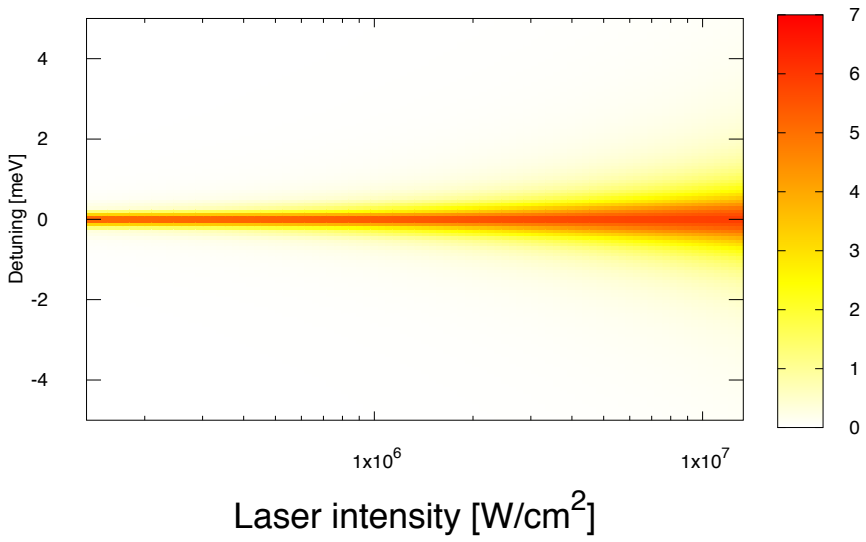

Figure 8.12: Inflow of the kinetic energy per unit time R_{photon} in units of meV/s for two-level system composed of A_1 and B_1 exciton.

calculated value of R_{photon} for a two-level system composed of A_1 and B_1 exciton is shown. The value is several meV per second at most, hence completely negligible in the time scale of A_1 exciton's lifetime.

Thus the heating process turned out to be minor effect when we try to trap spin-singlet excitons with zero center-of-mass momentum. However, we point out that the heating effect may possibly be a matter when we try to trap dark excitons. Excitons are only weakly coupled to the light when a carrier recombination process requires spin-flip of electrons, or exciton center-of-mass momentum is large. Such excitons are called dark excitons, and in general it has longer lifetime than that of bright excitons. Since we are considering the relaxation process between inner excitation levels which are not accompanied by spin-flip or momentum transfer, the dark excitons may survive sufficiently long time to emit many photons. In that case we need to seriously consider the heating process competing with the cooling process by emitting phonons.

8.5 Arbitrariness of the expression of degenerate states

In this section we discuss how the arbitrariness of expressing degenerate states A_1 and A_2 affects the interpretation of results in section 8.2. Since we are considering doubly degenerate states A_1 and A_2, energetically lowest excitons in graphane can be expressed by a linear combination of A_1 and A_2 exciton in general. Our results in former sections correspond to a special case of possible linear combinations.

In section 8.2.2 we assumed a linearly polarized light to induce an optical potential. In this case the optical potential does not have a strong tendency of trapping one of degenerate states. Then we can expect that any linear combination state will be equally trapped by an optical potential. On the other hand in section 8.2.3 we saw that the circularly polarized light selectively induce optical potential on one of degenerate excitonic states. Provided that the population of excited states is negligibly small, excitonic states can be mapped as a Bloch vector in Bloch sphere where its north and south pole corresponds to A_1 and A_2 state, respectively. It means that there is an energetically special direction for the Bloch vector corresponding to an excitonic state. Therefore we can expect that the Bloch vector will flip and align with the special direction. However, we need to confirm our expectations by a mathematically exact way and it is a future work of this thesis.

9. SUMMARY OF PART II

In this section we give a short summery of part II. Our motivation in this part is investigating the feasibility of optical manipulation techniques in excitonic systems in solids. This study is stimulated by the development of ultra-cold atomic system in past few decades. One of the central techniques supporting their successes is the optical confinement technique of neutral atoms, which is called optical potential. Its brief mechanism is inducing energy level shift of atoms by irradiating laser fields which is nearly resonant to the energy level intervals of atoms.

In chapter 7 we introduced several theoretical frameworks. In section 7.1 we gave an explanation for the physical mechanism of realizing optical potential in a two-level system. We saw the time-evolution of two-level system is easily understood by introducing the concept of Bloch vector. Stationary solution of two-level system is called the dressed state, and the spatial modulation of their eigenvalue works as a periodic optical potential. In section 7.1.4 we developed our discussion to a three-level system. Although its stationary solution can not be easily understood as we did in the last section, we could get analytical solutions. In section 7.2 we introduce a theoretical formalism to discuss the heating effect originating from the spontaneous photo-emission of excited states. By considering a quantization of electromagnetic field, this effect can be naturally included in our model. We saw that the energy income by heating process is roughly estimated by a stationary solution of the optical Bloch equation. In the subsequent section we introduced the mechanism of possible cooling process for excitons by emitting phonons.

In section 7.4 we summarized first principles methods for calculating the excitonic spectrum and the excitonic wave function. We used the GW+BSE method in combination with the density functional theory (DFT). The DFT is the most widely used method to calculate electronic structure of materials by ab initio method, though it has a problem of systematic underestimation of the band gap. The GW approximation can successfully correct the underestimation of the band gap. The Bethe-Salpeter equation is used to calculate excitonic states of solids. The GW+BSE method is considered as one of the most accurate method for simulating the optical gap of materials.

In chapter 8 we chose graphane, a two-dimensional semiconductor with a wide direct band gap. Graphane is suitable for a test case for investigating the feasibility of optical potential in excitonic system thanks to its simple band structure and huge exciton binding energy. We revealed that the lowest five level is available to implement the optical potential in section 8.1. These levels are decomposed into two two-level systems and one three-level system. In section 8.2 we show the possible depth of optical potential and revealed required conditions such as laser intensity and polarization dependency. To check the validity of our few-level model we numerically confirmed the energy correction by higher energy levels in 8.3. We could show that the correction does not become serious within the range of field intensity we used in the previous section. We also clarified that the heating effect is negligible as long as we are considering to

trap bright excitons.

We finally give a short comment about an experimental setup for implementing the optical trap. For utilizing our computational result the crystal of graphane must be suspended and cannot be put on any substrate. It is because the electronic state of two-dimensional material is strongly affected by screening effect of surroundings [63]. A laser standing wave will be prepared by using a mirror and a laser beam. Since typical beam radius amounts to $\mathrm{O}(10^2)$ μm, it seems not so difficult to put a crystal inside a laser standing wave.

10. CONCLUDING REMARKS

10.1 Summary of this thesis

In this thesis we accomplished two theoretical studies in the field of excitonic physics. The first one is a numerical investigation of the polyexciton stability in diamond. We succeeded in showing the stability of excitonic particles such as excitons, trions, biexcitons, chrged biexcitons, and triexcitons. The formation of charged biexcitons and triexcitons are unique in a system with multiple valleys and bands. The second one is a theoretical study for investigating the feasibility of optical confinement techniques of excitons in graphane. We clarified that the optical potential of the order of $10^2\mu$eV depth can be realized. The spatial periodicity is determined by a half wave length of laser light. In this case it is the order of 1 μm. In the followings we give more detailed summaries for each study.

In part I study we investigated the polyexciton stability in diamond. Although small excitonic complexes such as excitons, trions, and biexcitons are both experimentally and theoretically confirmed in many materials, formation of triexcitons or larger excitonic complexes is not trivial. Actually hydrogen and positronium do not form three-body bound state, and this is interpreted as the Pauli repulsion prevents an approach of the third particle. Since a theoretical indication by Wang and Kittel for the possible presence of polyexcitons in indirect gap semiconductors [14], the concept of polyexciton have been well accepted while experimental observations have been scarce for four decades. In diamond, next to the observation in silicon [15], an experimental observation of polyexciton PE_n for $n \leq 6$ was reported [17]. However the binding energies of polyexcitonic states have not been investigated so far. There is an exception studying the formation of tetraexcitons where the total wave function is symmetrized [18], and we're considering this treatment will provide incorrect energies.

Thus the presence of polyexciton was not concrete from theoretical aspects. To tackle this problem, we used a numerically efficient basis set called the explicitly correlated Gaussian (ECG) basis. The significant feature of this basis is that all matrix elements of Hamiltonian can be analytically calculated. The variational parameters are optimized by randomly sampling method called the stochastic variational method (SVM). The Hamiltonian of electron-hole few-body system is given by the effective mass theory. The multiple valley and band degrees of freedom are included within a frame work of the $\boldsymbol{k}\cdot\boldsymbol{p}$ perturbation theory. In this framework, electrons and holes are treated as independent particles with unit charge and own effective masses which is determined by the band curvature. We developed a simulation program provided by co-authors in [45], which originally only treats isotropic single band models, to include the anisotropy of effective mass and the multiple valley and band degrees of freedom. As a result, we succeeded in showing the stability of several polyexcitonic states : excitons, trions, biexcitons, charged biexcitons, and triexcitons. Though the charged particles are never observed in diamond, the total binding energy of neutral particles reproduced about 80% of experimentally observed values.

In particular the presence of charged biexcitons and triexcitons are unique in the systems with multiple valley and band degrees of freedom. We also discussed the effect of strong effective mass anisotropy, and revealed that it breaks the degeneracy of polyexcitonic states characterized by different combinations of valley and band degrees of freedom. Due to the different mass anisotropy, the distribution of energy levels has few meV width.

We now emphasize the significance of this work. The calculation of quantum six-body system tends to be regarded as a numerically high costing and hard to implement. However we could show that by appropriate choice of low-costing basis states such calculation can be accomplished within reasonable computational time. This work will serve a fundamental for discussing polyexcitons in more complicated but practically important semiconductors such as silicon, germanium, CuO_2, and TMDs. In theses materials, for example, spin-orbit splitting is not negligible. Explorations of the physics of polyexciton definitely help to understand optical property of materials like the multi-photon emission process, the quantum entanglement between emitted photons, etc. These features are essential for designing optical devices.

In part II we investigated the feasibility of an optical techniques to trap excitonic complexes in solids. This work is stimulated by the recent developments of experimental techniques to manipulate atomic system in vacuum. In the field of optical physics, spatial confinement techniques of quasi particles such as electrons, holes, excitons, and exciton-polaritons have been vigorously explored for experimental realization of BEC. For example, application of the uniaxial strain by 10 μm scale tip on crystal surface produces an effective local potential for carriers. It has been applied in some experiments to observe exciton BEC or exciton-polariton BEC [28,29]. Although many types of methods have been proposed experimentally or theoretically, we proposed to utilize a distinct mechanism from them : inducing optical Stark shift to the inner excitation levels of excitonic particles.

We tackled this problem by using a combination of first principles methods and a model calculation for light-matter coupling. We also chose an excitonic system in graphane, a two-dimensional semiconductor as a model system. Although the utilization of inner excitation levels of excitons are in principle valid in any materials, the graphane has several advantages among possible candidates as a test case. Firstly it has a simple band structure. In graphane a wide direct gap opens at Γ point and there is no complex elements such as the valley degeneracy or large spin-orbit splitting. Secondly excitons in graphane have huge binding energies. This feature is expected to ease difficulties to experimentally identify excitonic levels. The physical origin of this huge binding energy is considered to be due to the weak screening along normal direction to the crystal plane.

According to our GW+BSE calculations the binding energy of the energetically lowest exciton amounts to 1.5eV. We examined the lowest five excitonic levels for building optical potentials by inducing the infrared light whose energy is $\hbar\omega \simeq 500$meV and 660meV. We clarified that two-types of the optical potential can be realized. The energetically lowest excitonic level is doubly degenerate, and the optical potential of the first type traps both levels equally, and the second type traps a selected level by tuning the polarization and incident angle of the laser. The possible potential depth is the order of sub meV when the laser intensity is the order of 10^6 W/cm^2 to 10^7 W/cm^2 which is typical intensity in the experiments of cold atom trapping. When a laser standing wave is induced, the minimum width of optical potential is given by the

half of wave length. In our case, its values are 1.24 μm and 0.94μm for driving lasers having energy $\hbar\omega \simeq 500$meV and 660meV, respectively. This spatial scale is almost 100th part of the tip diameter used to induce strain on crystals [29]. As a summary, this optically driven confinement technique serves a way to confine excitons inside much smaller region than existing methods, and a way to spatially isolate selected excitonic states.

10.2 Future works

Different directions of developments can be proposed for the two studies we did in this thesis. We introduce them in order.

In the study of polyexcitonic state investigation, the most important and natural development is the numerical exploration of polyexcitons bigger than triexcitons. In the experiment reported by Omachi *et al* five peaks are observed and they are interpreted as a signature of a formation of PE_n for $n \leq 6$. To tackle this computationally quite high costing problem, a possible approach is parallelizing our program. However, we can't expect this parallelization greatly enhance the ability to treat bigger systems because the calculation cost quickly increases with the increase of the particle number. One promising solution is constructing the effective interaction potential between excitons. In this case the minimum unit of a system is an exciton, and we just need to solve n-body problem for simulating PE_n, not a $2n$-body problem.

It is also important to improve the physical model to describe excitonic systems. For example, in this study we neglected the spin-orbit splitting and the electron-hole exchange interaction. To discuss polyexcitons in other semiconductor such as silicon, GaAs, Cu_2O, TMD, and so on, these effects are not negligible. In these materials, they have a great significance not only for the matter of quantitative accuracy of the model, but also for describing the correct spin structure of polyexcitons. The spin structure of excitonic particles strongly restricts their ways to decay into photons and/or phonons, e. g. the lifetime of spin-triplet excitons is usually much longer than spin-singlet excitons.

In the study of exploring the application of optical trapping techniques in the excitonic system, the next goal is investigating the feasibility in more complex materials. From a viewpoint of applications, semiconductors such as diamond, GaAs, Cu_2O, TMD are more important than graphane. However, these materials have more complex properties like the large spin-orbit splitting, and the valley degeneracy. Our study in graphane can be a foundation for discussing excitonic systems in these materials.

Next goal is investigating the optical trap of excitonic complexes. As we mentioned so far the presence of polyexcitons have been unclear. This is due to the difficulty to find weak photo-emission peak originating from polyexcitons hidden behind strong spectra of free excitons and the electron-hole liquid. In general we can expect that the inner excitation levels of polyexcitons are different from those of excitons. If one energy level interval of a polyexciton is sufficiently apart from those of free excitons, we can utilize this level for inducing the optical potential which only traps polyexcitons. This technique will contribute to study polyexcitonic many-body properties.

APPENDIX A Physical Quantity of Excitons

A.1 Expectation value of one-body operator

Here we introduce the expectation value of one-body operator $\hat{\mathcal{O}}_1$ of the exciton within the Tamm-Dancoff approximation.

$$\hat{\mathcal{O}}_1 = \int d\boldsymbol{r}\Psi^\dagger(\boldsymbol{r})\hat{O}_1\Psi(\boldsymbol{r}) \tag{A.1}$$

$$|S\rangle = \sum_{\boldsymbol{k}}^{\{\mathrm{BZ}\}}\sum_{i}^{\mathrm{c.b.}}\sum_{j}^{\mathrm{v.b.}} A^S_{\boldsymbol{k}ij}a^\dagger_{\boldsymbol{k}i}a_{\boldsymbol{k}j}|\mathrm{g.s.}\rangle \tag{A.2}$$

Since each exciton state is diagonalized, clearly

$$\langle S'|S\rangle = \sum_{\boldsymbol{k}}^{\{\mathrm{BZ}\}}\sum_{i}^{\mathrm{c.b.}}\sum_{j}^{\mathrm{v.b.}}(A^{S'}_{\boldsymbol{k}ij})^*A^S_{\boldsymbol{k}ij} \tag{A.3}$$

$$= \delta_{S'S}\sum_{\boldsymbol{k}}^{\{\mathrm{BZ}\}}\sum_{i}^{\mathrm{c.b.}}\sum_{j}^{\mathrm{v.b.}}|A^S_{\boldsymbol{k}ij}|^2. \tag{A.4}$$

Then the expectation value is given by:

$$\langle S'|\hat{\mathcal{O}}_1|S\rangle = \langle\mathcal{O}_1\rangle^{\mathrm{e}^-}_{S'S} - \langle\mathcal{O}_1\rangle^{\mathrm{hole}}_{S'S} + \delta_{S'S}\langle\mathcal{O}_1\rangle^{\mathrm{g.s.}}_{SS} \tag{A.5}$$

where

$$\langle\mathcal{O}_1\rangle^{\mathrm{e}^-}_{S'S} = \sum_{\boldsymbol{p}}^{\{\mathrm{BZ}\}}\sum_{n}^{\mathrm{v.b.}}\sum_{m,i}^{\mathrm{c.b.}}(A^{S'}_{\boldsymbol{p}mn})^*A^S_{\boldsymbol{p}in}O_{1,\boldsymbol{p}m\boldsymbol{p}i} \tag{A.6}$$

$$\langle\mathcal{O}_1\rangle^{\mathrm{hole}}_{S'S} = \sum_{\boldsymbol{p}}^{\{\mathrm{BZ}\}}\sum_{m}^{\mathrm{c.b.}}\sum_{n,j}^{\mathrm{v.b.}}(A^{S'}_{\boldsymbol{p}mn})^*A^S_{\boldsymbol{p}mj}O_{1,\boldsymbol{p}j\boldsymbol{p}n} \tag{A.7}$$

$$\langle\mathcal{O}_1\rangle^{\mathrm{g.s.}}_{SS} = \{\sum_{\boldsymbol{k}}^{\{\mathrm{BZ}\}}\sum_{i}^{\mathrm{c.b.}}\sum_{j}^{\mathrm{v.b.}}|A^S_{\boldsymbol{k}ij}|^2\}\sum_{\boldsymbol{q}}^{\{\mathrm{BZ}\}}\sum_{\tau}^{\mathrm{v.b.}}O_{1,\boldsymbol{q}\tau\boldsymbol{q}\tau} \tag{A.8}$$

$$= \langle S|S\rangle\langle\mathrm{g.s.}|\hat{\mathcal{O}}_1|\mathrm{g.s.}\rangle, \tag{A.9}$$

and $O_{1,\boldsymbol{k}i\boldsymbol{q}j} = \int d\boldsymbol{r}\phi^*_{\boldsymbol{k}i}\hat{O}_1\phi_{\boldsymbol{q}j}$. Matrix element between excitonic states and the ground state $|0\rangle$ is much simpler and it is given by:

$$\langle 0|\hat{O}_1|S\rangle = \sum_{k}^{\{\mathrm{BZ}\}}\sum_{i}^{\mathrm{c.b.}}\sum_{j}^{\mathrm{v.b.}}A^S_{\boldsymbol{k}ij}O_{1,\boldsymbol{k}j\boldsymbol{k}i}. \tag{A.10}$$

These quantities are used to derive the exciton-field coupling strength in Sec. A.1.1.

A.1.1 Transition Dipole Moment of Exciton

The evaluation of the exciton transition dipole moment is easy when the plane wave basis set is used. As we can see detailed derivations in Appendix A.1, the expectation value $\boldsymbol{d}_{SS'} = \langle S|e\boldsymbol{r}|S'\rangle$ is given by:

$$\boldsymbol{d}_{SS'} = \langle e\boldsymbol{r}\rangle^{\mathrm{e}^-}_{S'S} - \langle e\boldsymbol{r}\rangle^{\mathrm{hole}}_{S'S} + \delta_{S'S}\langle e\boldsymbol{r}\rangle^{\mathrm{g.s.}}_{SS} \tag{A.11}$$

and

$$\langle e\boldsymbol{r}\rangle_{\boldsymbol{k}i\boldsymbol{k}j} = e\int_{\mathcal{N}\Omega} d\boldsymbol{r}\phi^*_{\boldsymbol{k}i}\boldsymbol{r}\phi_{\boldsymbol{k}j} \tag{A.12}$$

$$= e\lim_{\boldsymbol{q}\to 0}\sum_{\boldsymbol{G},\boldsymbol{G'}}\frac{C^*_{i,k+q,G}C_{j,k,G'}}{i\boldsymbol{q}\mathcal{N}\Omega}\int_{\mathcal{N}\Omega} d\boldsymbol{r}e^{-i(\boldsymbol{k}+\boldsymbol{q}+\boldsymbol{G})\cdot\boldsymbol{r}}(e^{i\boldsymbol{q}\cdot\boldsymbol{r}}-1)e^{i(\boldsymbol{k}+\boldsymbol{G'})\cdot r} \tag{A.13}$$

$$= e\lim_{\boldsymbol{q}\to 0}\sum_{\boldsymbol{G}}\frac{C^*_{i,k+q,G}C_{j,k,G}}{i\boldsymbol{q}}. \tag{A.14}$$

This is quite easy to compute when we use the *quantum-espresso* code.

A.1.2 The Electron-Phonon Interaction

The electron-phonon interaction can be obtained in the framework of the density functional perturbation theory. The electron-phonon interaction by the order of $1/\sqrt{M}$, where M is the total atom mass of an unit cell, is given as follows:

$$V_{phonon} = \sum_{i'i\boldsymbol{q}\lambda}\sqrt{\frac{\hbar}{2M\omega_{\boldsymbol{q}\lambda}}}\langle\phi_{i',k_{i'}}|\nabla_{q\lambda}V^{\mathrm{SCF}}(\boldsymbol{r})|\phi_{i,k_i}\rangle B_{q\lambda}a^\dagger_{i'}a_i \tag{A.15}$$

$$= \sum_{i'i\lambda} g_{i'k_{i'}ik_i\lambda}B_{q\lambda}a^\dagger_{i'}a_i. \tag{A.16}$$

Here $B_{q\lambda} = b^\dagger_{q\lambda} + b_{q\lambda}$ is the phonon creation and annihilation operator. $\omega_{\boldsymbol{q}\lambda}$ is a frequency of phonon of mode λ with wave vector $\boldsymbol{q}$. $g_{i'k_{i'}ik_i\lambda}$ is the coupling strength between electron and phonon. By evaluating the matrix element of $g_{i'k_{i'}ik_i\lambda}$ by two excitonic states with $k\pm q$ and k, we get the exciton-phonon coupling as:

$$G_{k\pm q,k} \simeq \sum_{pcc'v} A^{S*}_{pc'v}A^S_{pcv}g_{c'(p+k\pm q)c(p+k)} - \sum_{pcvv'} A^{S*}_{pcv'}A^S_{pcv}g_{vpv'(p\pm q)}. \tag{A.17}$$

APPENDIX B Symmetry of graphane crystal structure

B.1 Crystal structure of graphane and the symmetry operators of D_{3d} group

When the coordinate vector $\boldsymbol{r}$ is decomposed into a linear combination of unit vectors parallel to lattice vectors as follows:

$$\boldsymbol{r} = m\boldsymbol{e}_1 + n\boldsymbol{e}_1 + p\boldsymbol{e}_3 \equiv (m, n, p), \tag{B.1}$$

the lattice structure of Graphane is unchanged under operations in the list below.

$$\begin{array}{cccccc}
E & C_3^{(z)} & C_3^{(z)2} & C_2^{(1,0)} & C_2^{(01)} & C_2^{(11)} \\
\begin{pmatrix} 1 & 0 & 0 \\ 0 & 1 & 0 \\ 0 & 0 & 1 \end{pmatrix} & \begin{pmatrix} 0 & -1 & 0 \\ 1 & -1 & 0 \\ 0 & 0 & 1 \end{pmatrix} & \begin{pmatrix} -1 & 1 & 0 \\ -1 & 0 & 0 \\ 0 & 0 & 1 \end{pmatrix} & \begin{pmatrix} 1 & -1 & 0 \\ 0 & -1 & 0 \\ 0 & 0 & -1 \end{pmatrix} & \begin{pmatrix} -1 & 0 & 0 \\ -1 & 1 & 0 \\ 0 & 0 & -1 \end{pmatrix} & \begin{pmatrix} 0 & 1 & 0 \\ 1 & 0 & 0 \\ 0 & 0 & -1 \end{pmatrix} \\
i & S_6 & S_6^{-1} & \sigma_d^{(1,-1)} & \sigma_d^{(2,1)} & \sigma_d^{(1,2)} \\
\begin{pmatrix} -1 & 0 & 0 \\ 0 & -1 & 0 \\ 0 & 0 & -1 \end{pmatrix} & \begin{pmatrix} 1 & -1 & 0 \\ 1 & 0 & 0 \\ 0 & 0 & -1 \end{pmatrix} & \begin{pmatrix} 0 & 1 & 0 \\ -1 & 1 & 0 \\ 0 & 0 & -1 \end{pmatrix} & \begin{pmatrix} 0 & -1 & 0 \\ -1 & 0 & 0 \\ 0 & 0 & 1 \end{pmatrix} & \begin{pmatrix} 1 & 0 & 0 \\ 1 & -1 & 0 \\ 0 & 0 & 1 \end{pmatrix} & \begin{pmatrix} -1 & 1 & 0 \\ 0 & 1 & 0 \\ 0 & 0 & 1 \end{pmatrix}
\end{array} \tag{B.2}$$

Here I used the Schoenflies notation. The operation matrix transform the vector $\boldsymbol{r} = (m, n, p)$ as follows:

$$C_3^{(z)}\boldsymbol{r} = \begin{pmatrix} 0 & -1 & 0 \\ 1 & -1 & 0 \\ 0 & 0 & 1 \end{pmatrix} \begin{pmatrix} m \\ n \\ p \end{pmatrix} = \begin{pmatrix} -n \\ m-n \\ p \end{pmatrix}. \tag{B.3}$$

In the Cartesian coordinate, $\boldsymbol{r} = (x, y, z)$, $\boldsymbol{e}_1 = (1/2, 1/\sqrt{3}, 0)$, $\boldsymbol{e}_2 = (1/2, -1/\sqrt{3}, 0)$, $\boldsymbol{e}_3 = (0, 0, 1)$ and

$$m = x + y/\sqrt{3},\ n = x - y/\sqrt{3},\ p = z. \tag{B.4}$$

B.2 The character table of group D_{3d}

The character table of the group D_{3d} is given by as follows:

D_{3d}	E	$2C_3$	$3C_2'$	i	$2S_6$	$3\sigma_d$	$basis$
A_{1g}	1	1	1	1	1	1	$const.$
A_{2g}	1	1	-1	1	1	-1	
E_g	2	-1	0	2	-1	0	(xz, yz) .
A_{1u}	1	1	1	-1	-1	-1	
A_{2u}	1	1	-1	-1	-1	1	z
E_u	2	-1	0	-2	1	0	(x, y)

(B.5)

B.3 Representations of D_{3d} group and matrix elements of dipole moment

To discuss the possible coupling between basis it is convenient to see how a direct product of basis is decomposed into a linear combination of new basis. It can be derived by calculating products of character $\chi^i(R)$ for each element of the group R:

$$\chi^i(R)\chi^j(R) = \sum_k C_{ijk}\chi^k(R). \tag{B.6}$$

The way of decomposition is unique. The dipole moment between excitonic states are given by evaluating an operator $e\boldsymbol{r}$ and among components of $\boldsymbol{r}$, (x, y) and z belong to E_u and A_{2u} representation respectively. According to Eq. (B.6) we obtain a result as in Table (B.7).

	A_{1g}	A_{2g}	E_g	A_{1u}	A_{2u}	E_u
E_u	E_u	E_u	$A_{1u} + A_{2u} + E_u$	E_g	E_g	$A_{1g} + A_{2g} + E_g$
A_{2u}	A_{2u}	A_{1u}	E_u	A_{2g}	A_{1g}	E_g

(B.7)

Thus, if an excitonic state belongs to E_u representation it can be coupled with states belong to A_{1g}, A_{2g} and E_g representations.

APPENDIX C Hamiltonian matrix elements evaluated by the CG basis set

C.1 Matrix elements of Hamiltonian

Here we give the matrix elements of the Gram matrix and the Hamiltonian with multiple valley and band in anisotropic systems. The details of derivations of the matrix elements for isotropic systems are in the text book of Suzuki and Varga [27]. The book does not treat anisotropic systems, but the derivations described there can be generalized to anisotropic systems as follows. We assume the following type of basis.

$$|LM, \boldsymbol{v}, A\rangle = f_{LM}(\boldsymbol{r}) \cdot \chi_{sm_s} \cdot \prod_{i=1}^{N_e} |\Delta_i\rangle \prod_{i=1}^{N_h} |\Gamma_i\rangle \tag{C.1}$$

The envelope function $f_{LM}(\boldsymbol{r})$ is given by a product of a solid spherical harmonic, a Gaussian, and a plane wave part.

$$f_{LM}(\boldsymbol{r}) = |\boldsymbol{v}|^L Y_{LM}(\hat{\boldsymbol{v}}) \cdot \exp\{-\frac{1}{2}\mathrm{xAx}\} \tag{C.2}$$

The matrix elements of the Gram matrix is given by

$$\begin{aligned}
&\langle L'M', \boldsymbol{v}', A'|LM, \boldsymbol{v}, A\rangle \\
&= \frac{(2L+1)!!}{4\pi} \left\{ \frac{(2\pi)^{N-1}}{\det B} \right\}^{\frac{3}{2}} \rho^L \delta_{L'L} \delta_{M'M} \langle \chi_{s'm'}|\chi_{sm}\rangle \prod_i^{N_e} \delta_{\Delta'_i,\Delta_i} \prod_i^{N_h} \delta_{\Gamma'_i,\Gamma_i},
\end{aligned} \tag{C.3}$$

$$\rho = \sum_{i,j}^{N-1} u'_i (B^{-1})_{ij} u_j \tag{C.4}$$

where $B = A' + A$ and u_i is a coefficient of the global vector $\boldsymbol{v} = \sum_i^{N-1} u_i \mathrm{x}_i$. Next, we give matrix elements of the anisotropic kinetic energy of the electron:

$$\begin{aligned}
&\langle L'M', \boldsymbol{v}', A'| \sum_{i=1}^{N_e} \sum_{\gamma} t_{e,i}^{(\gamma)} \cdot \hat{\tau}_{\gamma\gamma,i} |LM, \boldsymbol{v}, A\rangle \\
&= \frac{1}{2} (B_{0L} B_{0L'})^{-1} \left\{ \frac{(2\pi)}{\det B} \right\}^{\frac{3}{2}} L!L'! \\
&\times \{ g_1(L, M, L', M', R_x, R_y, R_z) + g_2(L, M, L', M', P_x, P_y, P_z) \\
&+ g_2(L', M', L, M, P'_x, P'_y, P'_z) + g_3(L, M, L', M', Q_x, Q_y, Q_z) \} \langle \chi_{s'm'}|\chi_{sm}\rangle,
\end{aligned} \tag{C.5}$$

$$B_{nl} = \frac{4\pi(2n+l)!}{2^n n!(2n+2l+1)!!}. \tag{C.6}$$

The functions $g_1, g_2, and g_3$ are defined as follows:

$$g_1(L,M,L',M',R_x,R_y,R_z) = \frac{1}{L!}(\sum_{\mu=x,y,x} R_\mu)\rho^L B_{0L}\delta_{LL'}\delta_{MM'}, \tag{C.7}$$

$$R_\mu = \mathrm{Tr}\{A'\Lambda_\mu A B^{-1}\} \tag{C.8}$$

$$\Lambda_{\mu,jk} = \prod_{i=1}\delta_{\Delta_i'\Delta_i}\sum_{i=1}\frac{1}{m_{i,\mu}^{(\Delta_i)}}U_{ji}U_{ki}, \tag{C.9}$$

$$\begin{aligned}
&g_2(L,M,L',M',P_x,P_y,P_z)\\
&=\{\frac{1}{3c_{20}}\left(P_z-\frac{P_x+P_y}{2}\right)C_{20,LM}^{L'M}\delta_{MM'}+\frac{1}{4c_{22}}(P_x-P_y)(C_{2-2,LM}^{L'M-2}\delta_{M'M-2}+C_{22,LM}^{L'M+2}\delta_{M'M+2})\}\\
&\times B_{0L}D_{2LL'}\frac{1}{L'!}\rho^{L'}\delta_{L'L-2},
\end{aligned} \tag{C.10}$$

$$P_\mu = -\sum_{ij}^{N_{all}-1} u_i\{B^{-1}A'\Lambda_\mu A'B^{-1}\}_{ij}u_j, \tag{C.11}$$

$$P'_\mu = -\sum_{ij}^{N_{all}-1} u'_i\{B^{-1}A\Lambda_\mu AB^{-1}\}_{ij}u'_j. \tag{C.12}$$

Here, $C_{l_1m_1,l_2m_2}^{l_3m_3}$ is a Clebsch-Gordan coefficient, $N_{all} = N_e + N_h$, and

$$c_{20} = \frac{1}{4}\left(\frac{5}{\pi}\right)^{1/2},\ c_{22} = \frac{1}{4}\left(\frac{15}{2\pi}\right)^{1/2},\ D_{l_3l_1l_2} = \left\{\frac{(2l_1+1)(2l_2+1)}{4\pi(2l_3+1)}\right\}^{1/2}C_{l_10l_20}^{l_30}, \tag{C.13}$$

$$\begin{aligned}
&g_3(L,M,L',M',Q_x,Q_y,Q_z)\\
&=\frac{1}{c_{10}^2}\{(Q_x-Q_y)[C_{LM,1-1}^{L-1M-1}C_{L-1M'+1,1-1}^{LM'}\delta_{M-1M'+1}+C_{LM,1+1}^{L-1M+1}C_{L-1M'-1,1+1}^{LM'}\delta_{M+1M'-1}]\\
&-(Q_x+Q_y)[C_{LM,1-1}^{L-1,M-1}C_{L-1M'-1,1+1}^{LM'}+C_{LM,1+1}^{L-1M+1}C_{L-1M'+1,1-1}^{LM'}]\delta_{MM'}\\
&+2Q_zC_{LM,10}^{L-1M}C_{L-1M',10}^{LM'}\delta_{MM'}\}D_{L-1L1}D_{LL-11}\delta_{LL'}B_{0L-1}\rho^{L-1},
\end{aligned} \tag{C.14}$$

$$Q_\mu = 2\sum_{ij}^{N_{all}-1} u'_i\{B^{-1}A\Lambda_\mu A'B^{-1}\}_{ij}u_j,\ c_{10} = \left(\frac{3}{2\pi}\right)^{1/2}. \tag{C.15}$$

These expressions are applied to the matrix elements of hole kinetic energy. Next we give the matrix elements of inter-band coupling.

$$\begin{aligned}
&\langle L'M',\boldsymbol{v}',A'|\sum_{i=1}^{N_h}t_{h,i}^{(\Gamma_{xy}\Gamma_{yz})}\cdot\hat{\tau}_{\Gamma_{xy}\Gamma_{yz},i}|LM,\boldsymbol{v},A\rangle\\
&=(B_{0L'}B_{0L})^{-1}L'!L!\left\{\frac{(2\pi)^{N-1}}{\det B}\right\}\{h_{1,xz}(L,M,L',M',S_{xz})\\
&+h_{1,xz}(L',M',L,M,S'_{xz})+h_{2,xz}(L,M,L',M',T_{xz})\}\langle\chi_{s'm'}|\chi_{sm}\rangle,
\end{aligned} \tag{C.16}$$

$$
\begin{aligned}
&h_{1,xz}(L,M,L',M',S_{xz})\\
&=\frac{S_{xz}}{4c_{22}}D_{L2L'}(C^{L'M-1}_{LM,2-1}\delta_{M',M-1}-C^{L'M+1}_{LM,21}\delta_{M',M+1})B'_{0L}\frac{1}{L'!}\rho^{L'}\delta_{L',L-2},
\end{aligned}
\tag{C.17}
$$

$$
\begin{aligned}
&h_{2,xz}(L,M,L',M',T_{xz})\\
&=-\frac{T_{xz}}{2^{3/2}c_{11}^2}D_{L-1,1,L}D_{L,1,L-1}B_{0L-1}\frac{1}{(L-1)!}\rho^{L-1}\delta_{L'L}\\
&\times\{C^{L-1M}_{LM,10}(C^{LM'}_{L-1M,1-1}\delta_{M'M-1}-C^{LM'}_{L-1M,11}\delta_{M'M+1})\\
&+C^{LM'}_{L-1M',10}(C^{L-1M'}_{LM,1-1}\delta_{M'M-1}-C^{L-1M'}_{LM,11}\delta_{M'M+1})\},
\end{aligned}
\tag{C.18}
$$

$$
\begin{aligned}
&\langle L'M',\boldsymbol{v}',A'|\sum_{i=1}^{N_h}t_{h,i}^{(\Gamma_{yz}\Gamma_{zx})}\cdot\hat{\tau}_{\Gamma_{yz}\Gamma_{zx},i}|LM,\boldsymbol{v},A\rangle\\
&=i(B_{0L'}B_{0L})^{-1}L'!L!\left\{\frac{(2\pi)^{N-1}}{\det B}\right\}\{h_{1,xy}(L,M,L',M',S_{xy})\\
&+h_{1,xy}(L',M',L,M,S'_{xy})+h_{2,xy}(L,M,L',M',T_{xy})\}\langle\chi_{s'm'}|\chi_{sm}\rangle,
\end{aligned}
\tag{C.19}
$$

$$
\begin{aligned}
&h_{1,xy}(L,M,L',M',S_{xy})\\
&=\frac{S_{xy}}{4c_{22}}D_{L2L'}(C^{L'M-2}_{LM,2-2}\delta_{M',M-2}-C^{L'M+2}_{LM,22}\delta_{M',M+2})B'_{0L}\frac{1}{L'!}\rho^{L'}\delta_{L',L-2},
\end{aligned}
\tag{C.20}
$$

$$
\begin{aligned}
&h_{2,xy}(L,M,L',M',T_{xy})\\
&=-\frac{T_{xy}}{2c_{11}^2}D_{L-1,1,L}D_{L,1,L-1}B_{0L-1}\frac{1}{(L-1)!}\rho^{L-1}\delta_{L'L}\\
&\times(C^{L-1M-1}_{LM,1-1}C^{L'M'}_{L-1M'+1,1-1}\delta_{M'+1M-1}-C^{L-1M+1}_{LM,11}C^{L'M'}_{L-1M'-1,11}\delta_{M'-1M+1}),
\end{aligned}
\tag{C.21}
$$

$$
\begin{aligned}
&\langle L'M',\boldsymbol{v}',A'|\sum_{i=1}^{N_h}t_{h,i}^{(\Gamma_{zx}\Gamma_{xy})}\cdot\hat{\tau}_{\Gamma_{zx}\Gamma_{xy},i}|LM,\boldsymbol{v},A\rangle\\
&=i(B_{0L'}B_{0L})^{-1}L'!L!\left\{\frac{(2\pi)^{N-1}}{\det B}\right\}\{h_{1,yz}(L,M,L',M',S_{yz})\\
&+h_{1,yz}(L',M',L,M,S'_{yz})+h_{2,yz}(L,M,L',M',T_{yz})\}\langle\chi_{s'm'}|\chi_{sm}\rangle,
\end{aligned}
\tag{C.22}
$$

$$
\begin{aligned}
&h_{1,yz}(L,M,L',M',S_{xz})\\
&=\frac{S_{yz}}{4c_{22}}D_{L2L'}(C^{L'M-1}_{LM,2-1}\delta_{M',M-1}+C^{L'M+1}_{LM,21}\delta_{M',M+1})B'_{0L}\frac{1}{L'!}\rho^{L'}\delta_{L',L-2},
\end{aligned}
\tag{C.23}
$$

$$
\begin{aligned}
&h_{2,yz}(L,M,L',M',T_{xz}) \\
&= -\frac{T_{yz}}{2^{3/2}c_{11}^2} D_{L-1,1,L} D_{L,1,L-1} B_{0L-1} \frac{1}{(L-1)!} \rho^{L-1} \delta_{L'L} \\
&\times \{ C_{LM,10}^{L-1M} (C_{L-1M,1-1}^{LM'} \delta_{M'M-1} + C_{L-1M,11}^{LM'} \delta_{M'M+1}) \\
&+ C_{L-1M',10}^{LM'} (C_{LM,1-1}^{L-1M'} \delta_{M'M-1} + C_{LM,11}^{L-1M'} \delta_{M'M+1}) \}.
\end{aligned}
\tag{C.24}
$$

Here,

$$
S_\mu = -\sum_{i,j} u_i \{B^{-1} A' Z_\mu A' B^{-1}\}_{ij} u_j \tag{C.25}
$$

$$
S'_\mu = -\sum_{i,j} u'_i \{B^{-1} A Z_\mu A B^{-1}\}_{ij} u'_j \tag{C.26}
$$

$$
T_\mu = \sum_{i,j} u_i \{B^{-1} A' Z_\mu A B^{-1}\}_{ij} u'_j, \tag{C.27}
$$

where, *e.g.* for $\mu = xy$,

$$
Z_{xy,jk} = -N \sum_{i=1}^{N_h} U_{ji} U_{ki} \delta_{\Gamma_{yz}\Gamma'_i} \delta_{\Gamma'_i \Gamma'_{zx}} \prod_{j \neq i}^{N_h} \delta_{\Gamma'_j \Gamma_j} \tag{C.28}
$$

and $c_{11} = c_{10}/2$. Finally, we show the matrix elements of the Coulomb potential:

$$
\begin{aligned}
&\langle L'M', \boldsymbol{v}', A' | \frac{1}{r_{ij}} | LM, \boldsymbol{v}, A \rangle \\
&= \langle L'M', \boldsymbol{v}', A' | LM, \boldsymbol{v}, A \rangle \sum_{n=0}^{L} \frac{L!}{(L-n)!} \left(\frac{\sigma\sigma'}{c\rho} \right)^n \sqrt{\frac{2c}{\pi}} \frac{(-1)^n}{(2n+1)n!},
\end{aligned}
\tag{C.29}
$$

where

$$
c^{-1} = \sum_{k,l} w_k^{(ij)} \{B^{-1}\}_{kl} w_l^{(ij)}, \tag{C.30}
$$

$$
\sigma = c \sum_{k,l} w_k^{(ij)} \{B^{-1}\}_{kl} u_l, \tag{C.31}
$$

$$
\sigma' = c \sum_{k,l} w_k^{(ij)} \{B^{-1}\}_{kl} u'_l, \tag{C.32}
$$

$$
w_k^{(ij)} = \{U^{-1}\}_{ik} - \{U^{-1}\}_{jk}. \tag{C.33}
$$

C.2 Intervalley Coulomb Interaction

In this section we estimate the magnitude of intervalley Coulomb interaction with an approximate model. The analytical form of the matrix element of direct inter-valley Coulomb interaction is given by

$$
V_{pp'kk'} = C \int d\boldsymbol{r}^N |f(\{\boldsymbol{r}\})|^2 \frac{1}{\epsilon r} e^{i\boldsymbol{p}\cdot\boldsymbol{r_1} + i\boldsymbol{p'}\cdot\boldsymbol{r_2} - i\boldsymbol{k'}\cdot\boldsymbol{r_2} - i\boldsymbol{k}\cdot\boldsymbol{r_1}},
\tag{C.34}
$$

where C is a normalization constant. $\boldsymbol{r}_1$, $\boldsymbol{r}_2$ are the one-particle coordinates of electrons, and $r = |\boldsymbol{r}_1 - \boldsymbol{r}_2|$. p, p', k, and k' are the valley wave vector of electrons. According to a previous numerical simulation of biexciton with isotropic effective masses [2], the mean distance between the electrons $\langle r_{e^-e^-} \rangle$ is $\langle r_{e^-e^-} \rangle \simeq 4.5 a_{\mathrm{ex}}$, where $a_{\mathrm{ex}} = 31.1[a_{\mathrm{B}}]$ is the exciton Bohr radius (a_{B} is the Hydrogen Bohr radius), in the case of diamond. Assuming that the cell-periodic part of the Bloch function and the envelope function to be unity and a simple exponential form with the decaying length $\langle r_{e^-e^-} \rangle = 4.5 a_{\mathrm{ex}}$, respectively, the inter-valley matrix element of the direct Coulomb interaction can be approximated as

$$\begin{aligned} V_{pp'kk'} \quad &\sim C \int d\boldsymbol{r}_1 d\boldsymbol{r}_2 \frac{1}{\epsilon r} e^{-2r/(3a_{ex})} \\ &\times e^{i\boldsymbol{p}\cdot\boldsymbol{r_1} + i\boldsymbol{p'}\cdot\boldsymbol{r_2} - i\boldsymbol{k'}\cdot\boldsymbol{r_2} - i\boldsymbol{k}\cdot\boldsymbol{r_1}}, \end{aligned} \tag{C.35}$$

Here we neglected the spatial correlation between electrons and holes. This matrix element can be calculated analytically and we get to

$$V_{pp'kk'} = \frac{4}{\epsilon (3a_{ex})^2} \frac{\delta(\boldsymbol{k} + \boldsymbol{k'} - \boldsymbol{p'} - \boldsymbol{p})}{(2/(3a_{ex}))^2 + \Delta k^2}, \tag{C.36}$$

where $\Delta k = |\boldsymbol{k} - \boldsymbol{p}|$. When $\Delta k = 0$, this is a direct Coulomb interaction. Provided that $\boldsymbol{k} = (k_c, 0, 0)$ and $\boldsymbol{p} = (0, k_c, 0)$ ($k_c = 0.76\overline{\Gamma \mathrm{X}} = 0.76/6.74$ $[a_{\mathrm{B}}^{-1}]$), we obtain $V_{pp'kk'} = 0.90$[meV]. This value amounts to 1.77% of the direct Coulomb interaction. This smallness is thanks to the large exciton Bohr radius and large wave vector across the valleys. Here we used the geometric mean of anisotropic effective mass to derive the exciton Bohr radius. This is comparable with other effects neglected in our approximation.

APPENDIX D Energy of Polyexcitons

Here we show the value of the total binding energy E_{PE_n} and separation energy S_{PE_n} for every possible inequivalent bound state. The columns "electron" and "hole" show the subscript of the valley or band. $\pm k_z$ means the valley on $\pm k_z$ axis and yz means the Γ_{yz} band, for instance. There are 6 valleys ($\Delta(\pm k_c 00)$, $\Delta(0 \pm k_c 0)$, $\Delta(00 \pm k_c)$) and 3 bands (Γ_{yz}, Γ_{zx}, Γ_{xy}) in diamond. We regard two combinations as equivalent if they can be transformed into each other by rotation and inversion. The factor g is the degeneracy of each state. Q is the absolute value of the total momentum.

We also show the group theoretical classification of the states based on the factor group of Hamiltonian. It depends on the combination of valleys and bands as we ignored inter-valley(band) coupling. The Q is kept unchanged even if we include the inter-valley(band) coupling, but the group theoretical classification is not. We hence show only for simple cases like exciton and trion$^{\pm}$. The columns "group" and "rep." stand for the group of the block diagonalized Hamiltonian and the representation the state belongs to, respectively. The name of representations are taken from the textbook [25], and have no information on the points on Brillouin zone.

Here we show an example to derive such classifications. Let us consider the exciton ($\Delta_{00k_c}/\Gamma_{xy}$): the Hamiltonian is

$$H = t_e^{(\Delta_{00k_c})} |\Delta_{00k_c}\rangle\langle\Delta_{00k_c}| + t_h^{(\Gamma_{xy})} |\Gamma_{xy}\rangle\langle\Gamma_{xy}| + V_{\mathrm{Coulomb}}. \tag{D.1}$$

This Hamiltonian has a symmetry of the group C_{4v}. The total wave function is a product of the envelope function and Bloch functions (Δ_{00k_c}, Γ_{xy}). The envelope function is set as scalar under the group operations through our calculations. Δ_{00k_c} and Γ_{xy} transform as Δ_1 and $\Delta_{2'}$, respectively. The total wave function hence belongs to $\Delta_{2'}$ representation of C_{4v} group.

Exciton

electron	hole	E_{PE_n}[meV]	S_{PE_n}[meV]	g	Q	group	rep.
k_z	xy	-7.181×10^1	-	6	k_c	C_{4v}	$\Delta_{2'}$
k_z	yz	-6.774×10^1	-	12	k_c	C_{2v}	Σ_3
Average		-6.909×10^1	-				

Trion$^+$

electron	hole		E_{PE_n}[meV]	S_{PE_n}[meV]	g	Q	group	rep.
k_z	yz	yz	7.113×10^1	3.39	12	k_c	C_{2v}	Σ_1

k_z	yz	xy	7.345×10^1	1.64	12	k_c	C_{2v}	Σ_4
k_z	yz	zx	7.110×10^1	3.36	6	k_c	C_{4v}	$\Delta_{2'}$
k_z	xy	xy	7.505×10^1	3.24	6	k_c	C_{4v}	Δ_1
Average			7.255×10^1	2.78				

Trion$^-$

electron		hole	E_{PE_n}[meV]	S_{PE_n}[meV]	g	Q	group	rep.
k_z	k_z	yz	7.138×10^1	4.09	12	$2k_c$	C_{2v}	Σ_3
k_z	k_z	xy	7.564×10^1	3.83	6	$2k_c$	C_{4v}	$\Delta_{2'}$
k_z	$-k_z$	yz	7.183×10^1	4.09	6	0	D_{2h}	N_2
k_z	$-k_z$	xy	7.564×10^1	3.83	3	0	D_{4h}	X_3
k_z	k_y	yz	7.158×10^1	3.84	12	$\sqrt{2}k_c$	C_{2v}	Σ_1
k_z	k_y	xy	7.386×10^1	2.05	24	$\sqrt{2}k_c$	C_{1h}	U_1
Average			7.310×10^1	3.23				

Biexciton

electron		hole		E_{PE_n}[meV]	S_{PE_n}[meV]	g	Q
k_z	k_z	yz	yz	1.412×10^2	5.73	12	$2k_c$
k_z	k_z	yz	zx	1.409×10^2	5.40	6	$2k_c$
k_z	k_z	yz	xy	1.446×10^2	5.04	12	$2k_c$
k_z	k_z	xy	xy	1.482×10^2	4.60	6	$2k_c$
k_z	$-k_z$	yz	yz	1.410×10^2	5.49	6	0
k_z	$-k_z$	yz	zx	1.411×10^2	5.59	3	0
k_z	$-k_z$	yz	xy	1.446×10^2	5.01	6	0
k_z	$-k_z$	xy	xy	1.479×10^2	4.24	3	0
k_z	k_y	yz	yz	1.407×10^2	5.20	12	$\sqrt{2}k_c$
k_z	k_y	yz	zx	1.427×10^2	3.13	24	$\sqrt{2}k_c$
k_z	k_y	xy	xy	1.443×10^2	4.74	24	$\sqrt{2}k_c$
k_z	k_y	xy	zx	1.450×10^2	1.40	12	$\sqrt{2}k_c$
Average				1.433×10^2	4.36		

CBE$^+$

electron		hole			E_{PE_n}[meV]	S_{PE_n}[meV]	g	Q
k_z	k_z	yz	yz	yz	unbound	-	-	
k_z	k_z	yz	yz	zx	1.521×10^2	1.09×10^1	12	$2k_c$
k_z	k_z	yz	yz	xy	1.534×10^2	8.77	12	$2k_c$
k_z	k_z	yz	zx	xy	1.537×10^2	9.07	6	$2k_c$
k_z	k_z	yz	xy	xy	1.551×10^2	6.86	12	$2k_c$
k_z	k_z	xy	xy	xy	unbound	-	-	

k_z	$-k_z$	yz	yz	yz	unbound	-	-	
k_z	$-k_z$	yz	yz	zx	1.516×10^2	1.06×10^1	6	0
k_z	$-k_z$	yz	yz	xy	1.539×10^2	9.30	6	0
k_z	$-k_z$	yz	zx	xy	1.540×10^2	9.44	3	0
k_z	$-k_z$	yz	xy	xy	1.555×10^2	7.62×10^1	6	0
k_z	$-k_z$	xy	xy	xy	unbound	-	-	
k_z	k_y	yz	yz	yz	unbound	-	-	
k_z	k_y	yz	yz	zx	1.523×10^2	9.61	24	$\sqrt{2}k_c$
k_z	k_y	yz	zx	zx	1.533×10^2	8.97	24	$\sqrt{2}k_c$
k_z	k_y	yz	zx	xy	1.539×10^2	8.85	12	$\sqrt{2}k_c$
k_z	k_y	xy	xy	zx	1.546×10^2	9.60	24	$\sqrt{2}k_c$
k_z	k_y	xy	xy	xy	unbound	-	-	
Average					1.535×10^2	9.31		

CBE$^-$

electron			hole		E_{PE_n}[meV]	S_{PE_n}[meV]	g	Q
k_z	k_z	k_z	yz	yz	unbound	-	-	
k_z	k_z	k_y	yz	yz	1.513×10^2	1.01×10^1	24	$\sqrt{5}k_c$
k_z	k_z	k_x	yz	yz	1.537×10^2	9.11	24	$\sqrt{5}k_c$
k_z	k_z	$-k_z$	yz	yz	1.524×10^2	1.11×10^1	12	k_c
k_z	k_z	k_z	yz	zx	unbound	-	-	
k_z	k_z	k_x	yz	zx	1.527×10^2	1.18×10^1	12	$\sqrt{5}k_c$
k_z	k_z	$-k_z$	yz	zx	1.518×10^2	1.07×10^2	6	k_c
k_z	k_z	k_z	yz	xy	unbound	-	-	
k_z	k_z	$-k_z$	yz	xy	1.547×10^2	1.01×10^2	12	k_c
k_z	k_z	k_x	yz	xy	1.549×10^2	9.91	24	$\sqrt{5}k_c$
k_z	k_z	k_y	yz	xy	1.538×10^2	9.18	24	$\sqrt{5}k_c$
k_z	k_z	k_z	xy	xy	unbound	-	-	
k_z	k_z	$-k_z$	xy	xy	1.587×10^2	1.05×10^1	6	k_c
k_z	k_z	k_x	xy	xy	1.552×10^2	6.98	24	$\sqrt{5}k_c$
k_z	$-k_z$	k_x	yz	yz	1.540×10^2	9.46	12	k_c
k_z	$-k_z$	k_y	yz	yz	1.516×10^2	1.07×10^1	12	k_c
k_z	$-k_z$	k_x	yz	zx	1.530×10^2	1.03×10^1	12	k_c
k_z	$-k_z$	k_x	yz	xy	1.554×10^2	1.04×10^1	12	k_c
k_z	$-k_z$	k_x	xy	xy	1.559×10^2	7.70	12	k_c
k_z	k_y	$-k_y$	yz	zx	1.540×10^2	9.49	12	k_c
k_z	k_y	k_x	xy	xy	1.539×10^2	9.57	24	$\sqrt{3}k_c$
k_z	k_y	k_x	xy	zx	1.540×10^2	9.00	48	$\sqrt{3}k_c$
Average					1.539×10^2	9.51		

Triexciton

electron			hole			E_{PE_n}[meV]	S_{PE_n}[meV]	g	Q
k_z	k_z	k_z	yz	yz	yz	unbound	-	-	
k_z	k_z	k_z	yz	yz	zx	unbound	-	-	
k_z	k_z	k_z	yz	yz	xy	unbound	-	-	
k_z	k_z	k_y	yz	yz	yz	unbound	-	-	
k_z	k_z	k_y	yz	yz	zx	2.229×10^2	9.91	24	$\sqrt{5}k_c$
k_z	k_z	k_y	yz	yz	xy	2.238×10^2	1.13×10^1	24	$\sqrt{5}k_c$
k_z	k_z	k_x	zy	yz	yz	unbound	-	-	
k_z	k_z	k_x	yz	yz	zx	2.259×10^2	1.32×10^1	24	$\sqrt{5}k_c$
k_z	k_z	k_x	yz	yz	xy	2.278×10^2	1.14×10^1	24	$\sqrt{5}k_c$
k_z	k_z	$-k_z$	yz	yz	yz	unbound	-	-	
k_z	k_z	$-k_z$	yz	yz	zx	2.223×10^2	1.34×10^1	12	k_c
k_z	k_z	$-k_z$	yz	yz	xy	2.249×10^2	1.19×10^1	12	k_c
k_z	k_z	k_z	zy	zx	yz	unbound	-	-	
k_z	k_z	k_z	yz	zx	xy	unbound	-	-	
k_z	k_z	$-k_z$	yz	zx	xy	2.249×10^2	1.20×10^1	6	k_c
k_z	k_z	k_z	yz	xy	xy	unbound	-	-	
k_z	k_z	$-k_z$	yz	xy	xy	2.292×10^2	1.28×10^1	12	k_c
k_z	k_z	k_x	yz	xy	xy	2.266×10^2	6.56	24	$\sqrt{5}k_c$
k_z	k_z	k_y	yz	xy	zx	2.254×10^2	9.01	24	$\sqrt{5}k_c$
k_z	k_z	k_z	xy	xy	yx	unbound	-	-	
k_z	k_z	$-k_z$	xy	xy	xy	unbound	-	-	
k_z	k_z	k_x	xy	xy	zx	2.256×10^2	9.66	24	$\sqrt{5}k_c$
k_z	k_z	k_x	xy	xy	xy	unbound	-	-	
k_z	$-k_z$	k_x	yz	yz	yz	unbound	-	-	
k_z	$-k_z$	k_x	yz	yz	zx	2.245×10^2	1.17×10^1	12	k_c
k_z	$-k_z$	k_x	yz	yz	xy	2.265×10^2	1.02×10^1	12	k_c
k_z	$-k_z$	k_y	yz	yz	yz	unbound	-	-	
k_z	$-k_z$	k_y	yz	yz	zx	2.237×10^2	1.09×10^1	12	k_c
k_z	$-k_z$	k_y	yz	yz	xy	2.243×10^2	1.18×10^1	12	k_c
k_z	$-k_z$	k_x	yz	zx	xy	2.257×10^2	9.33	12	k_c
k_z	$-k_z$	k_x	yz	xy	xy	2.275×10^2	7.87	12	k_c
k_z	$-k_z$	k_x	xy	xy	zx	2.265×10^2	1.09×10^1	12	k_c
k_z	$-k_z$	k_x	xy	xy	xy	unbound	-	-	
k_z	k_y	k_x	xy	xy	xy	unbound	-	-	
k_z	k_y	k_x	xy	xy	yz	2.246×10^2	8.55	48	$\sqrt{5}k_c$
k_z	k_y	k_x	xy	zx	yz	2.255×10^2	8.62	8	$\sqrt{5}k_c$
Average						2.253×10^2	1.02×10^1		

REFERENCE

[1] M. Nagai, R. Shimano, K. Horiuchi, and M. Kuwata-Gonokami. *Phys. Stat. Sol. (b)*, **238**, 509, 2003.

[2] J. Usukura, Y. Suzuki, and K. Varga. *Phys. Rev. B*, **59**, 5652, 1999.

[3] D. W. Kidd, D. K. Zhang, and K. Varga. *Phys. Rev. B*, **93**, 125423, 2016.

[4] M. Zieliński, M. Korkusiński, and P. Hawrylak. *Phys. Rev. B*, **81**, 085301, 2010.

[5] L. M. Smith and J. P. Wolfe. *Phys. Rev. B*, **51**, 7521, 1995.

[6] K. Matsuda. *J. Phys. Soc. Japan*, **84**, 121009, 2015.

[7] K. F. Mak, K. He, C. Lee, G. H. Lee, J. Hone, and T. F. Heinz. *Nat. Mat.*, **12**, 207, 2013.

[8] E. J. Sie, A. J. Frenzel, Y. Lee, J. Kong, and N. Gedik. *Phys. Rev. B*, **92**, 125417, 2015.

[9] Y. You, X. Zhang, T. C. Berkelbach, M. S. Hybertsen, D. R. Reichman, and T. F. Heinz. *Nat. Phys.*, **11**, 477, 2015.

[10] G. Plechinger, P. Nagler, J. Kraus, N. Paradiso, C. Strunk, and C. Schüller. *Phys. Stat. Solidi RRL*, **9**, 457, 2015.

[11] M. Ikezawa, Y. Masumoto, T. Takagahara, and S. V. Nair. *Phys. Rev. Lett.*, **79**, 3522, 1997.

[12] S. Bubin, O. V. Prezhdo, and K. Varga. *Phys. Rev. A*, **87**, 054501, 2013.

[13] G. Calzaferri. *Chem. Phys. Lett.*, **87**, 443, 1982.

[14] J. Shy-Yih Wang and C. Kittel. *Phys. Lett.*, **42**A, 189, 1972.

[15] A. G. Steele, W. G. McMullan, and M. L. W. Thewalt. *Phys. Rev. Lett.*, **59**, 2899, 1987.

[16] L. M. Smith and J. P. Wolfe. *Phys. Rev. Lett.*, **58**, 2823, 1987.

[17] J. Omachi, T. Suzuki, K. Kato, N. Naka, K. Yoshioka, and M. Kuwata-Gonokami. *Phys. Rev. Lett.*, **111**, 026402, 2013.

[18] A. C. Cancio and Y. Chang. *Phys. Rev. B*, **42**, 11317, 1990.

[19] L. Hedin. *Phys. Rev.*, **139**, 3A, 1965.

[20] M. S. Hybertsen and S. G. Louie. *Phys. Rev. B*, **34**, 8, 1986.

[21] M. Rohlfing and S. G. Louie. *Phys. Rev. B*, **62**, 8, 2000.

[22] P. Giannozzi et al. *J. Phys.: Condens. Matter*, **21**, 395502, 2009.

[23] J. Deslippe, G. Samsonidze, D. A. Strubbe, M. Jain, M. L. Cohen, and S. G. Louie. *Comp. Phys. Comm.*, **183**, 1269, 2012.

[24] J. M. Luttinger and W. Kohn. *Phys. Rev.*, **97**, 4, 1954.

[25] M. S. Dresselhaus, G. Dresselhaus, and A. Jorio. Group theory. *Springer, Heidelberg*, 2008.

[26] H. M. James and A. S. Coolidge. *J. Chem. Phys.*, **1**, 825, 1933.

[27] Y. Suzuki and K. Varga. Stochastic variational approach to quantum-mechanical few-body problems. *Springer, Heidelberg*, 1998.

[28] R. Balili, V. Hartwell, D. Snoke, L. Pfeiffer, and K. West. *Science*, **316**,1007, 2007.

[29] K. Yoshioka, E. Chae, and M. Kuwata-Gonokami. *Nat. Comm.*, DoI: 10.1038/ncomms1335.

[30] C. W. Lai, N. Y. Kim, S. Utsunomiya, G. Roumposand H. Deng, M. D. Fraser, T. Byrnes, P. Recher, N. Kumada, T. Fujisawa, and Y. Yamamoto. *Nature*, **450**, 529, 2007.

[31] A. T. Hammack, M. Griswold, L. V. Butov, L. E. Smallwood, A. L. Ivanov, , and A. C. Gossard. *Phys. Rev. Lett.*, **96**, 227402, 2006.

[32] E. Wertz, L. Ferrier, D. D. Solnyshkov, R. Johne, D. Sanvitto, A. Lematre, I. Sagnes, R. Grousson, A. V. Kavokin, P. Senellart, G. Malpuech, and J. Bloch. *Nat. Phys.*, **6**, 860, 2010.

[33] A. Amo, S. Pigeon, C. Adrados, R. Houdrè, E. Giacobino, C. Ciuti, and A. Bramati. *Phys. Rev. B*, **82**, 081301, 2010.

[34] A.L. Ivanov and P. B. Littlewood. *Phys. Rev. Lett.*, **87**, 13, 2001.

[35] M. M. de Lim, M. van der Poel Jr., P. V. Santos, and J. M. Hvam. *Phys. Rev. Lett.*, **97**, 045501, 2006.

[36] M. J. A. Schuetz, J. Knörzer, G. Giedke, L. M. K. Vandersypen, M. D. Lukin, and J. I. Cirac. *Phys. Rev. X*, **7**, 041019, 2017.

[37] M Lindberg and R Binder. *J. Phys.: Condens. Matter*, **15**, 1119, 2003.

[38] R Binder and M Lindberg. *J. Phys.: Condens. Matter*, **18**, 729, 2006.

[39] M. Combescot, M. G. Moore, and C. Piermarocchi. *EPL*, **93**, 47012, 2011.

[40] Monique Combescot, Michael G. Moore, and Carlo Piermarocchi. *Phys. Rev. Lett.*, **106**, 206404, 2011.

[41] M. J. A. Schuetz, Michael G. Moore, and Carlo Piermarocchi. *Nat. Phys.*, **6**, 919, 2010.

[42] C. Gardiner and P. Zoller. Foundation of quantum optics. *Imperial College Press*, 2014.

[43] C. Gardiner and P. Zoller. *Imperial College Press*, 2015.

[44] H. Sahin, O. Leenaerts, S. K. Singh, and F. M. Peeters. *WIREs Comp. Mol. Sci.*, **5**, 255, 2015.

[45] H. Katow, J. Usukura, R. Akashi, K. Varga, and S. Tsuneyuki. *Phys. Rev. B*, **95**, 125205, 2017.

[46] N. Naka, K. Fukai, Y. Handa, and I. Akimoto. *Phys. Rev. B*, **88**, 035250, 2013.

[47] Y. Hazama and N. Naka. *Phys. Rev. B*, **90**, 045209, 2014.

[48] P. J. Dean, E. C. Lightowlers, and D. R. Wight. *Phys. Rev.*, **140**, 1A, 1965.

[49] J. Mitroy, S. Bubin, W. Horiuchi, Y. Suzuki, L. Adamowicz, W. Cencek, K. Szalewicz, J. Komasa, D. Blume, and K. Varga. *Rev. of Modern Phys.*, **85**, 693, 2013.

[50] Y. Suzuki, J. Usukura, and K. Varga. *J. Phys. B: At. Mol. Opt. Phys.*, **31**, 31, 1998.

[51] K. Varga and Y. Suzuki. *Phys. Rev. A*, **53**, 1907, 1995.

[52] K. Varga and Y. Suzuki. *Comp. Phys. Comm.*, **106**, 158, 1997.

[53] A. Schindlmayr. *Eur. J. Phys.*, **18**, 374, 1997.

[54] A. Jones, N. J. Ghimire H. Yu, S. Wu, G. Aivazian, J. S. Ross, B. Zhao, J. Yan, D. G. Mandrus, D. Xiao, W. Yao, and X. Xu. *Nat. Nanotech.*, **8**, 634, 2013.

[55] J. S. Ross, S. Wu, N. J. Ghimire H. Yu, A. M. Jones, G. Aivazian, J. Yan, D. G. Mandrus, D. Xiao, W. Yao, and X. Xu. *Nat. Comm.*, **4**, 1474, 2013.

[56] P. Hohenberg and W. Kohn. *Phys. Rev.*, **136**, 3B, 1964.

[57] W. Kohn and L. J. Sham. *Phys. Rev.*, **140**, 4A, 1965.

[58] P. Cudazzo, C. Attaccalite, I. V. Tokatly, and A. Rubio. *Phys. Rev. Lett.*, **104**, 226804, 2010.

[59] S. Lebègue, M. Klintenberg, O. Eriksson, and M. I. Katsnelson. *Phys. Rev. B*, **79**, 245117, 2009.

[60] F. Karlicky, R. Zboril, and M. Otyepka. *J. of Chem. Phys.*, **137**, 034709, 2012.

[61] O. Leenaerts, H. Peelaers, A. D. Hernandez-Nieves, B. Partoens, and F. M. Peeters. *Phys. Rev. B*, **82**, 195436, 2010.

[62] P. Cudazzo, L. Sponza, C. Giorgetti, L. Reining, F. Sottile, and M. Gatti. *Phys. Rev. Lett.*, **116**, 066803, 2016.

[63] Y. Cho and T. C. Berkelbach. *Phys. Rev. B*, **97**, 041409(R), 2018.